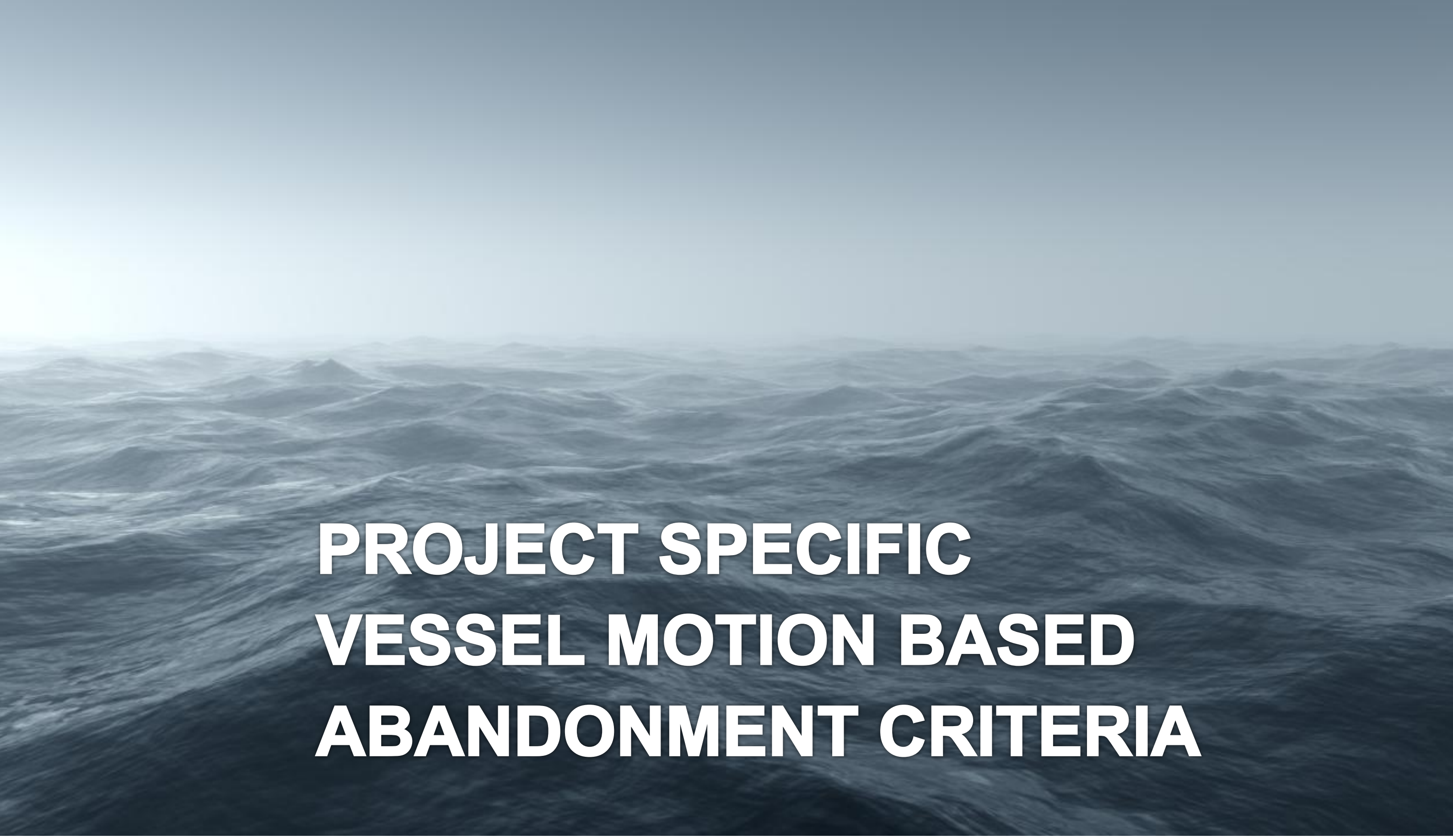

PROJECT SPECIFIC VESSEL MOTION BASED ABANDONMENT CRITERIA

Master of Science Thesis

J.F. Van Aubel

August 14th, 2015

For the degree of Master of Science in Offshore and Dredging Engineering
at Delft University of Technology

- confidential -

TU Delft Delft University of Technology

Allseas

Master of Science Thesis:

Project Specific Vessel Motion Based Abandonment Criteria

Author:

Jeroen F. Van Aubel

Thesis Committee:

Delft University of Technology	prof. dr. A.V. Metrikine (Chairman)
	dr. ir. K.N. van Dalen
	ir. Y. Qu
Allseas Engineering bv	ir. A.M. Geers
	ir. P. Demeersseman

ABSTRACT

When harsh weather conditions are expected during an offshore pipeline operation, the decision to start the abandonment procedure has to be taken based on pipeline integrity limits. The pipeline integrity which is analysed by a maximum design sea state does not correspond to the situation offshore, because sea states always occur in a different combination of parameters and therefore difficult to predict. Consequently abandonment decisions based on sea states to prevent the pipeline from buckling are difficult to take.

Presently the Allseas' pipelay vessels are running on-board software (SMD) what combines sea state predictions from multiple sources including metocean data, Wavex™ information and data from Motion Reference Units (MRU) which measure the actual vessel motions real-time. The SMD software can predict the significant wave height, zero crossing periods and approach directions. Furthermore the exact vessel motions can be predicted in the coming hours with fair accuracy which suggests an opportunity to develop vessel motion based abandonment criteria.

With the use of OrcaFlex by Orcina, pipeline installation is modelled for three case situations which differ in water depth and pipe properties. By performing time domain simulations using the Finite Element Method these cases are analysed to find the dominant vessel motions concerning pipeline integrity in a way such that some degrees of freedom can be discarded. Two different types of simulations are distinguished: The first type uses a large sum of short simulations with the model excited by theoretical predefined harmonic vessel motions. These simulations without wave effects are used to determine the direct relationship between vessel motions and pipeline integrity. The second method uses long time simulations with the model excited by stochastic design sea states. These simulations are used to determine which vessel motions and structural responses are expected. For both methods amplitude peaks of the time histories between the quantities are compared to develop and evaluate vessel motion based criteria for the different case situations.

For specific deep water operations where the pipeline is leaving the stinger almost vertically (departure angle of about 80°) and the tensioners are modelled on the brakes, the maximum bending moment which occurs in touchdown area is found to be well correlated with bottom tension and vertical velocity of the stinger tip. For deep water operations with an intermediate departure angle of about 45° and compensating tensioners, the maximum bending moment which occurs near the stinger tip is found to be correlated with the top tension and the vertical acceleration of the stinger tip, since the pipeline weight acts in the same direction.

For increasing amplitudes and frequencies of the vertical stinger tip motions the correlation with bending moment is affected due to geometric nonlinearities. For deep water operations this happens for unlikely excitations. However, in particular shallow water operations which result into small departure angles it is found that the natural frequencies which occur near the vessel motion peak frequencies result into large dynamic effects and increased geometric nonlinear behaviour. These geometric nonlinearities affect the correlation between stinger tip motions and the pipeline structural response in such way that the found vessel motion based criteria are not applicable.

Concluded is that for specific deep water projects with large departure angles, vessel motion based criteria based on vertical stinger tip motions show promising results. It is recommended to further study the applicability of the proposed vessel motion based criteria by analysing it with data generated by SMD during an actual pipelay operation.

ACKNOWLEDGMENT

This thesis is the final course of my Master of Science study in Offshore and Dredging Engineering at the Delft University of Technology. It has been performed in cooperation with the Pipeline Engineering department of Allseas Engineering bv in Delft. I would like to express my gratitude towards all the people that provided any kind of support during the full duration of this thesis.

At the Delft University of Technology, I would like to thank prof. dr. A.V. Metrikine for accepting me as one his graduation students and for lecturing the inspiring course "Structural Dynamics" which was in my opinion the most interesting course of the curriculum. Also I would like to thank ir. Y. Qu and dr. ir. K.N. van Dalen for their helpful support and participation in the graduation committee.

At Allseas Engineering, I would like to thank ir. P. Rijneveld for offering me the opportunity to graduate on this challenging assignment as well as giving me appreciated feedback during my thesis. Furthermore I want to express my gratitude to my daily supervisor ir. A.M. Geers for her enormous amount of support, guidance and constructive feedback during my graduation thesis. In particular the enthusiastic weekly meetings where very motivational. Then I would like to thank ir. P. Demeersseman for his perspicuous advice, feedback and his participation in the committee. Also I want to thank ir. A. Huisman for his welcome suggestion to start using OrcaFlex as well as giving me software support. Then I want to thank Orcina for providing me an educational license of OrcaFlex, ir. S de Groot for her support and participating in the meetings and M. van Veenendaal for his contribution in my MATLAB coding. Along with the persons earlier mentioned, I finally would like to thank ir. R. Vink and all the enthusiastic engineers of the department for their support and interest during my time at Allseas.

NOMENCLATURE

Abbreviations	Definition
A&R	Abandonment and Recovery
AP	After Perpendicular
API	Application Programming Interface
BC	Base Case
COG	Centre of Gravity
DOF	Degree Of Freedom
FBE	Fusion Bond Epoxy
FDM	Finite Difference Method
FEM	Finite Element Method
FEA	Finite Element Analysis
FD	Frequency Domain
FDFD	Finite Difference Frequency Domain
JONSWAP	Joint North Sea Wave Observation Project
LOP	Lift-Off Point
MRU	Motion Reference Unit
PE	Poly Ethylene
PM	Pierson-Moskovitz
R&D	Research & Development
RAO	Response Amplitude Operator
SB	Sagbend
SMD	Ship Motion Decision
ST	Stinger Tip
STA	Stinger Tip Area
TD	Time Domain
TDA	Touchdown Area
TDP	Touchdown Point
tnb	Local tangent, normal, binormal coordinate system
VIV	Vortex Induced Vibrations
XYZ	Global Cartesian coordinate system
xyz	Local Cartesian coordinate system

Latin symbols	Definition	Unit
$\mathbf{A}$	Added mass matrix	
A	Cross-sectional area	[m^2]
A_s	Cross-sectional steel area	[m^2]
$\boldsymbol{a}$	Connectivity matrix	
$\mathrm{a}(t)$	Local pipeline acceleration	[m/s^2]
$\mathbf{B}$	Complex load matrix	
$\mathbf{b}$	Complex response vector	
$\mathbf{C}$	Damping matrix	
C, c	Damping coefficient	[kg/s]
C_a	Added mass coefficient	[-]
C_D	Drag coefficient	[-]
D	Directional distribution	[-]
D_o	Outer steel diameter	[m]
E	Young's modulus	[N/m^2]
$\mathbf{F}$	Load matrix	
F	Force	[N]
f	Force per unit length	[N/m]
g	Gravitational acceleration	[m/s^2]
$\mathrm{H_S}$	Significant wave height	[m]
$H(\omega)$	Transfer function / RAO	[m/m]/[deg/m]
h	Water depth	[m]
I	Second moment of inertia	[m^4]
j	Integer / element no.	[-]
$\mathrm{K_C}$	Keulegan–Carpenter number	[-]
$\mathbf{K}$	**S**tiffness matrix	
$\boldsymbol{k}$	Element geometric stiffness matrix	
L	Length	[m]

Latin symbols	Definition	Unit
l	Beam element length	[m]
$\mathbf{M}$	Mass matrix	
M	Mass coefficient	[kg]
M	Moment	[Nm]
m	mass	[kg]
m_j	j^{th} spectral moment	[m^2/s^j]
N	No of elements	[-]
n	Integer	[-]
p	Pressure	[N/m^2]
Re	Reynolds number	[-]
R_1, R_2	Ramberg & Osgood parameters	[-]
$\mathrm{r}(t)$	Local pipeline displacement	[m]
$\mathrm{S}(\omega)$	One-dimensional variance density spectrum	[m^2s/rad]
$\mathrm{S}(\omega, \vartheta)$	Two-dimensional variance density spectrum	[m^2s/rad]
S	Shear force	[N]
s	Natural coordinate	[m]
$\mathbf{T}$	Transfer matrix	
T	Period	[s]
$\mathrm{T_Z}$	Zero crossing period	[s]
T	Effective tension	[N]
T_{tw}	True wall tension	[N]
t	Time	[s]
t_w	Wall thickness	[m]
$\mathbf{u}$	Nodal displacement vector	[m]
$\mathrm{v}(t)$	Local pipeline velocity	[m/s]
w	Unit weight	[N/m]
w_s	Submerged unit weight	[N/m]
$\mathrm{x}(t)$	Stinger tip displacement in global X direction	[m]
$\mathrm{x^{COG}}(t)$	Surge motion	[m]
$\mathrm{y}(t)$	Stinger tip displacement in global Y direction	[m]
$\mathrm{y^{COG}}(t)$	Sway motion	[m]
$\mathrm{z}(t)$	Stinger tip displacement in global Z direction	[m]
$\mathrm{z^{COG}}(t)$	Heave motion	[m]

Greek & other symbols	Definition	Unit
α	Phase	[rad] / [deg]
Γ	Gamma function	[-]
Δ	Difference operator	[-]
ε	Strain	[-]
ε_b	Bending strain	[-]
ε_t	Tensile strain	[-]
$\zeta(t)$	Surface elevation	[m]
$\theta(t)$	Pitch	[deg]
ϑ	Direction of incoming waves relative to the vessel	[deg]
κ	Curvature	[m^{-1}]
μ	Dynamic viscosity	[kg m^{-1} s^{-1}]
v	Flow velocity	[m/s]
$\xi(t)$	Arbitrary harmonic vessel motion	[m] / [deg]
ρ	Density of seawater	[kg/m^3]
ρ_s	Density of steel	[kg/m^3]
σ	Stress	[N/m^2]
δ	Deflection	[m]
$\varphi(t)$	Roll	[deg]
$\psi(t)$	Yaw	[deg]
ω	Frequency	[rad/s]
$(\dot{\ })$	Partial derivative with respect to time	[s^{-1}]
$(')$	Partial derivative with respect to the natural coordinate	[m^{-1}]
∇	Volume displacement	[m^3]

Subscripts (unless stated otherwise)	Definition
$()_{\mathrm{a}}$	Amplitude
$()_{\mathrm{b}}$	Local binormal direction
$()_{b}$	Buoyancy
$()_{c}$	Vector sum of bending
$()_{\mathrm{s}}$	Significant amplitude
$()_{I}$	Inertial
$()_{D}$	Drag
$()_{\mathrm{dyn}}$	Dynamic
$()_{d}$	Dry
$()_{E}$	Elastic
$()_{\mathrm{eq}}$	(Linear) equivalent
$()_{e}$	External
$()_{G}$	Geometric
$()_{g}$	Gravity
$()_{h}$	Hoop
$()_{i}$	Internal
$()_{j}$	Integer
$()_{k}$	Integer
$()_{\mathrm{n}}$	Local normal direction
$()_{n}$	Natural
$()_{p}$	Peak
$()_{roller}$	Roller boxes
$()_{\mathrm{sta}}$	Static
$()_{\mathrm{sim}}$	Simulation
$()_{\mathrm{span}}$	Unsupported span
$()_{seabed}$	Seabed
$()_{\mathrm{t}}$	Local tangential direction
$()_{\mathrm{vm}}$	Equivalent von Mises
$()_{ve}$	Lay vessel
$()_{\mathrm{X}}$	Global X direction
$()_{\mathrm{x}}$	Local x direction
$()_{\mathrm{Y}}$	Global Y direction
$()_{\mathrm{y}}$	Local y direction
$()_{y}$	Yield
$()_{\mathrm{Z}}$	Global Z direction
$()_{\mathrm{z}}$	Local z direction

CONTENTS

1.0	**INTRODUCTION**	**1**
1.1	Allseas Group S.A.	1
1.2	Pipeline installation using the S-lay method	1
2.0	**SCOPE OF WORK**	**2**
2.1	Problem background	2
2.2	Thesis Goal	3
2.3	Thesis Approach	3
2.4	Thesis Outline	4
2.5	Coordinate systems	4
2.5.1	Local coordinate system for the vessel	4
2.5.2	Local coordinate systems for the pipeline	5
2.5.3	Global coordinate system	5
3.0	**MECHANICS DURING OFFSHORE PIPELAY**	**6**
3.1	Vessel motions	6
3.1.1	Sea states	6
3.1.2	Linear theory	8
3.2	Pipeline loads during installation	9
3.2.1	Submerged weight	9
3.2.2	Hydrodynamic loads	9
3.2.3	Supports	11
3.2.4	Seabed loads	11
3.2.5	Tension	12
3.2.6	Internal loads	12
3.3	Pipeline integrity	14
3.3.1	Bending moment	14
3.3.2	Equivalent strain	15
3.4	Modelling dynamic effective tension	16
3.5	Numerical analysis	17
3.5.1	Beam elements	17
3.5.2	Static Analysis	19
3.5.3	Dynamic equilibrium	19
3.5.4	Linear dynamic analysis	19
3.5.5	Nonlinear dynamic analysis	21
3.5.6	Modal analysis	22
3.6	Chapter conclusion	22
4.0	**EXPERIMENTAL MODEL SETUP**	**23**
4.1	General model setup properties	23
4.2	Base cases	24
4.3	Modal analysis of the base cases	27
4.4	Chapter Conclusion	29
5.0	**DOMINANT VESSEL MOTIONS REGARDING PIPELINE INTEGRITY**	**30**
5.1	Vessel motions at COG	30
5.1.1	Vessel motions at COG using predefined harmonic motions	30
5.1.2	Vessel motions at COG using displacement RAOs	34
5.2	Superposed vessel motions	36
5.2.1	Superposition of vessel motions	36
5.2.2	Superposed vessel motions using displacement RAOs	38
5.3	Chapter conclusion	39
6.0	**VESSEL MOTION BASED CRITERIA**	**40**
6.1	Relation between vertical stinger tip motions and effective tension	40
6.1.1	Relation between vertical stinger tip motions and effective bottom tension without probability	40
6.1.2	Relation between vertical stinger tip motions and effective bottom tension with probability	42
6.1.3	Relation between vertical stinger tip motions and effective top tension	45
6.2	Relation between effective tension and bending moment	46
6.2.1	Constant effective tension in TDA	46

6.2.2 Time history comparison 47
6.2.3 Correlation between effective tension and bending moment in TDA 47
6.2.4 Geometric nonlinear behaviour 49
6.2.5 Influence of water depth on nonlinear behaviour 52
6.3 Relation between vertical stinger tip motions and extreme bending moments 56
6.3.1 Correlation between vertical stinger tip velocity and bending moment in the TDA 56
6.3.2 Correlation between vertical stinger tip acceleration and bending moment in the STA 58
6.3.3 Correlation between vertical stinger tip motions and bending moment in shallow water depths 58
6.4 Chapter conclusion 59

7.0 CONCLUSION 61
7.1 Vessel motion based criteria 61
7.2 Application for Allseas Engineering 61

8.0 RECOMMENDATIONS 62
8.1 Recommendations for adding vessel motion based criteria in SMD 62
8.2 Recommendations for future research 62

LIST OF FIGURES 63

LIST OF TABLES 66

REFERENCES 67

APPENDIX A: FREE VIBRATIONS FOR THE BENDING OF A SIMPLY SUPPORTED BEAM 69

APPENDIX B: HYDRODYNAMIC FLUID FLOW REGIMES 71

APPENDIX C: INFLUENCE OF DIRECTIONAL WAVE SPREADING 72

1.0 INTRODUCTION

1.1 Allseas Group S.A.

The Swiss-based Allseas Group S.A was founded in 1985 by Edward Heerema. It is one of the major offshore pipelay installation and subsea construction companies in the world. The Allseas Group S.A. counts over 2500 employees operating worldwide with offices in the Netherlands, USA, Australia, India, Portugal, Belgium and Switzerland. The company operates a fleet of six vessels for pipelay installation, pipelay support, trenching, subsea installation and heavy lifting purposes. All their vessels are designed and developed by the company itself. Their approach is to support their clients who already are in the conceptual design stage with services like project management, engineering, procurement, installation and decommissioning. The five specialised pipelay vessels of Allseas are: Lorelay, Solitaire, Audacia, Tog Mor and the new Pioneering Spirit. Each vessel is suited for a specific area in offshore pipeline installation.

Allseas Engineering bv is part of the Allseas Group S.A. and based in Delft. At Allseas Engineering most of the office work is completed. The department of Pipeline Engineering is responsible for the design, analysis and support for the installation of pipelines and inline structures. Naval Engineering (subdivision of the R&D department) is responsible for the design, analysis and support of the vessels. For specific projects, both teams are responsible for the interaction between vessel motions and pipeline response during offshore pipeline installation.

1.2 Pipeline installation using the S-lay method

At Allseas the installation of pipelines is performed using the S-lay method. The vessel pays out pipeline over the firing line from beadstall (first welding station) to touchdown point (TDP). The pipeline section which is bended by the stinger is called the overbend. The section which is bent by the seabed is called the sagbend. Therefore the catenary curve looks like the shape of an S. The point between the overbend and sagbend where the pipeline is straight (zero bending moment) is called the inflection point.

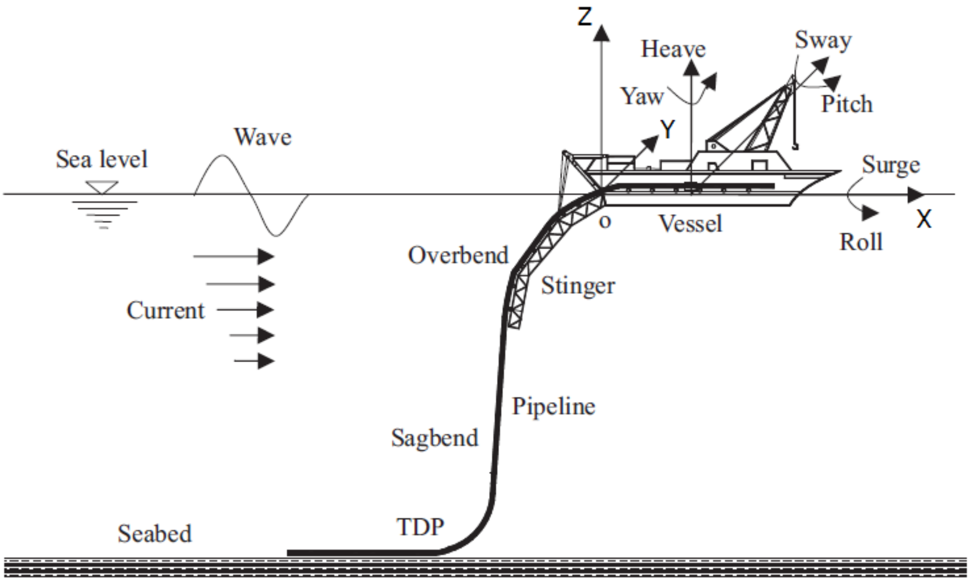

Figure 1-1 Offshore pipeline installation using the S-lay method. Adapted from (Gong, et al., 2014)

By keeping the pipeline under tension by the tensioners, the pipeline is laid on the seabed by moving the vessel or by braking the tensioners between paying out pipeline. Vessel motions cause dynamic tension fluctuations in the pipeline. Tensioners can compensate a large part of the dynamic tension fluctuations by compensating paying out and pulling in pipeline. If the dynamic tension exceeds a limit which cannot be compensated by the tensioners, the pipeline integrity will be affected and the pipeline could buckle. Therefore an optimal lay tension is an important parameter when laying pipeline.

2.0 SCOPE OF WORK

2.1 Problem background

When harsh weather conditions are expected during a pipeline operation, the decision to start the abandonment procedure has to be taken. The pipeline integrity is limited by an operational limit. This operational limit is currently defined by a design sea state (Figure 2-1). Such statistical sea state is characterised by a significant wave height (H_S), a zero crossing wave period (T_Z) and the conservative worst case direction of incoming waves relative to the vessel (ϑ). With this design sea state it is never possible to get the same limiting sea state offshore, because the sea state criteria always occur in a different combination of the characteristic parameters. Besides it is at the moment impossible to determine the exact actual H_S, T_Z and ϑ. Both facts result into a difficult interpretive and conservative operational limit.

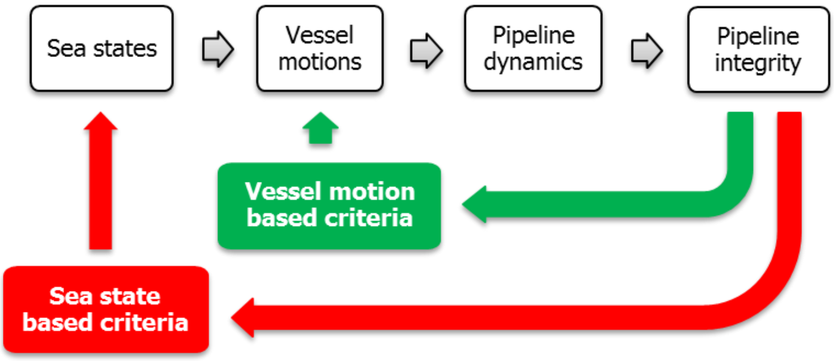

Figure 2-1 Vessel motion based criteria vs Sea state based criteria

At Allseas Engineering, the innovation department developed on-board software what combines sea state predictions from multiple sources such as metocean forecasts, Wavex™ (radar) information and data from Motion Reference Units (MRU). This Ship Motion Decision software (SMD) can predict in addition to the sea state, the vessel motions in upcoming hours based on spectral weather forecasts (Figure 2-2). This so-called (vessel) response forecasting could support the decision making for A&R procedures. Despite response forecasting is relatively new in the offshore pipelay industry; it has been used quite effectively in the offshore drilling industry since the 1980s. It helps the decision making during deep water drilling and crane vessel operations exposed to large sea states. (Standing, 2005).

If vessel motion based criteria (Figure 2-1) is evaluated against predicted vessel motions, SMD could be developed further with improved operational limit criteria. This will cause SMD to be more reliable in creating a better overview for taking A&R operational decisions.

Figure 2-2 Graphical user interface of the SMD application

2.2 Thesis Goal

The previous section leads to the following goal:

"Develop project specific vessel motion based abandonment criteria"

The associated main research question is:

"What vessel motion limits pipeline integrity?"

To find an answer for above question, the following sub-questions help to reach the goal:

- What loads influence the pipeline integrity?

- How do vessel motions affect the pipeline integrity during S-Lay operations?
  - What vessel motions are dominant regarding pipeline integrity?

- How can pipeline integrity be predicted by measuring vessel motions?
  - To what extent the relationship between vessel motions and pipeline integrity is linear?

2.3 Thesis Approach

First the mechanics during pipeline installation are investigated. Vessel motions for a set of design spectra are derived using linear theory. Also the external and internal loads of the pipeline catenary and their impact on the pipeline integrity will be analysed. In order to find static and dynamic approximations of the loads, different solution methods are described. Because of the nonlinear nature of some mechanics, the focus is on numerical approximation methods.

With the use of the numerical analysis software OrcaFlex (v9.8c) by Orcina, pipeline installation is modelled and analysed for three different situations. Using finite element simulations, successively static analyses and modal analyses are investigated to find the expected behaviour of the base cases with regards to the pipeline integrity.

Multiple dynamic analyses will be studied to find a dominant vessel motion with regards to the pipeline integrity. Two different excitation methods will be treated. The first method uses many short simulations with excitation by theoretical predefined harmonic vessel motions without waves. The second method uses long stochastic simulations with excitation by sea states. By using contour plots and polar plots the results are presented and analysed for all three base cases.

With the use of the dominant vessel motions and dominant loads on the pipeline, the relationship between pipeline integrity and the dominant vessel motion is analysed and there limitations are discussed for the different base cases and different type of excitations. Both excitation methods are used. In the stochastic method, the peaks of the time histories are compared to find relations. This way project specific vessel motion based abandonment criteria is indicated. Also the linear / nonlinear behaviour is investigated.

2.4 Thesis Outline

This thesis is build up in four parts before describing conclusions and recommendations. Each part (single chapter) will end with a conclusion before starting the next. In this section each chapter will be treated.

Chapter 3: Mechanics during offshore pipelay
The goal of this chapter is to give an overview of mechanics and modelling of offshore pipelay operations. The theory behind the mechanics and most important loads during offshore pipeline installation are derived and analysed regarding pipeline integrity. Simplifications for pipeline integrity and dynamic tension are introduced. Also different methods for setting up a more complete model are explained including their advantages and disadvantages. The mechanics described in this chapter are modelled in the next chapter.

Chapter 4: Experimental model setup
In this chapter the three models (base cases) which are set up in OrcaFlex are described. Also the static and mode shapes are analysed.

Chapter 5: Dominant vessel motions regarding pipeline integrity
The impact of the different vessel motions on the three base cases are determined and analysed. In this chapter the dominant vessel motion with the most impact on the pipeline integrity is derived and analysed.

Chapter 6: Vessel motion based laying criteria
Using the findings of the previous three chapters, vessel motion based criteria is derived using the comparison procedure. Also the limitations of the criteria are treated.

2.5 Coordinate systems

In this thesis three coordinate systems are used in order to describe the kinematics and dynamics appropriately. To distinguish all three of them, they are described separately in this section.

2.5.1 Local coordinate system for the vessel

The origin in the local Cartesian coordinate system (xyz) of the vessel is at its After Perpendicular (AP).
AP is defined as the intersection between the water line with the after-side from the straight portion of the vessel's rudder post (McGraw-Hill, 2002). The vessel motions are parallel to the axis of the coordinate system. The forward motion of the vessel (surge) is parallel to the x-axis. The motion directed to starboard (sway) is parallel to the y-axis and the motion lifting the vessel upwards (heave) is parallel to the z-axis. Besides the three translational degrees of freedom (DOF) also three rotational vessel motions occur. Roll rotates about the x-axis, pitch rotates about y-axis and yaw rotates about the z-axis. In Figure 2-3 the vessel motions at the centre of gravity (COG) of the vessel are presented.

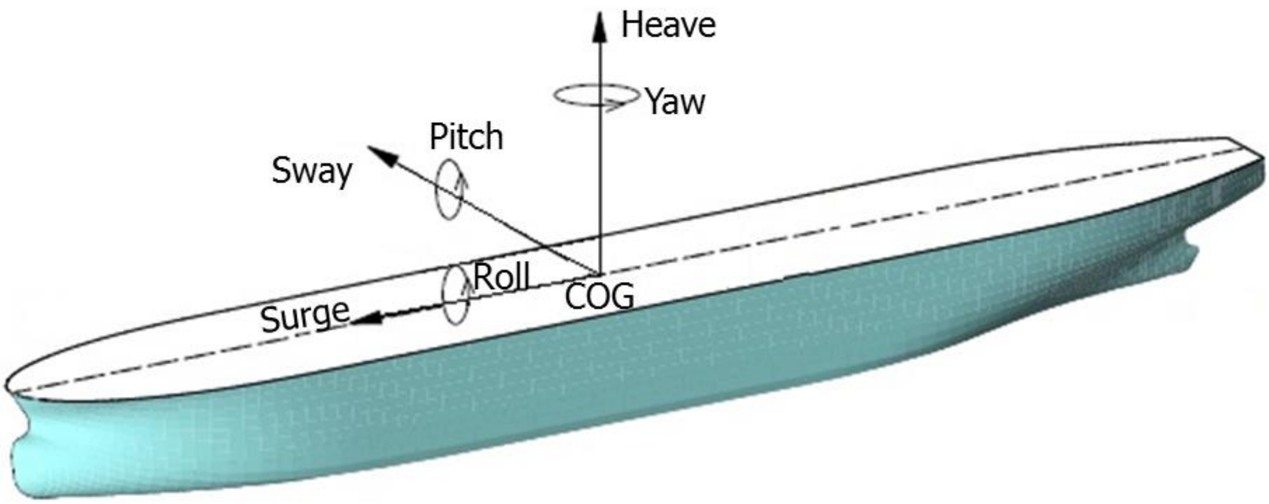

Figure 2-3 Vessel motions in six degrees of freedom at the centre of gravity of the vessel

2.5.2 Local coordinate systems for the pipeline

Because the pipeline is curved, the coordinate system of the pipeline is described in a local tangent, normal, binormal coordinate system (tnb) in addition to the global coordinate system. As presented in Figure 2-4. The axial motion of a point of the pipeline is directed in the local tangential direction (t-direction). Positive axial motions are directed to the beadstall and negative to touchdown point (TDP). Perpendicular to the tangential direction and in the dominant plane of bending, the normal (n-direction) is directed. The binormal direction is directed perpendicular to both the tangential and normal direction.

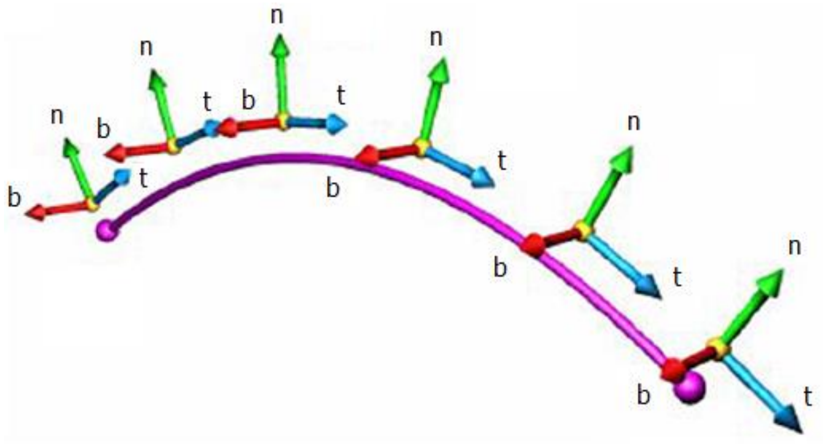

Figure 2-4 local tnb-coordinate system for the pipeline

For a single beam element representing a small section of pipeline a local Cartesian coordinate system (xyz) is used. Here is x in tangential direction, z in normal direction and y in binormal direction of the beam section.

2.5.3 Global coordinate system

All local coordinate systems are implemented in one global earthbound coordinate system (XYZ). The local coordinate system of the vessel is placed in XYZ in a way that the origin of xyz and XYZ are the same. Note in Figure 2-5 that gravity is directed in negative Z-direction and the waterline is parallel to the X-direction and Y-direction. The global Z-coordinate of TDP is the water depth minus the mean draught of the vessel.

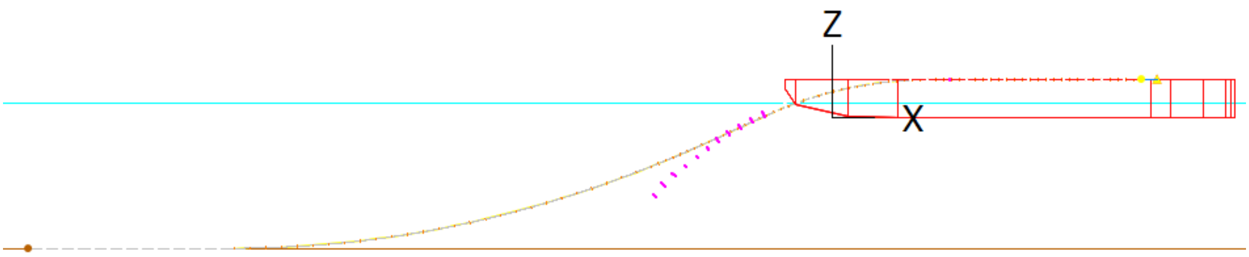

Figure 2-5 2D representation (ZX-plane) of the pipeline catenary in the global XYZ-coordinate system

3.0 MECHANICS DURING OFFSHORE PIPELAY

The goal of this chapter is to give an overview of the mechanics and modelling of offshore pipelay operations. The mechanics and most important loads during offshore pipeline installation are derived and analysed with regards to the pipeline integrity. Simplifications for pipeline integrity and dynamic tension are introduced. Also different methods for setting up a more complete model are explained including their advantages and disadvantages. These simplifications and the numerical method described in this chapter are used in the next chapters.

3.1 Vessel motions

Vessel motions measured by MRUs during offshore operations are different than the modelled vessel motions in the engineering phase. This is mainly due to the uncertainty of the sea state which is introduced in the problem background (section 2.1). During the design phase of a pipeline operation, vessel motions are derived from stochastic sea states by means of linear theory. This section will describes the modelling of sea states, RAOs and vessel motions while using linear theory.

3.1.1 Sea states

The weather conditions offshore are described using sea states. Sea states are also used as design input for the dynamic analysis of pipelines during installation. A sea state describes the sea surface as a stochastic stationary Gaussian distributed process of all possible time records that can be made under conditions of the actual observation. The wave field of a sea state can be described with the random-phase/amplitude model. Its foundation is that all waves are statistically independent and generated by local winds (Holthuijsen, 2007). Also the nonlinear interaction between the wave components is discarded. Using the random-phase/amplitude model the sea surface can be represented as the sum of a large number of independent wave components. Each wave component has a constant amplitude which is Rayleigh distributed and a random phase which is uniform distributed. The variance of the expected amplitude of each wave component is distributed over an infinitely small frequency interval to obtain a continuous variance density spectrum. It gives a complete statistical description of the stationary Gaussian surface elevation of ocean waves. A narrow variance density spectrum contains more regular waves than a wide banded spectrum which results in more variation of wave frequencies.

To characterize the variance density spectrum, the significant wave height and zero crossing period are determined. Both can be determined by the spectral moments of the variance density spectrum which are calculated with equation (3.1).

$$m_j = \int_{-\infty}^{\infty} \omega^j \left|S_\zeta(\omega)\right|^2 d\omega \tag{3.1}$$

Where m_j is the j^{th} spectral moment, $S_\zeta(\omega)$ the variance density spectrum and ω the frequency.
The estimated significant wave height H_S and zero crossing period T_Z can then be determined with (3.2).

$$\begin{gathered} H_S \approx 4\sqrt{m_0} \\ T_Z = \sqrt{\frac{m_0}{m_2}} \end{gathered} \tag{3.2}$$

For different types of ocean waves a couple of frequently used variance density spectra are used. For a long crested sea-surface often a Pierson-Moskovitz (PM) spectrum is used and for a short crested sea-surface the JONSWAP spectrum is used which is based on the PM spectrum (Holthuijsen, 2007), but with a larger peak and a smaller tail. In Figure 3-1 a one dimensional JONSWAP spectrum is presented with parameters which are used in a limiting sea state.

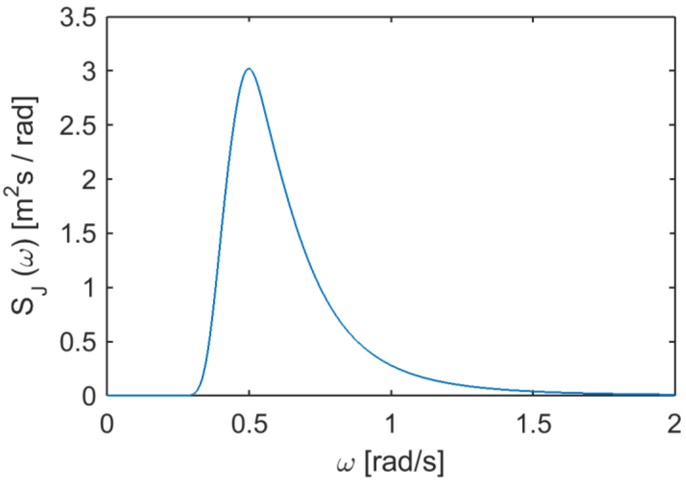

Figure 3-1 1D variance density spectrum of a limiting sea state, JONSWAP, $\mathrm{H_S} = 4.0m$, $\mathrm{T_Z} = 9.0s$

A sea state is besides wave height and wave frequency also dependent on the vessel approach direction ϑ. Therefore the variance density spectrum presented in Figure 3-1 should also contain directional dependency. Generally the two-dimensional (directional) wave spectrum $\mathrm{S}(\omega, \vartheta)$ is considered as the product of a one-dimensional wave spectrum and a directional distribution $\mathrm{D}(\vartheta)$ like in equation (3.3) (Holthuijsen, 2007).

$$\mathrm{S}(\omega, \vartheta) = \mathrm{S}(\omega)\mathrm{D}(\vartheta) \tag{3.3}$$

There are different methods for the directional distribution. The most used and recommended is the cosine-n method (DNV-RP-C205, 2010) which gives equation (3.4).

$$\mathrm{D}(\vartheta) = \frac{\Gamma(1 + n/2)}{\sqrt{\pi}\Gamma(1/2 + n/2)} \cos^n(\vartheta - \vartheta_P) \tag{3.4}$$

ϑ_P denotes the peak direction, Γ the gamma function and the power n controls the width of the distribution due to dependency of the wind and frequency. A power of $n = 2$ gives a large amount spreading and may underestimate the waves in the peak direction. Therefore when wave directional spreading is included in simulations a more conservative power like $n = 8$ is used (Figure 3-2) which result in moderate wave directional spreading.

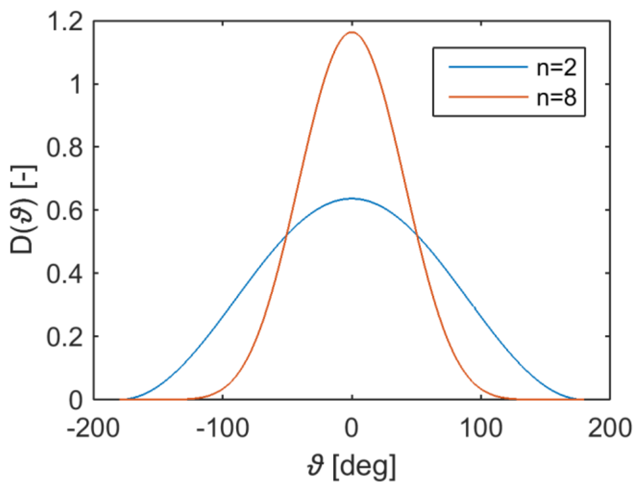

Figure 3-2 Directional distribution using the cosine-n method

3.1.2 Linear theory

In this thesis linear theory is used to transfer waves into vessel motions. This means that the relationship between incident regular waves and the vessel response on those waves is linear. Loads by wind and current have are out of the scope and are neglected in this thesis. Assumed is that the second order mean drift force is compensated by the dynamic positioning system of the vessel and low frequency secondary wave forces do not significantly influence the vessel motions in deep water.

The dynamic behaviour of the vessel can be described using the linearized hydrodynamic loads. These are dynamic forces and moments caused by the fluid on the oscillating vessel in still water. Waves are radiated from the vessel. The hydrodynamic loads on the vessel can be split in two parts (Journée & Massie, 2000):

- The incident (also known as Froude-Krylov) force. This is the pressure of the undisturbed waves integrated over the wetted surface of the vessel
- Diffraction forces and moments. These are pressures that occur due to the wave disturbances caused by the vessel.

Using the static equilibrium of forces and moments, these forces can be rewritten in an equation of motion for the vessel. For the pipelay vessel this is:

$$(\mathbf{M}_{ve} + \mathbf{A}_{ve})\ddot{\mathbf{u}}(t) + \mathbf{C}_{ve}\dot{\mathbf{u}}(t) + \mathbf{K}_{ve}\mathbf{u}(t) = \mathbf{F}_{ve}(t) \tag{3.5}$$

$\mathbf{M}_{ve}$ = mass matrix
$\mathbf{A}_{ve}$ = added mass matrix
$\mathbf{C}_{ve}$ = damping matrix
$\mathbf{K}_{ve}$ = stiffness matrix
$\mathbf{u}(t)$ = displacement vector
$\mathbf{F}_{ve}(t)$ = hydrodynamic load vector

The hydrostatic forces can be rearranged in the stiffness matrix $\mathbf{K}_{ve}$. The diffraction forces and moments can be written into added mass and damping matrices using 3D potential theory (Journée & Massie, 2000). To obtain the equation of motion for a complex hull, Allseas uses 3D diffraction software (e.g. AQWA). This software calculates the forces and moments of the vessel using 3D potential theory and by dividing the vessel's hull into surface panels.

Within linear theory the transfer functions which relate waves into vessel responses are known as RAOs (Response Amplitude Operators). For all six DOFs of the vessel, specific RAOs are determined. Both amplitude and phase characteristics of the RAO are dependent on the frequency and direction of the incident waves (Journée & Massie, 2000).

$$H(\omega,\vartheta) = |H(\omega,\vartheta)|e^{i\angle H(\omega,\vartheta)} \tag{3.6}$$

$H(\omega,\vartheta)$ = RAO depending on frequency and direction
$|H(\omega,\vartheta)|$ = modulus (magnitude) of the RAO
$\angle H(\omega,\vartheta)$ = argument (angle) of the RAO

Suppose an incident harmonic surface elevation $\zeta(t)$ with a random amplitude ζ_a and frequency ω will excite the vessel from a certain direction ϑ in its COG:

$$\zeta(t) = \zeta_a e^{-i\omega t} \tag{3.7}$$

Depending on the wave characteristics, an arbitrary vessel motion $\xi(t)$ will respond to the wave motion by (with phase $\alpha_{\xi\zeta}$ relative to the incoming wave):

$$\xi(t) = \xi_a e^{-i(\omega t - \alpha_{\xi\zeta})} \tag{3.8}$$

The ratio of the complex amplitudes of the output signal to the input signal is the RAO and equal to:

$$H_{\xi\zeta}(\omega,\vartheta) = \frac{\xi(\omega,\vartheta)}{\zeta(\omega,\vartheta)} = \frac{\xi_a}{\zeta_a}e^{i\alpha_{\xi\zeta}} \tag{3.9}$$

The modulus of the RAO is the ratio of the output and input amplitudes:

$$\left|H_{\xi\zeta}(\omega,\vartheta)\right| = \frac{\xi_a}{\zeta_a} \tag{3.10}$$

The argument of the RAO is the phase shift.

$$\angle H_{\xi\zeta}(\omega,\vartheta) = \angle\xi(\omega,\vartheta) - \angle\zeta(\omega,\vartheta) = \alpha_{\xi\zeta} \tag{3.11}$$

To determine the RAOs for the pipelay vessel, the matrices in the equation of motion (3.5) must be known. For a simplified vessel (e.g. homogeneous barge) this can be done analytically, but for a complex hull (an Allseas vessel) the RAOs are approximated using 3D diffraction software. The RAOs are only of interest for a range of frequencies where waves excite the vessel. This frequency range is typically between 0.30 rad/s and 1.25 rad/s. Assumed is the vessel is symmetric on its longitudinal x-axis (dashed line in Figure 2-3). For that reason only half of the approach directions relative to the vessel are required to obtain RAOs for all directions.

Using the RAOs, a specific response spectrum of any variance density spectrum can be derived with equation (3.12)

$$S_{\xi\zeta}(\omega,\vartheta) = \left|H_{\xi\zeta}(\omega,\vartheta)\right|^2 \cdot S_\zeta(\omega,\vartheta) \tag{3.12}$$

With the response spectra for each vessel motion in a certain direction, vessel motions can be simulated.

3.2 Pipeline loads during installation

The loads of a pipeline during installation can be divided in environmental and structural loads. The environmental loads originate from the fluid, seabed, waves, wind and due to vessel motions which act on the pipeline through the supports of the vessel. The structural loads come from the pipeline, weight of the pipeline, tensioners and the supports of the vessel itself. The loads derived and discussed in this section are important for the distinct shape of the catenary and the pipeline integrity.

3.2.1 Submerged weight

The unit gravity, f_g is equal to the unit dry weight of the homogeneous pipeline w_d and can be determined using the following equation.

$$f_g = w_d = \tfrac{\pi}{4}\left({D_e}^2 - {D_i}^2\right)\rho_s g \tag{3.13}$$

With D_e,D_i respectively the external and internal diameter of the pipeline. ρ_s is the density of the pipeline's material (steel) and g the gravitational acceleration. If the pipeline has corrosion coatings or concrete coatings, these thicknesses and densities should be included in equation (3.13) (Sparks, 2007).
According to Archimedes' law a submerged body in a fluid experiences an upwards force equal to the weight of the displaced fluid. This static load f_b (known as buoyancy) acting on a submerged body yields:

$$f_b = \rho\nabla g \tag{3.14}$$

With ∇ the volume displacement and ρ the density of the fluid (seawater $\rho = 1025$ [kg/m^3]). The unit submerged weight w_s is the nett sum of the unit inertia load and the unit hydrostatic load:

$$w_s = f_g - f_b = \tfrac{\pi}{4}\left({D_e}^2(\rho_s - \rho) - {D_i}^2\rho_s\right)g \tag{3.15}$$

3.2.2 Hydrodynamic loads

If a slender uniform cylinder is placed vertically in a fluid with a certain flow, the flow will apply a pressure distribution around the cylinders wall circumference. The pressure distribution is dependent on the Reynolds number which can be defined as the ratio of inertia forces and viscous forces of the fluid:

$$\mathrm{Re} = \frac{\rho D_e \mathrm{v}}{\mu} \tag{3.16}$$

With v the flow velocity and μ the dynamic viscosity.

For different boundaries of Reynolds numbers one can divide different flow regimes of pressure distributions around the cylinders wall circumference. These are described in Appendix B.

During the installation of pipelines, the pressure in the wake (which is the region of disturbed fluid flow behind the cylinder) is lost due to flow induced disturbances. Therefore a pressure difference will rise between the front and wake of the pipeline which results into a force on the pipeline. This force has a drag and lift term which consists out of pressure and friction forces. The pressure forces are time dependent, because of periodic shedding (Journée & Massie, 2000). For the determination of the force due to pressure and friction, this time dependency is normally neglected and the mean force is taken equal to zero. The lift force could be important when vortex induced vibrations (VIV) have influence (Ogink, 2001).
VIV are vibrations due to alternate shedding of the vortices in the wake of the pipeline. In pipeline engineering, VIV have influence on free span pipelines at the seabed or for very long pipe spans in relation with the fatigue damage after installation. Because of relatively short installation periods during S-lay, VIV during pipeline installation are of minor importance and neglected during installation. Without VIV the mean load containing fluid pressure and friction effects is equal to the mean drag force (Ogink, 2001).

The unit hydrodynamic drag force $f_D(t)$ is typically expressed in terms of the stagnation pressure (static pressure at a stagnation point in a fluid flow) multiplied with the external diameter of the pipeline and a drag coefficient C_D:

$$f_D(t) = \tfrac{1}{2}\rho C_D D_e \mathrm{v}_r(t)|\mathrm{v}_r(t)| \tag{3.17}$$

With $\mathrm{v}_r(t)$ the relative velocity of fluid around the normal direction of the pipeline. Currents occur in the first hundreds meters below sea surface level. Pipelines installed with the S-lay method currents are not sensitive to currents, because of the stinger which supports the pipeline (Gong, et al., 2014) (note also Figure 1-1). Therefore the relative velocity of the fluid $\mathrm{v}_r(t)$ is assumed equal to the velocity of pipeline itself. Further investigation to current is out of the scope in this thesis. Fluid drag mainly acts in lateral direction of the pipeline (Journée & Massie, 2000), thus the C_D in normal and binormal direction is much larger than in axial direction.

The drag coefficient is depending on the Reynolds number, surface roughness of the pipeline and the frequency dependent Keulegan Carpenter number ($\mathrm{K_C}$):

$$\mathrm{K_C} = \frac{\mathrm{vT}}{D_e} \tag{3.18}$$

With v the velocity of the pipeline, T the oscillation period and D_e the external diameter of the pipeline.

Drag coefficients at sea are typically between 2.0 and 0.6. For offshore pipelines, the surface roughness is neglected and the drag coefficient C_D = 1.2. More accurate is to use a variable drag coefficient for more turbulent flow as the drag coefficient is very depending on the Reynolds number (Sumer & Fredsøe, 1997).

Besides the drag force, the hydrodynamic load also has an inertia term. The inertia part is caused by the additional mass of the fluid around the body which is accelerated due to the action of pressure. This added mass is for dependent of the fluid mass displacement by the pipeline. It is also dependent on the effects in the wake which are depending on Re and $\mathrm{K_C}$ and contribute to the added mass coefficient C_a. This non-dimensional coefficient C_a varies between 0 and 1. In this thesis an added mass coefficient of C_a = 1 is used. The hydrodynamic unit inertia force f_I yields (Sparks, 2007)

$$f_I = \rho A_e C_a \mathrm{a}_r \tag{3.19}$$

With A_e the external area of the cross-section and a_n the acceleration of the pipeline in normal direction.

If the pipeline is moving through flowing fluid an additional term from the Froude-Krylov force is to be included in the hydrodynamic load. This term is equal to the displaced fluid multiplied with the acceleration of the current flow. Since offshore pipeline installation is dominated by drag effects, the Froude-Krylov term is often neglected. In this thesis, the sea environment is modelled without current flow and thus is the term is automatically removed.

The total hydrodynamic unit load f_{dyn} is the sum of the drag and inertia term and yields (Sparks, 2007):

$$f_{\mathrm{dyn}} = -(f_D + f_I) = -\tfrac{1}{2}\rho C_D D_e \mathrm{v}_r(t)|\mathrm{v}_r(t)| - \rho A C_a \mathrm{a}_r \tag{3.20}$$

Note that the minus sign is present, because the force is in opposite direction of the pipeline movement. Equation (3.21) is known as the Morison equation (Journée & Massie, 2000). The equation was originally derived and used for hydrodynamic forces on straight piles. Fortunately, the equation also produces good results for pipelines as long the outer diameter is small in relation with the wavelength. However the flow on the pipeline is not perpendicular along the span length. Therefore the flow velocity is decomposed into components normal and transverse to the pipeline axes.

3.2.3 Supports

Because the pipeline is supported on the vessel this pipeline will get about the same excitation as the pipelay vessel. The pipeline on the firing line is supported on rollers which are located in so-called roller boxes on the vessel and stinger with certain spacing in between. Under ideal laying conditions, the pipeline is evenly distributed on the roller boxes with contact forces perpendicular to the pipelines axial axis. Each roller box can be accurately modelled as a set of springs with a fixed stiffness giving frictionless support (Verwoert, 2012). The first pair of springs normal to the pipe is to support the pipeline and loads. The second pair of springs is to restrain the lateral movement of the pipe. There can be assumed that the contact force increases linear with the deformation (Verwoert, 2012). The following equations arise

$$\begin{aligned} \mathrm{F}_{support} &= \mathrm{K}_{roller} \cdot \delta_{roller} && \text{for} \quad \delta_{roller} > 0 \\ \mathrm{F}_{support} &= 0 && \text{for} \quad \delta_{roller} \leq 0 \end{aligned} \tag{3.21}$$

With $\mathrm{F}_{support}$ the contact load, K_{roller} the roller box stiffness and $\delta_{roller}$the deflection of the roller.

Figure 3-3 side view (left) and front view (right) of a modelled support with springs

3.2.4 Seabed loads

The loads of the seabed acting on the pipeline result from the bearing capacity which counteract the pipeline's weight and soil resistance which balances the horizontal equilibrium of forces. The interaction of the pipeline and the seabed can be modelled in various degrees of accuracy. (Schmidt, 1977) was the first who used a linear elastic foundation for the modelling of offshore pipelay. Much more advanced models exist which includes effects for various soils, empirical constants and stiffness' with nonlinear behaviour (Randolph & Quiggin, 2009). However these soil models are still unable to describe vertical pipe-seabed interaction using variable soil stiffness with pipeline penetration under cyclic motions (Gong, et al., 2014). Therefore nonlinear methods are not usable for a dynamic pipelay analysis and a linear elastic foundation will be modelled. Also for simplicity a flat seabed surface is assumed. Hence the equations for the seabed load are

$$\begin{aligned} F_{seabed} &= K_{seabed} \cdot \delta_{seabed} && \text{for} \quad \delta_{seabed} > 0 \\ F_{seabed} &= 0 && \text{for} \quad \delta_{seabed} \leq 0 \end{aligned} \tag{3.22}$$

With F_{seabed} the seabed load, K_{seabed} the soil stiffness of the seabed and $\delta_{seabed}$the seabed deflection.

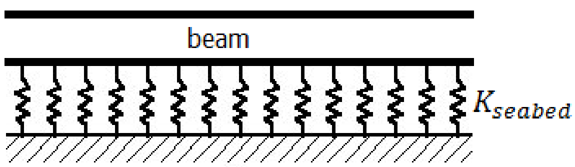

Figure 3-4 Linear elastic foundation

3.2.5 Tension

The required amount of tension is dependent on the engineering limits. If the applied tension decreases, the sagbend radius decreases and LOP moves further down on the stinger until it reaches the stinger tip. If that happens the pipeline causes loads on the stinger tip which is prohibited during laying, because it could lead to damaging and possible buckling of the pipeline. Therefore LOP and its departure angle is tension dependent. For submerged pipelines it is better to define the effective tension, because in addition to the resulting true wall force from axial stresses in the pipeline's wall T_{tw}, the pressure difference between both sides of the wall also has influence on the axial force in the pipeline. (Sparks, 2007). This leads to equation (3.23).

$$T = T_{tw} + A_e p_e - A_i p_i \tag{3.23}$$

With
A_i, A_e the internal and external area of the of the pipeline's cross section.
p_i, p_e the internal and external pressure of the fluid (sea water).

The effective tension between LOP and TDP can be factorized into a horizontal component in global X-direction and a vertical component in Z-direction. The horizontal component of the effective tension of each point along the sagbend is always constant. The vertical component of the effective tension is weight dependent. The effective top tension is close to the effective tension at LOP (Gong, et al., 2014).

3.2.6 Internal loads

In the sagbend region the bending stiffness of the pipeline can be assumed to behave linear elastic (Jensen, 2010),(Orcina, 2014). Non-linear bending behaviour is primarily an issue for the overbend where the pipeline is plastically bent over the stinger. Because the deformations of the pipeline in the sagbend are considered to be linear elastic and without shear deformations, the sagbend catenary can be described as an Euler-Bernoulli beam using large deflection theory (Sparks, 2007). In the static equilibrium of the beam, the beam is deformed by bending, shearing and twisting forces. If the external loads are larger than the internal loads, the static equilibrium loses balance and local buckling may happen. On the other hand, if the external loads are vanished, the shape of the beam returns to its original shape. In Figure 3-5 a small two-dimensional in-plane (XZ) segment of the beam is shown (Jensen, 2010). In the two-dimensional situation of Figure 3-5 the tensioned pipeline is homogenous with uniform cross-sections and weight distribution along its length.

The equilibrium of forces in the global XZ plane yields (Jensen, 2010)

$$(T + dT)\cos(\theta + d\theta) - T\cos\theta + (S + dS)\sin(\theta + d\theta) - S\sin\theta = 0 \tag{3.24}$$

$$(T + dT)\sin(\theta + d\theta) - T\sin\theta + (S + dS)\cos(\theta + d\theta) - S\cos\theta - w_s ds = 0 \tag{3.25}$$

With θ the angle and S the shear force acting in normal direction of the pipeline. For small values of $d\theta$, the following approximations are valid:

$$\begin{aligned} \cos(\theta + d\theta) &\approx \cos\theta - d\theta\sin\theta \\ \sin(\theta + d\theta) &\approx \sin\theta + d\theta\cos\theta \end{aligned} \tag{3.26}$$

After substituting the approximations of (3.26) in (3.27) and (3.28) and multiplying (3.27) with $(-\sin\theta)$ and (3.28) with $(\cos\theta)$ the equations are simplified. By adding both equations and dividing by ds one equation results which determines equation (3.27) (Jensen, 2010):

$$T\kappa - S' - w_s\cos\theta = 0 \tag{3.27}$$

With κ the curvature of the pipeline which is the derivative of the angle ($\kappa = \theta'$). From Euler-Bernoulli beam theory, the following equations are given:

$$\begin{aligned} M &= EI\kappa = EI\kappa \\ S &= M' = EI\kappa' \end{aligned} \tag{3.28}$$

With M the bending moment and EI the bending stiffness.

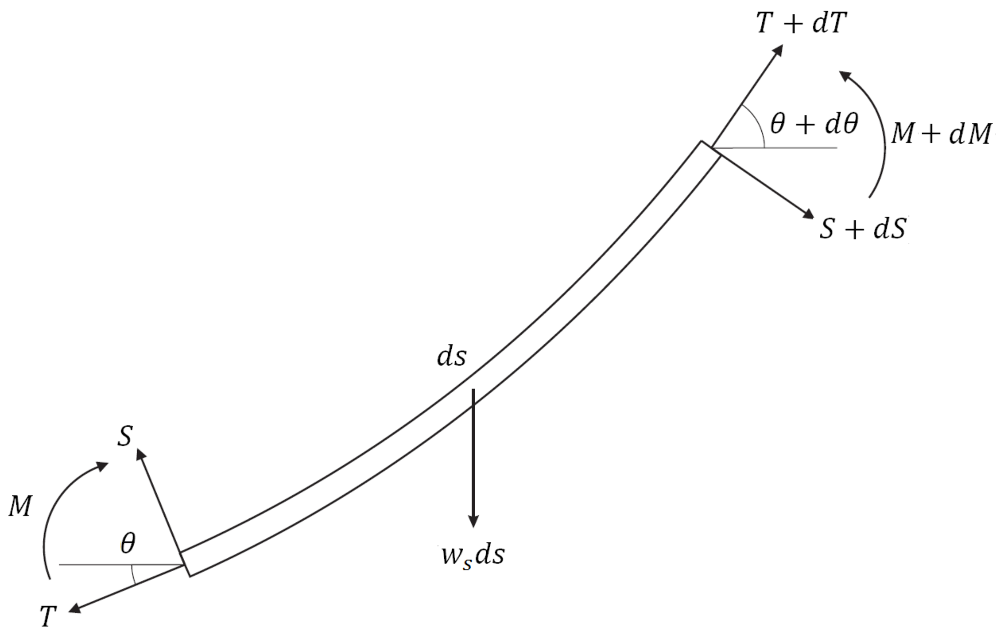

Figure 3-5 Internal loads of a small unsupported bend pipeline segment

Using (3.28), the differential equation of (3.24) is rewritten as a function of θ:

$$T\kappa - EI\kappa'' - w_s \cos\theta = 0 \tag{3.29}$$

Equation (3.29) is known as the nonlinear bending equation. It is valid for pipelines with both small and large deflections and in shallow and deep water. The equation is used in many studies of the static situation of the pipeline catenary and can only be approximated (section 0). Without the bending stiffness term, in equation (3.29), the equation is known as the natural catenary equation (3.43).

$$T\kappa - w_s \cos\theta = 0 \tag{3.30}$$

This equation can be solved exactly, but is inaccurate near the ends of the pipeline However its solution for the span length L_{span} solution and can be used as initial guess for the static state solution. (Jensen, 2010).

3.3 Pipeline integrity

There are multiple failure modes of a tensioned pipeline during s-lay installation. At Allseas the design parameters are adjusted in order to make sure the pipeline is installed safely according to a classification standard (DNV-OS-F101, 2010). Although all failure modes should be prevented, there are two failure modes which limit the pipeline integrity most likely during dynamics. These are fatigue and local buckling criteria (Bai & Bai, 2005).

- Fatigue damage typically occurs due to microscopic cracks in the pipeline. The magnitude of stresses at the pipeline is not directly related for this kind of damage, but the number of stress cycles by repeated loading and unloading. This is known as the cyclic loading which causes the microscopic cracks to grow until failure. A three hours dynamic analysis of the limiting sea states in multiple directions is used to determine the stress cycles. Using material specific S-N curves and Miner's rule, the maximum fatigue damage is determined.

- Local buckling in the pipeline occurs for certain combinations between tension, external pressure and bending moment of the pipeline. The local buckling check of DNV use all three of these quantities with additional factors for safety, material and the quality of the welds (DNV-OS-F101, 2010).

Because fatigue check is depended on the amount of stress cycles over time and the local buckling check is dependent on a limiting stress, the determination of fatigue damage using vessel motion based criteria is more complex than the determination of local buckling. Particularly if the local buckling check could be simplified which will be described in the next two sections. Therefore pipeline integrity due to fatigue damage will be out of the scope in this thesis.

3.3.1 Bending moment

The largest contribution to failure by local buckling is distinctly the bending moment of the pipeline (Jensen, 2010) (Bai & Bai, 2005), (DNV-OS-F101, 2010). In particular the bending moment in the unsupported sagbend of the pipeline catenary is of concern, because this section considered load, while the overbend is often considered displacement controlled (Williams, et al., 2002). In this thesis the focus regarding pipeline integrity is thus bending moment.

The bending moment capacity defines the limiting bending moment of the pipeline which is part of the combined local buckling condition (DNV-OS-F101, 2010). At Allseas the nonlinear moment-curvature relationship is used to define the moment capacity (Figure 3-6).

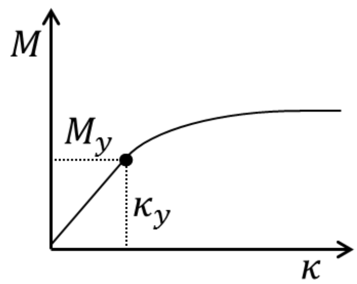

Figure 3-6 moment-curvature relationship

This relationship is mainly dependent on the material and geometry of the pipeline, but also a characteristic amount of axial wall force (tension) in the static and dynamic situation (DNV-OS-F101, 2010). The elastic region of the moment-curvature relationship is limited by the yield bending moment which can be determined with equation (3.31) (DNV-OS-F101, 2010).

$$M_y = \frac{2\sigma_y I}{D_o} \tag{3.31}$$

With M_y and σ_y respectively the yield bending moment and yield stress, I the polar second moment of inertia and D_o the outer diameter of the steel pipeline. The yield bending moment is a conservative limit for the bending moment, because the real moment capacity is larger. Nonetheless the yield bending moment can be used as a soft limit for the bending moment (Bai & Bai, 2005).

3.3.2 Equivalent strain

Besides bending moment another often used parameter regarding local buckling is the equivalent strain which is derived by applying the von Mises yield criterion in a simplified form. Radial strain and shear strain are both assumed small and neglected in this simplification. Hence the equation for equivalent strain is (DNV-OS-F101, 2010):

$$\varepsilon_{\mathrm{vm}} = \sqrt{(\varepsilon_t + \varepsilon_c)^2 + \varepsilon_h^2 - (\varepsilon_t + \varepsilon_c)\varepsilon_h} \tag{3.32}$$

With

$\varepsilon_{\mathrm{vm}}$ the equivalent von Mises strain
ε_t the tensile strain
ε_h the hoop strain
ε_c the vector sum of bending strain ε_{b}

The tensile strain ε_{t} and hoop strain ε_h are determined with respectively equation (3.33) and (3.34) (DNV-OS-F101, 2010).

$$\varepsilon_t = \frac{T + A_e \rho h}{E A_s} \tag{3.33}$$

$$\varepsilon_h = \frac{D_e \rho h}{2 E t_{w,nom}} \tag{3.34}$$

With

A_e the external cross section of the pipeline
$A_s$the steel cross section of the pipeline
h the water depth
$t_{w,nom}$ the nominal wall thickness

The (nonlinear) bending strain in the local x, y or z direction of the pipeline is determined with equation (3.39) (Bai & Bai, 2005). The Ramberg & Osgood parameters depend on the pipe properties. Allseas uses in-house developed software called "BENDPIPE" which iteratively determines the material specific moment-curvature relationship and specific Ramberg and Osgood parameters.

$$\varepsilon_{b,\mathrm{x;y;z}} = \frac{\sigma_y}{E}\left[\frac{M}{M_y} + R_1\left(\frac{M}{M_y}\right)^{R_2}\right]\frac{M_{\mathrm{x;y;z}}}{M} \tag{3.35}$$

With

ε_b the bending strain
R_1, R_2 the Ramberg & Osgood parameters
σ_y the yield stress which is defined to be the stress which gives a total strain of 0.5%

The vector sum of bending strain is the largest contribution to the equivalent strain (Bai & Bai, 2005), (DNV-OS-F101, 2010), (Ogink, 2001). Therefore the bending moment will be primarily used as limiting parameter for the pipeline integrity regarding local buckling throughout this thesis. The equivalent strain will be used for validation.

3.4 Modelling dynamic effective tension

In the previous sections and the introduction, the relation between tension and bending moment in the sagbend was introduced. The vessel in combination with the tensioners applies a safe amount of tension on the pipeline so the pipeline does not buckle during installation. Due to vessel motions the required amount of tension fluctuates. Less tension leads to higher bending moments in the sagbend. Vessel motions cause compressive axial motions in the pipeline which result in compressive axial tension fluctuations and thus fluctuations of bending moments.

For deep water pipelay operations, the axial motions of the pipeline at LOP are almost equal to the vertical motion of the pipeline at LOP $\mathrm{r}_{\mathrm{Z},LOP}(t)$, because of the large unsupported span length and large weight of the pipeline which influence the departure angle θ. If the departure angle is assumed to be close to 90°, the dynamic effective tension $T_{\mathrm{dyn}}(t)$ relating vertical motions of the pipeline can be modelled with a mass-spring-dashpot system (Nonemaker, 2012) described in Figure 3-7 and equation (3.36).

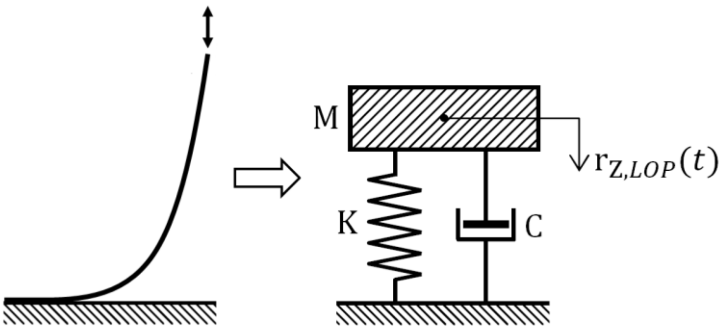

Figure 3-7 mass spring dashpot representation of the effective tension at lift-off point

$$T_{\mathrm{dyn}}(t) = \mathrm{M}\,\ddot{\mathrm{r}}_{\mathrm{Z},LOP}(t) + \mathrm{C}\,\dot{\mathrm{r}}_{\mathrm{Z},LOP}(t) + \mathrm{K}\,\mathrm{r}_{\mathrm{Z},LOP}(t) \tag{3.36}$$

with M the mass coefficient [kg], C the damping coefficient [kg/s], K the spring coefficient [kg/s^2] and $\mathrm{r}_{\mathrm{t},IP}(t)$ the axial pipeline motion at LOP [m].

For deep water pipelay operations it can be assumed that the dynamic tension at LOP is about equal to the dynamic tension in the last tensioner at each point of time. Thus only large variations between different positions at the unsupported pipeline will occur. A constant static effective top tension is given by the tensioners which are modelled on the brakes. For only vertical displacements of the pipeline at LOP, the spring stiffness K is linearly related to the submerged weight of the pipeline (Nonemaker, 2012). For horizontal displacements, the stiffness is also dependent of water depth and effective bottom tension (Jensen, 2010).

$$\mathrm{K} = \frac{dT_{\mathrm{sta}}}{d\mathrm{r}_{\mathrm{Z},LOP}} \tag{3.37}$$

Newton's 2nd law states that the total inertia force of the pipeline at the stinger tip is equal to the product of its mass and acceleration. Thus for a pipeline leaving the stinger perpendicular to the sea surface level (90°), the axial pipeline acceleration is linear related to the total mass M of the unsupported pipeline. The total mass at LOP has an inertia term of the pipeline mass and an added inertia term of the surrounded fluid. For the unsupported pipeline, the unit inertia load in normal direction $f_{I,\mathrm{n}}$ is equal to the inertia load of the pipeline and the surrounding fluid of equation (3.19) which yields:

$$f_{I,\mathrm{n}} = (w_s + \rho C_a A)\ddot{\mathrm{r}}_{\mathrm{n}}(t) \tag{3.38}$$

If the inertia load in normal direction is integrated over the span length (L_{span}) and translated to the axial direction at LOP, one finds the total inertia load at LOP. The inertia coefficient M can be found by dividing the total inertia load $F_I(t)$ over the acceleration of the pipeline at LOP:

$$\mathrm{M} = \frac{F_I(t)}{\ddot{\mathrm{r}}_{LOP}(t)} \tag{3.39}$$

The damping coefficient C has nonlinear terms including the effects of the nonlinear fluid drag load. To find a linear relationship, the damping should be linearized. A damping coefficient based on linearized fluid drag can be derived analytically and will be discussed in section 3.5.4.

3.5 Numerical analysis

To use the proposed model of previous section in an analytical way is quite complex. Also in order to reach the thesis goal a more advanced dynamic model should be made which includes the influence of the different vessel motions of section 3.1 and the static shape based on the nonlinear bending equation derived in section 3.2.6. To effectively describe the relation between pipeline motions and vessel motions with regards to the sagbend bending moment numerical methods are used.

3.5.1 Beam elements

In order to solve the pipelay problem numerically, the pipeline can be modelled by a finite number of beam elements. A simple beam element can be represented as a 2D linear Euler-Bernoulli beam with length l which is presented in Figure 3-8. It has in total six degrees of freedom. This means that the matrices for mass, damping and stiffness have six columns and six rows. The length of the beam l is in the local x-direction.

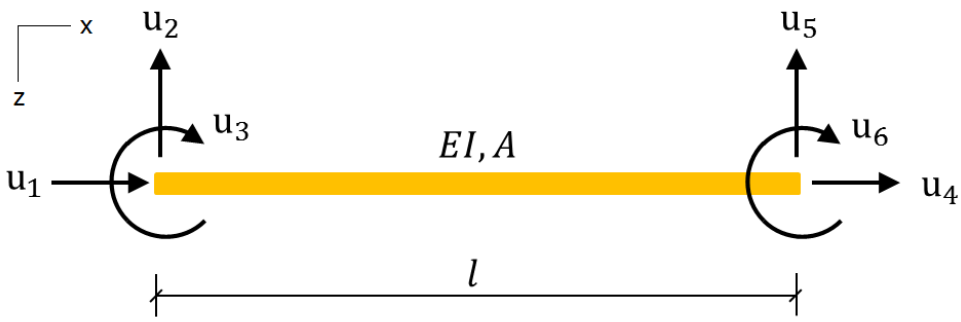

Figure 3-8 Euler-Bernoulli beam element with six degrees of freedom

The stiffness matrix of a single element has two different terms. The first term $\boldsymbol{k}_E$ comes from the combined elastic stiffness (without shear deformations) containing both axial and bending load terms. It is expressed as (Cook, et al., 1989):

$$\boldsymbol{k}_E = \begin{bmatrix} \frac{EA}{l} & & & & & \\ 0 & \frac{12EI}{l^3} & & & SYM & \\ 0 & \frac{-6EI}{l^2} & \frac{4EI}{l} & & & \\ \frac{-EA}{l} & 0 & 0 & \frac{EA}{l} & & \\ 0 & \frac{-12EI}{l^3} & \frac{6EI}{l^2} & 0 & \frac{12EI}{l^3} & \\ 0 & \frac{-6EI}{l^2} & \frac{2EI}{l} & 0 & \frac{6EI}{l^2} & \frac{4EI}{l} \end{bmatrix} \tag{3.40}$$

Besides elastic deformation of the material, the beam element also changes its geometry when subjected to an external load. The change in geometry will affect the equilibrium. This is primarily an issue for large displacements due to large axial tension forces. To derive the geometric stiffness matrix of the beam element, the finite strains are investigated. In the X direction these are expressed with a linear term and second order displacement term:

$$\varepsilon_{xx} = \frac{\partial \mathrm{r_x}}{\partial \mathrm{x}} + \frac{1}{2}\left[\left(\frac{\partial \mathrm{r_x}}{\partial \mathrm{x}}\right)^2 + \left(\frac{\partial \mathrm{r_z}}{\partial \mathrm{x}}\right)^2\right] \tag{3.41}$$

With ε_{xx} the total strain in x direction. $\mathrm{r_x}, \mathrm{r_z}$ are the displacements of the beam in the local x and z direction. Equation (3.41) is derived from the Cauchy-Green strain tensor (Cook, et al., 1989). The axial strains are constant over the cross-section according to Navier's hypothesis. Where the first order term is related to the elastic stiffness, the second order terms in (3.41) are responsible for the nonlinear axial strains (Larsen, 1990). The lateral second order term contributes to the geometric stiffness $\boldsymbol{k}_G$ given in equation (3.42)

$$\boldsymbol{k}_G = \frac{F}{l}\begin{bmatrix} 0 & & & & & \\ 0 & \frac{6}{5} & & & SYM & \\ 0 & \frac{-l}{10} & \frac{2l^2}{15} & & & \\ 0 & 0 & 0 & 0 & & \\ 0 & \frac{-6}{5} & \frac{l}{10} & 0 & \frac{6}{5} & \\ 0 & \frac{-l}{10} & \frac{-l^2}{30} & 0 & \frac{l}{10} & \frac{2l^2}{15} \end{bmatrix} \tag{3.42}$$

The geometric stiffness matrix represents linearization of the nonlinear rope effect for a constant axial force F. The effects to the curvature of the beam are included in the stiffness. For the geometric stiffness of the beam element only the axial strains are of interest, because the lateral strains are small for beams under large tension. Note that if a small element length is used, the geometric stiffness has minor influence on the structural response behaviour. However if the pipeline catenary is modelled as a single hinged Euler-Bernoulli beam, the geometric shape does have significant influence on the bending behaviour (Chatjigeorgiou, 2013). The geometric influence is a phenomenon what will be investigated during model tests.

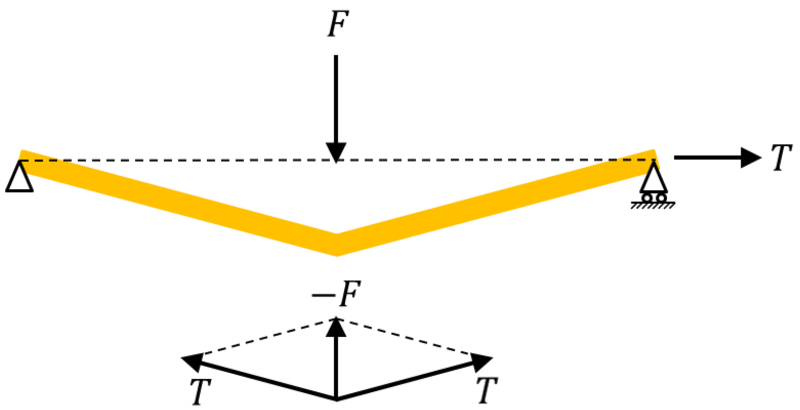

Figure 3-9 Rope effect of a 2D simple supported beam with a point load

The total stiffness matrix of 2D linear Euler-Bernoulli beam can be found by the sum of the different stiffness's.

$$\boldsymbol{k}_{,j} = \boldsymbol{k}_{E,j} + \boldsymbol{k}_{G,j} \tag{3.43}$$

By a transformation matrix $\mathbf{T}_j$, the stiffness can be transformed to the global system. Another matrix $\boldsymbol{a}_j$ is used to transform the local DOFs to the global DOFs. By summing up all the elements the global stiffness matrix $\mathbf{K}$ is obtained.

$$\mathbf{K} = \sum_j \boldsymbol{a}_j^T\, \mathbf{T}_j \boldsymbol{k}_{,j} \mathbf{T}_j^T \boldsymbol{a}_j \tag{3.44}$$

For modelling pipelay operations, where large rotations and displacements occur, beam elements without displacement limitations are needed. In a 3D reference system (beam element with 12 DOFs) this can be achieved by using a ghost reference system. In such system two local reference systems are added for the rotations of the elements at each deformed element's end (Larsen, 1990).

3.5.2 Static Analysis

In the static analysis the structural response is approximated for the loads on $t = 0$. Consequently the unknowns of the static equilibrium are approximated.

$$\mathbf{Ku} = \mathbf{F} \tag{3.45}$$

In other words the nonlinear bending equation (3.29) for all the elements is solved. This equation is of the second order, but the free span length L and the reaction of the seabed F_{seabed} are also unknown which makes a total of four unknowns. Therefore no exact solutions are known. The changing boundary layers near the ends of the pipeline where the stiffness is dominating can be described by using a perturbation method (Plunkett, 1968) to approximate the four unknowns (Dixon & Rutledge, 1968), (Rienstra, 1987). This is known as the stiffened catenary. For S-Lay pipelay operations the stiffened catenary approach can give accurate results for the static configuration compared to the method which will be used in commercial packages (Li, et al., 2010). Commercial packages use a shooting method to approximate the static analysis. In the shooting method first the values of the missing data (loads and displacements) in the matrices of equation (3.45) are estimated (e.g. using the natural catenary equation). After the estimate an iterative procedure of transfer matrices can be used to converge to the solution (Larsen, 1990). Hence the shooting procedure is less time consuming than the FEM for static analysis. The found static configuration is the starting situation for the dynamic analysis.

3.5.3 Dynamic equilibrium

The full 3D dynamic equilibrium of an offshore pipeline catenary can be described by ten analytical nonlinear partial differential equations with ten unknowns (Chatjigeorgiou & Mavrakos, 2010). Because of its complexity, this thesis uses a numerical approach for which the dynamic equilibrium is typically written as

$$\mathbf{M\ddot{u}} + \mathbf{C\dot{u}} + \mathbf{Ku} = \mathbf{F}(t) \tag{3.46}$$

The mass matrix $\mathbf{M}$ is dominated by the mass of the structure itself and the added mass of the surrounded fluid (hydrodynamic mass). The hydrodynamic mass is unlike the structural mass dependent on the direction of the displacements. This nonlinearity can only be solved in time domain solutions (Larsen, 1990). The total mass is lumped on the nodes, which means that for each single element the mass is on summed on the diagonal of the mass matrix and all other coupling effects are neglected. This will cost significant less computational time without notable affection to the accuracy.

In section 3.2.2 was described that the hydrodynamic drag load contributes to the damping by its relative velocity squared term. Also damping from seabed and structural damping of the system occur. To specify the damping matrix $\mathbf{C}$ on such effects is a difficult procedure. Generally, the structural damping is specified to be proportional to the stiffness or mass matrices known as Rayleigh structural damping. For offshore pipelay where the hydrodynamic drag loads give large damping effects there is no need to specify structural damping (Orcina, 2014). Therefore the damping matrix $\mathbf{C}$ is corresponding to the hydrodynamic drag loads which are related and in phase with the velocity vector.

3.5.4 Linear dynamic analysis

Because of the nonlinear effects of the damping and mass matrices, the dynamic response of the pipeline is also nonlinear. Nonlinear behaviour during S-lay operations originates from fluid drag, geometry, seabed, material and deadband of the tensioners (Callegari, et al., 2003). Since the seabed is modelled linear and the deadband is discarded, this leaves nonlinear effects by geometry, material and fluid drag. To find the linearized dynamic equilibrium, one could use the frequency domain method. It is mainly popular for problems with many DOFs exposed to stochastic harmonic loads. The transformation between first order waves and vessel motions described in section 3.1 is a famous frequency domain solution.

Using the frequency domain method the load matrix $\mathbf{F}(t)$ is described by its complex notation.

$$\mathbf{M\ddot{u}} + \mathbf{C\dot{u}} + \mathbf{Ku} = \mathbf{B} \cdot e^{i\omega t} \tag{3.47}$$

The complex response vector $\mathbf{b}$ can be found by rewriting equation (3.48)

$$[\mathbf{K} - \omega^2\mathbf{M} + i\omega\mathbf{C}]\mathbf{b} = \mathbf{B} \tag{3.48}$$

The linear response vector can also be written by

$$\mathbf{b}(\omega) = \mathbf{H}(\omega) \cdot \mathbf{B}(\omega) \tag{3.49}$$

with $\mathbf{H}$ equal to $[\mathbf{K} - \omega^2\mathbf{M} + i\omega\mathbf{C}]^{-1}$. For each load excited discrete frequency of the load vector, equation (3.47) should be solved. Because the response is linear the damping matrix $\mathbf{C}$ should contain linearized terms. Fortunately the fluid drag (which is assumed to be the largest contribution to nonlinear behaviour) can be effectively linearized. The linearized drag force can be determined with an equivalent damping coefficient $\mathrm{c_{eq}}$.

$$f_{D,\mathrm{eq}}(t) = \mathrm{c_{eq}} \mathrm{v_n}(t) \tag{3.50}$$

The normal velocity of the pipeline at a point along the pipeline $\mathrm{v_n}(t)$ is a harmonic motion equal to

$$\mathrm{v_n}(t) = \mathrm{v_{n,a}} \cos(\omega t) \tag{3.51}$$

Because the dissipated energy of the nonlinear and linear drag forces in one harmonic oscillation with period T should be equal, the following equation is given (Larsen, 1990).

$$\int_0^{\mathrm{T}} \left[f_{D,eq}(t) \cdot \mathrm{v_n}(t)\right] dt = \int_0^{\mathrm{T}} \left[f_D(t) \cdot \mathrm{v_n}(t)\right] dt \tag{3.52}$$

Solving equation (3.52) will result in the equivalent drag coefficient $\mathrm{c_{eq}}$ (Larsen, 1990).

$$\mathrm{c_{eq}} = \frac{4}{3\pi} \rho C_D D_e \mathrm{v_{n,a}} \tag{3.53}$$

To know the amplitude of the normal velocity in the pipeline, one needs to know the dynamic response of the pipeline first. This means that the damping coefficient from equation (3.53) should be solved repeatedly and the linearized drag should change at each intermediate step. Therefore when using the frequency domain method frequently FDM is added known as FDFD. FDM discretises the governing differential equations into a grid. For each intermediate step the equivalent drag can be determined.

Multiple research studies using FD or FDFD approaches to linearized dynamics of offshore pipelines and risers are performed. Basically only for small excitations of the pipeline (low frequency and small amplitudes) and thus small dynamic angles and displacements the linearized approach give accurate results (Brewer & Dixon, 1970), (Suzuki & Jingu, 1982), (Shekker, et al., 1984) , (Clauss, et al., 1992). However more recent studies conclude that significant additional nonlinear behaviour occur (Chatjigeorgiou, 2008) which in the case for bending moments result in larger nonlinear behaviour than its linear equivalent. As a result the linear dynamic analysis described in this section is not suitable for an accurate relation between vessel motions and pipeline integrity and a full nonlinear dynamic analysis is needed.

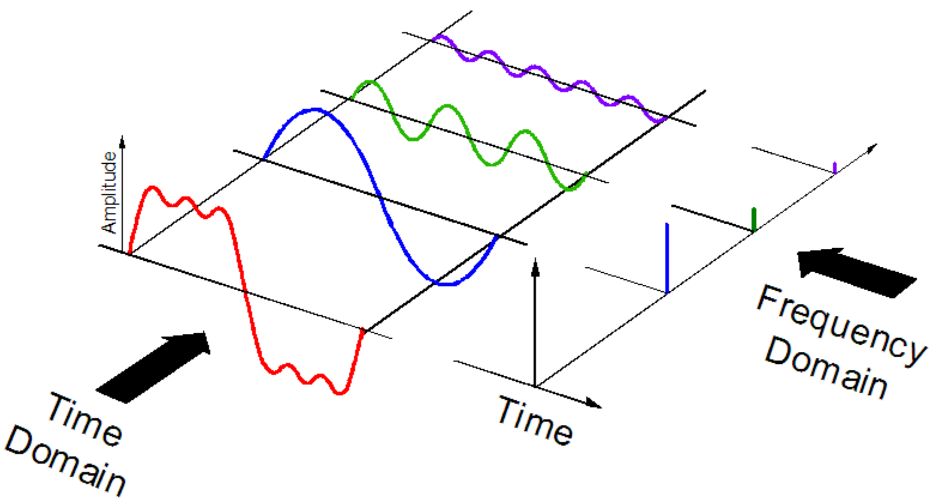

Figure 3-10 Schematic difference between FD and TD

3.5.5 Nonlinear dynamic analysis

In the offshore industry nonlinear dynamic analyses are performed to validate the design parameters for offshore pipelay, mooring cables or risers. The requirements are specified in the classification standards (DNV-OS-F101). The FDFD method which is used for linear dynamics can also be used for higher order nonlinear analyses. For instance (Chatjigeorgiou, 2013) approximated the dynamics of the pipelay catenary up to the second order. His conclusion was that for large excitations, the second order effects for dynamic bending moments may exceed the first order dynamic bending moments.

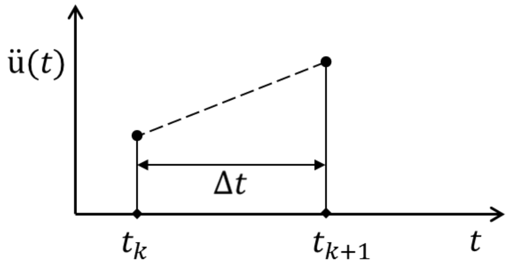

Figure 3-11 time integration during one time step (Larsen, 1990)

More popular is the use TD methods to do a full nonlinear dynamic analysis. The main advantages in comparison with the frequency domain method are the capability of determining transient loads and nonlinear effects (Larsen, 1990). By using FEM, the loads acting on each node of the beam element in the system are calculated and subsequently used to create a local equation of motion for every segment and node in the system. The acceleration follows from the dynamic equilibrium which can be rewritten to equation (3.54)

$$\ddot{\mathrm{u}}(t) = \frac{1}{\mathrm{M}}[\mathrm{F}(t) - \mathrm{C}\dot{\mathrm{u}}(t) - \mathrm{K}\mathrm{u}(t)] \tag{3.54}$$

The local equation of motion including the displacement and velocity is solved by step by step integration of the acceleration at the end of each time step Δt using the equations of (3.55) taken from (Larsen, 1990).

$$\begin{aligned} \dot{\mathrm{u}}_{k+1} &= \dot{\mathrm{u}}_k + \int_{t_k}^{t_{k+1}} \ddot{\mathrm{u}}_k(t)dt \\ \mathrm{u}_{k+1} &= \mathrm{u}_k + \int_{t_k}^{t_{k+1}} \dot{\mathrm{u}}_k(t)dt \end{aligned} \tag{3.55}$$

There are multiple FEM integration methods to solve the integrals in the equations of (3.55). The difference between them is the method to assume the time history of acceleration during Δt. A frequently used integration method in the structural analysis is the Newmark-β family of methods (Larsen, 1990). In this thesis the Generalized-α integration scheme (Chung & Hulbert, 1993) is used. This is a modified Newmark-β method. The main advantage of this scheme is that it minimises the low frequency damping by specifying the level of high frequency dissipation.

The solving process of the local equations of motions is repeated for each predefined time step in the total predefined simulation time. This leads to large simulation times for stochastic problems. Therefore for linear stochastic problems (Gaussian distributed), FDM is preferred.

3.5.6 Modal analysis

To find the mode shapes of an undamped system, the damping matrix $\mathbf{C}$ in the equation of motion is neglected. Therefore the equation of motion of the elements for N degrees of freedom can be rewritten to:

$$\mathbf{M}\ddot{\mathbf{u}}(t) + \mathbf{K}\mathbf{u}(t) = 0 \tag{3.56}$$

Because no damping is involved, the solution of equation (3.56) should be harmonic and can be expressed into the form of equation (3.57)

$$\mathbf{u}(t) = \mathbf{u}_\mathrm{a}\sin(\omega t) \tag{3.57}$$

Substituting equation (3.57) in the undamped equation of motion (3.56) yields:

$$-\mathbf{M}\omega^2\mathbf{u}_\mathrm{a}\sin(\omega t) + \mathbf{K}\,\mathbf{u}_\mathrm{a}\sin(\omega t) = 0 \tag{3.58}$$

If the vector $\mathbf{u}(t)$ contains only one cell ($N = 1$) and thus one DOF, only one solution exists which is $\omega = \sqrt{\mathrm{K}/\mathrm{M}}$. In reality the pipeline has unlimited degrees of freedom ($N = \infty$). In a FEM analysis the undamped equation of motion contains N (finite) elements which mean there are N degrees of freedom and N natural frequencies. Because the modal analysis uses a linear approach, the modal analysis can also be obtained using FDM (Callegari, et al., 2003). Nevertheless FEM give fast and accurate results. For simple problems like a simple linear Euler-Bernoulli beam bending in one direction, the modal analysis can be determined analytical. This is presented in Appendix A and will be of use in the next chapter.

3.6 Chapter conclusion

In this chapter the loads of a pipeline during installation are derived and/or described with emphasis on effective tension and bending moments by vessel motions and hydrodynamic loads. This is because vessel motions cause the tension fluctuations which are related to bending moment fluctuations in the sagbend. Bending moments primarily influence the pipeline integrity with regards to local buckling. The yield moment can be used as a conservative soft limit for the pipeline. A more accurate parameter to limit local buckling is the equivalent von Mises strain.

Vessel motions in six DOF can be represented as linear responses to irregular sea states with the use of linear theory. Vessel motions apply dynamic tension on the pipeline at LOP.

For deep water operations, the vertical pipe motions at LOP can be related to dynamic tension by using a model with assumed equality between axial pipe motions and vertical pipe motions. Because damping by fluid drag primarily affect the pipeline in normal (thus horizontal) direction and inertia affects the pipeline only in vertical direction, the inertia effects can be neglected at TDP which is also the case for damping effects at LOP when related to tension.

Full dynamic approximations contain multiple partial nonlinear differential equations which need to solve iteratively. These equations could be linearized by linearizing the hydrodynamic drag before using the FDFD method. Although frequency domain methods are preferred for stochastic and linear problems, the time domain method using FEM is preferred for a full dynamic analysis of an offshore pipeline installation. This is because the modelling involves higher order nonlinearities which have significant contribution to the bending behaviour in the sagbend and thus the pipeline integrity.

4.0 EXPERIMENTAL MODEL SETUP

In this chapter three models (base cases) are introduced which are developed with OrcaFlex. Also static analyses and modal analyses of these models are performed and assessed to describe the differences in their expected dynamic behaviour.

4.1 General model setup properties

The base cases which are used to analyse the relationship between vessel motions and pipeline integrity are modelled using OrcaFlex (version 9.8c) by Orcina. This is a renowned commercial software package for modelling offshore marine systems. It is capable of performing and plotting dynamic analyses by using FEM. At the pipeline engineering department of Allseas Engineering, OrcaFlex is used to simulate and design the installation of different kinds of marine structures.

The general model properties used to model offshore pipeline operations (which are introduced in chapter 3.0) are presented in Table 4-1. These properties are used for all simulations in OrcaFlex. Note that a very small drag coefficient C_D for axial direction is taken. This value is determined by OrcaFlex through the influence of skin friction (Orcina, 2014).

Type	Quantity		Value
Environmental constants	ρ	[kg/m^3]	1025
	g	[m/s^2]	9.81
	μ	[kg/(m·s)]	$1.32 \cdot 10^{-9}$
Hydrodynamic coefficients	C_D in normal and binormal direction	[-]	1.2
	C_D in axial direction	[-]	0.008
	C_a in normal and binormal direction	[-]	1.0
	C_a in axial direction	[-]	0
Stiffness's	K_{seabed}	[kN/m^3]	100
	$K_{support}$	[kN/m]	70000

Table 4-1 General model properties used in OrcaFlex

OrcaFlex is capable of using the Generalized-α integration scheme (section 3.5.5) for the dynamic analyses through the implicit solving method (Orcina, 2014). The FEM properties used in OrcaFlex are presented in Table 4-2. The spacing between the pipeline supports lead to convergence difficulties for large element lengths. However small element length results in time-consuming computation times. Therefore the element length of the pipeline is chosen to be shorter only in the first meters (overbend).

Description			Value
Element length	overbend	[m]	5
	sagbend	[m]	10
Time step		[s]	0.10
Integration tolerance		[-]	$25 \cdot 10^{-6}$
Level of high frequency dissipation		[-]	0.4

Table 4-2 FEM properties used in OrcaFlex

In this thesis MATLAB coding is used to control the input and output of the OrcaFlex data and simulation files through the API of OrcaFlex. Therefore this control can be automated which is convenient when working with a large amount of simulations. MATLAB scripts are used to export the results of the OrcaFlex simulations into matrices. These matrices are used to find the extreme values in a TD simulation and to plot results into line, scatter polar and contour plots.

Figure 4-1 Block diagram of the sensitivity study roadmap

4.2 Base cases

Three base cases will be used to investigate the relationship between vessel motions and the bending behaviour in the sagbend of the pipeline. The base cases are derived from real projects executed with "Solitaire" which is one of the largest pipelay vessels in the world (Figure 4-2). There is chosen for three different water depths to test and investigate relationships between vessel motions and pipeline integrity. This is because water depth has a large influence on the dynamic behaviour of pipelines (Jensen, 2010). Base case number one (BC1) is an ultra-deep water case in the Gulf of Mexico which installs an 18-inch diameter pipeline in a water depth which exceeds 2.5 km below sea surface level. The pipeline can be categorised as long and slender. The base cases BC2 and BC3 are both from the same project which will be laid in the Norwegian Sea. The 36-inch diameter pipeline can be categorised heavy and stiff. The major difference between BC2 and BC3 is the water depth which is deep for BC2 and shallow for BC3. The pipeline properties of the three base cases are categorised in Table 4-3.

All three base cases use the same type of classified steel (API-5L X65), but with different moment capacity properties. The nonlinear behaviour is included in OrcaFlex by importing specific stress-strain curves for the different pipelines. The linear region of the stress-strain curve can be defined as a nominal bending stiffness (EI_{nom}). Note that EI_{nom} is much larger for BC2 and BC3 compared to BC1. This is mainly a result of the larger diameter. Therefore the yield moments are also much larger for BC2/BC3 which is about 4.5 times the yield moment of BC1.

The axial stiffness's are modelled linear, because their nonlinearities are negligible (Orcina, 2014). Consequently all three base cases use the same Young's modulus ($E = 207$ [GPa]) for the axial stiffness's. The three different pipelines all include a layer of anti-corrosion coating. BC2 and BC3 also have a significant amount of concrete coating which force the pipeline not being buoyant during installation.

Description			Value		
Base Cases			BC1	BC2	BC3
Water depth		[m]	2503	700	92
D_o		[mm]	457.2	911.9	914.9
Wall Thickness		[mm]	27.00	28.90	30.50
D_e		[mm]	458	1019.9	1102.9
Material grade		[API – 5L]	X65		
σ_y		[MPa]	448 MPa		
M_y		[kNm]	1661	7685	8124
EI_{nom}		[MNm^2]	175.4	1619.1	1699.7
Anti-corrosion coating	Type		FBE	PE	
	Thickness	[mm]	0.4	4	4
	Density	[kg/m^3]	1300	900	900
Concrete coating	Thickness	[mm]	-	70	90
	Density	[kg/m^3]	-	3050	3050
Weight in air	Empty	[N/m]	2817.4	9762.4	15416.0
	Flooded	[N/m]	4101.3	15522.9	21174.4
Submerged weight	Empty	[N/m]	1160.9	1548.2	5809.6
	Flooded	[N/m]	2444.7	7308.7	11568.0

Table 4-3 Pipeline properties of the three base cases

Figure 4-2 Solitaire pulling a 30" diameter pipeline near the Shetland Islands

For most pipeline operations the stinger setting is not changed between laying depths. Consequently if a stinger is used for a shallow water case, the same stinger setting is used to lay pipeline in deep water. The pipeline in the cases BC2/BC3 force to have a small departure angle because of the minimal stinger tip separation, which is a safety margin between the stinger tip and the pipeline in order to get no loads on the stinger tip. Besides the stinger tip separation, the external loads on the pipeline, suspended length of the pipeline and the properties of Table 4-3 are responsible for the departure angle. For the ultra-deep BC1 which is long, slender and less stiff compared to the other cases, the static departure angle is almost perpendicular to the mean surface water level. In the situation of BC2, the static departure angle is smaller. Because of the deep water depth and large bending stiffness, the pipeline's static length is relatively large in order to bend the pipeline on the seabed. The static departure angle is almost half in comparison with BC1. The stiff short pipeline in the shallow water of BC3 results in a small departure angle of 21°. The stinger and tensioner settings and the key results from the static situation of the base cases with optimised tension are presented in Table 4-4.

Description			Value		
Base Cases			BC1	BC2	BC3
Vessel			Solitaire		
Stinger	Length	[m]	140	140	
	Radius	[m]	120	240	
Tensioner mode			Brake	Compensating	
Nominal effective top tension		[kN]	3540	4200	4450
Nominal effective bottom tension		[kN]	596	2960	3712
Static suspended length		[m]	2897	1785	368
Static departure angle		[deg]	81	39	21
Static max bending moment SB		[kNm]	332	774	2518
M_{sta} / M_y		[%]	20	10	31

Table 4-4 Properties of pipelay model and the associated static approximation for all three base cases

If BC2 with BC3 are compared, one notices that BC3 has a static bending moment which is 31% of the yield moment compared to 10% for BC2. Due to the smaller water depth and larger submerged weight, the maximum static bending moment increases. More tension is needed to decrease the bending moment. Larger tension also results in a smaller departure angle. The different pipeline of BC1 is less stiff due to the smaller diameter. Therefore the yield moment is also smaller. The maximum static bending moment is 20% of the yield moment (section 3.3.1).

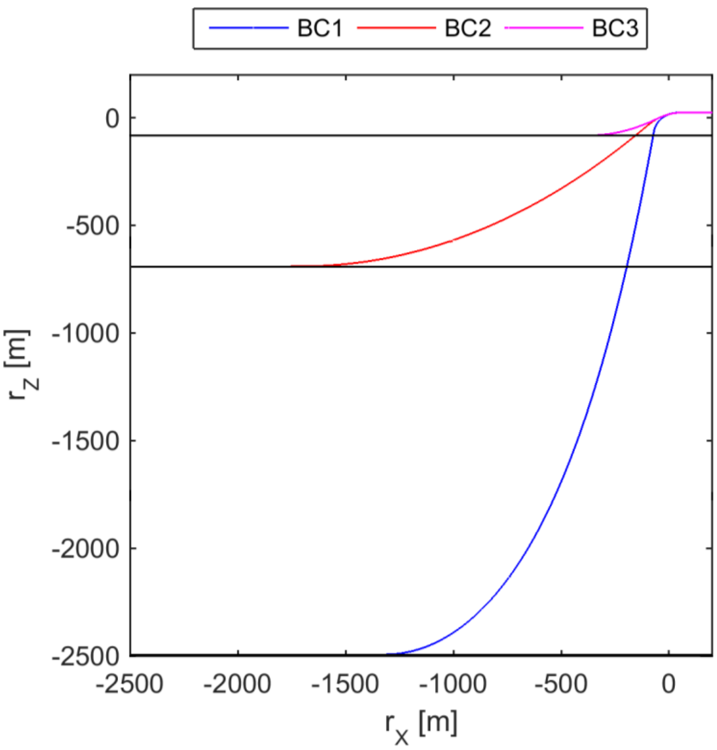

Figure 4-3 S-Lay catenary shapes of the base cases at different water depths (XZ-plane)

In the situation of BC1 the tensioners are modelled on the brakes. This means that during pipelay the tensioners are on their brakes between pulls (paying out lengths of pipeline). When laying pipeline, the tensioners pay out and then brake again which results in dynamic tension of the pipeline (modelled in section 3.4). For BC2 and BC3, this so-called deep water lay mode cannot be used, because the expected dynamic tension exceeds the tension capacity. By using fully compensating tensioners, the dynamic tension is zero and the suspended pipeline fluctuates in length.

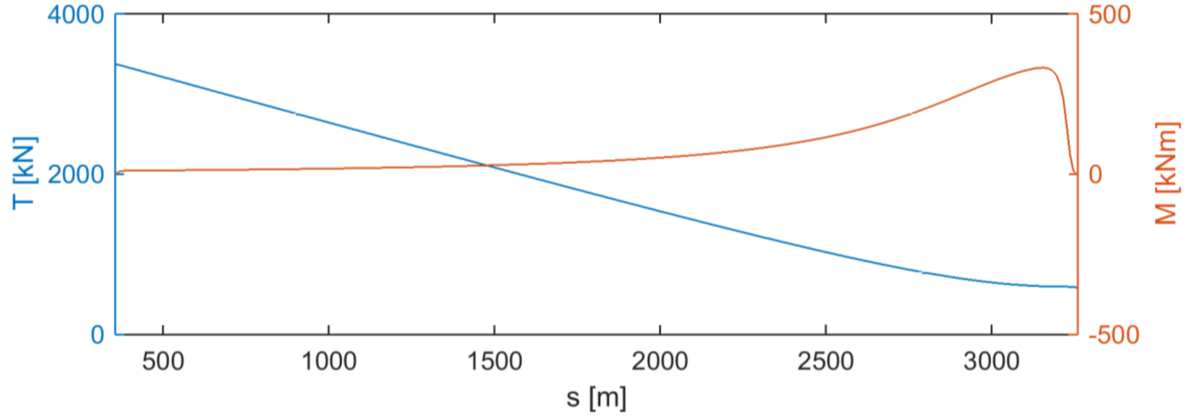

Figure 4-4 Tension and bending moment along the unsupported span length (BC1)

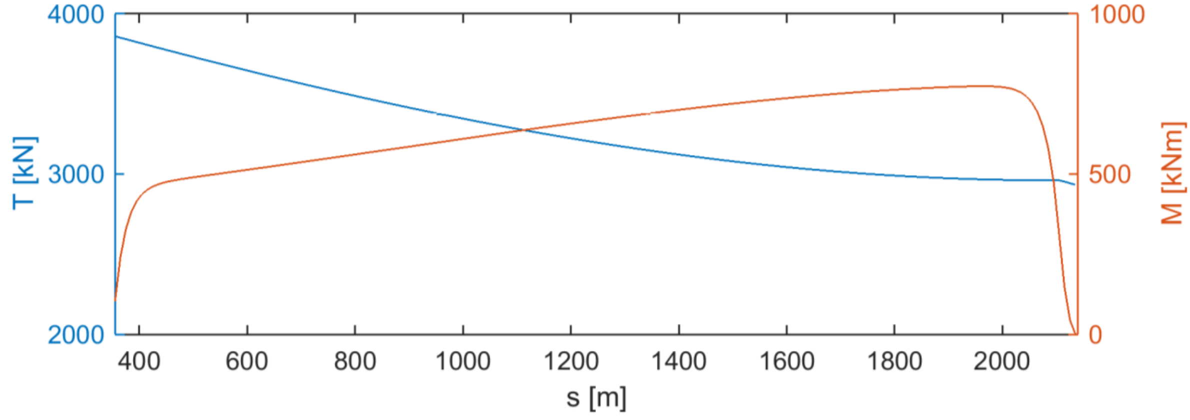

Figure 4-5 Tension and bending moment along the unsupported span length (BC2)

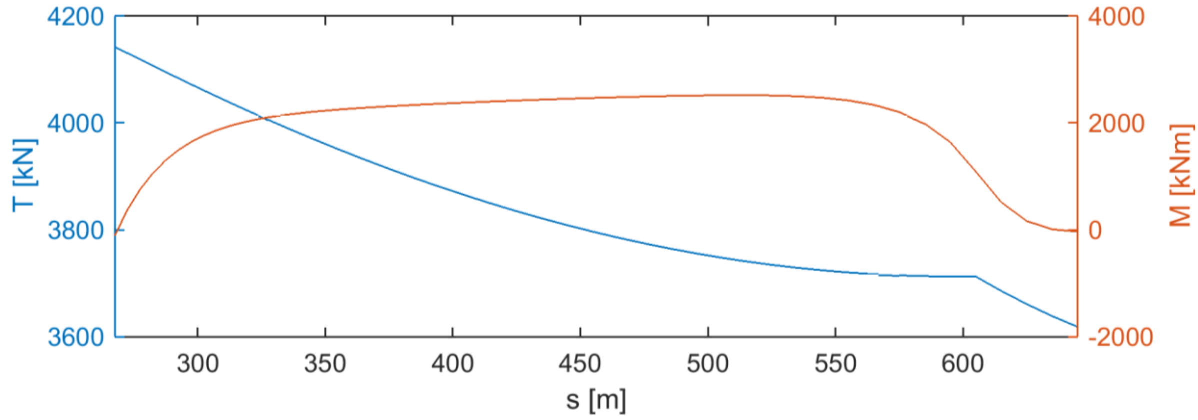

Figure 4-6 Tension and bending moment along the unsupported span length (BC3)

In the static situation of BC1, the large slender pipeline and large departure angle result in small bending moments in the area of the inflection point and large in in the TDA (Figure 4-4). When the effective tension decreases along the span length (through the pipeline weight), the bending moment increases. This effect also occurs for the other two base cases, but less profound. In BC2 the less slender pipeline with moderate departure angle already has a significant amount of bending moment in the area around the inflection point (Figure 4-5). Still the maximum static bending moment occurs in the TDA. In BC3 the pipeline is very stiff and the departure angle is small causing the pipeline to behave like an almost straight simply supported beam. The maximum static bending moment occurs between the middle and end of the unsupported span (Figure 4-6).

4.3 Modal analysis of the base cases

OrcaFlex is capable to perform a full modal analysis by using equation (3.56) for a static converged model. For all three base cases, the first five natural frequencies for the in-plane modes are shown in Table 4-5 at the next page. Note that the first in-plane mode shape is disappeared. This is because the catenary shape in the static situation is already bent which replaced the first mode shape. The deformations of the pipeline will cause axial strains in the beam and lead to an increase of the in-plane effective stiffness (Chatjigeorgiou, et al., 2007)

Mode [-]	$\boldsymbol{\omega_n}$ BC1 [rad/s]	$\boldsymbol{\omega_n}$ BC2 [rad/s]	$\boldsymbol{\omega_n}$ BC3 [rad/s]
1	-	-	-
2	0.096	0.145	0.750
3	0.165	0.214	1.160
4	0.234	0.299	1.711
5	0.298	0.373	2.237
6	0.364	0.456	2.414

Table 4-5 Natural frequencies of the in-plane mode shapes for each base case

The natural frequencies of the bending motions of a simple supported beam with length L can be determined with equation (4.1). A derivation of this equation is presented in Appendix A.

$$\omega_n = \sqrt{\frac{EI}{\rho_s A}}\left(\frac{n\pi}{L}\right)^2 \tag{4.1}$$

The boundary conditions are different for the tensioned nonlinear bent pipeline. Therefore equation (4.1) does not approximate the natural frequencies of the base cases very accurately. Nevertheless some behaviour of equation (4.1) can also be applied on the base cases. For instance a larger bending stiffness and smaller span length results in higher natural frequencies which is also the situation for the base cases (Table 4-5).

For BC1, the mode shapes for the in-plane normal motions and bending moment along the pipeline in the plane of bending (XZ) are plotted in Figure 4-7. The different mode shapes converge in the TDA. Both the dynamic in-plane bending moments and normal motions have peaks in the area before the TDP. Normal motions in the TDA give rise to the in-plane dynamic curvature and which result in larger in-plane bending moments. Note that for an increased number of modes the last peak in the mode shapes before TDP shifts closer to TDP. For BC1, the first few natural frequencies (Table 4-5) are lower than the excitation frequencies of the vessel motions by waves (usually between 0.30 rad/s and 1.25 rad/s). This way, the shifting of the last peaks before TDP will be the result of motions with increasing frequencies and occur in smaller steps. Therefore, the dynamic effects will cause the maximum dynamic bending moments to occur in the same region of pipeline (TDA). A fluctuation of axial motion leads to tension fluctuations which lead to fluctuations of the dynamic bending moment. In the static situation was seen that the axial motions of the pipeline at LOP result into normal motions of the pipeline in the TDA. Because the normal motions of the pipeline correspond to the bending moment, the maximum bending moment during dynamic simulations are likely to occur close or at the maximum static bending moment in the TDA. Note that the two large peaks (first and latest) in the mode shapes for M_{Y} are the supports and not the first and last peaks of the bending moment due to the bending of the pipeline.

For BC2, the modes shapes of the in-plane normal motions and dynamic bending moments along the pipeline are shown Figure 4-8. The smaller water depth (thus smaller span length) and thicker pipeline result in a less slender pipeline which causes higher natural frequencies (Table 4-5). Therefore more dynamic effects are expected in comparison with BC1. For both the normal motions and the bending moments, the mode shapes show almost equal peaks at the beginning and end of the sagbend. This is likely due to the small departure angle which result in both axial and significant normal motions at LOP. This results in the fact that in the area around LOP, the bending moment is significant. Because the static state solution (section 4.2) shows a small difference between the bending moment in the TDA and area around LOP, the dynamic bending moment has a larger influence on the position of the extreme bending moment in this case.

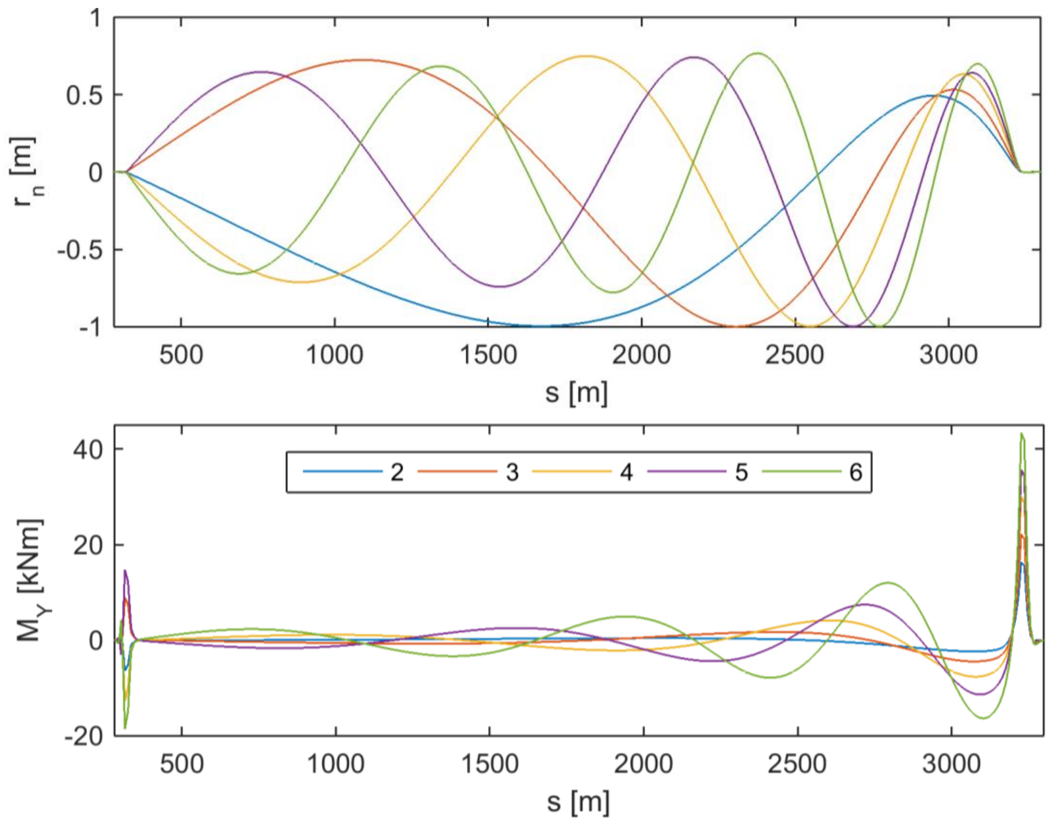

Figure 4-7 First 5 mode shapes for the normal motions along the pipeline (up) and in-plane dynamic bending moment along the pipeline in global Y direction (down) (BC1)

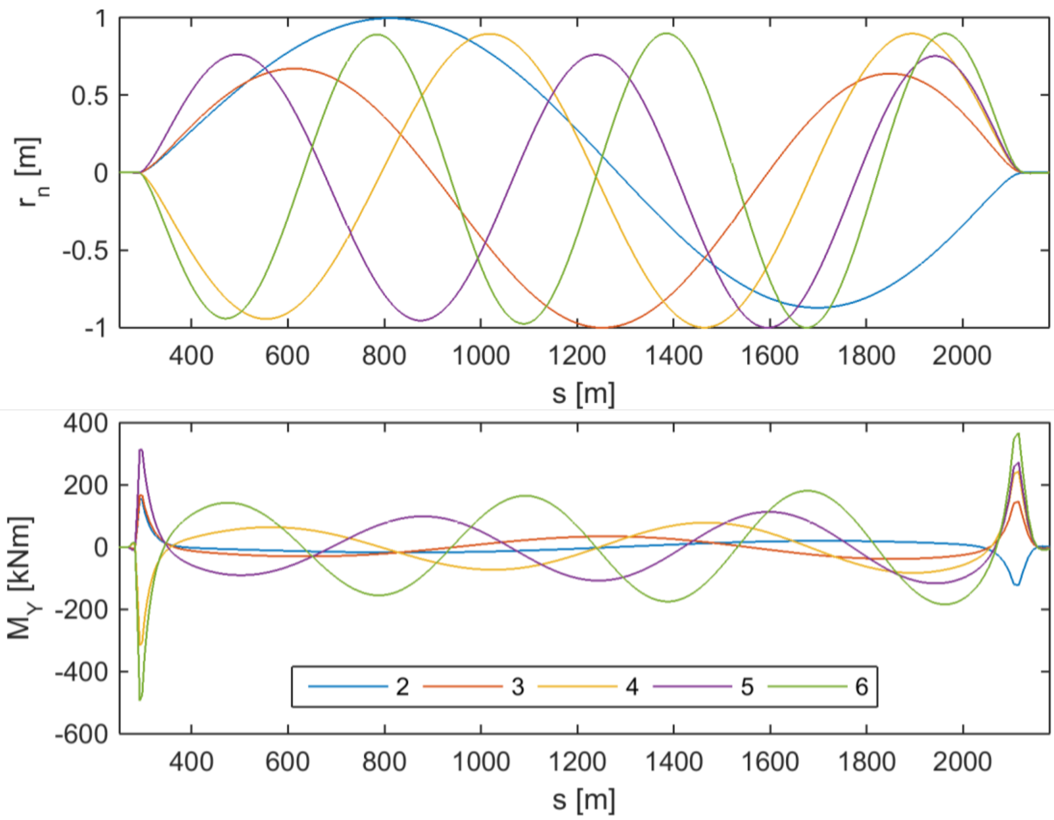

Figure 4-8 First 5 mode shapes for the normal motions along the pipeline (up) and in-plane dynamic bending moment along the pipeline in global Y direction (down) (BC2)

In the situation for BC3, the unsupported pipeline is even less slender and stiffer than in the situation of BC2. Therefore the natural frequencies are even higher. The first two natural frequencies occur within the frequency range of the vessel motions (section 3.1). Note that there is a significant distance between the peaks of the first two mode shapes. Due to resonance at the shifting natural frequencies of the first two modes (BC3), relatively large excited normal motions and dynamic bending moments are expected at different and moving positions along the pipeline. Therefore dynamic behaviour is more present in shallow water cases and pipelines with large bending stiffness's.

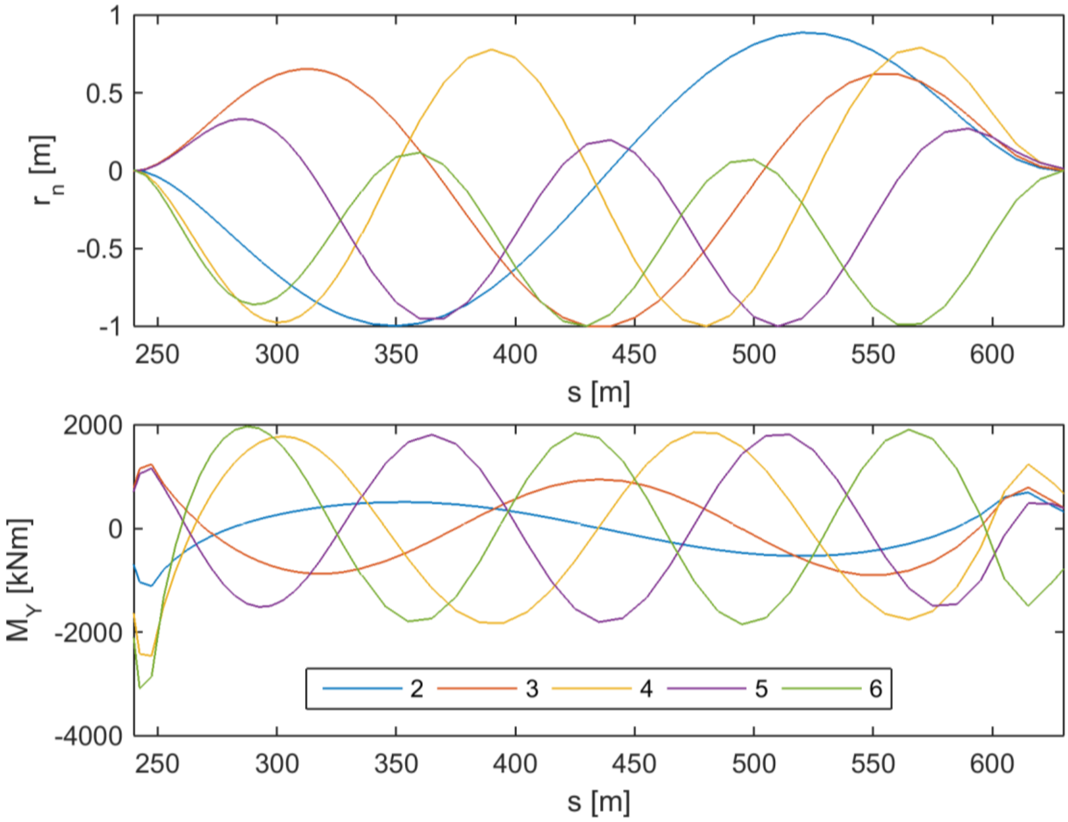

Figure 4-9 First 5 mode shapes for the normal motions along the pipeline (up) and in-plane dynamic bending moment along the pipeline in global Y direction (down) (BC3)

4.4 Chapter Conclusion

Three bases cases are modelled in OrcaFlex with different pipe properties, water depths and departure angles. For the deep water base cases, the maximum static bending moment occurs in the touchdown area (TDA). For a slender pipeline with a departure angle close to 90° also the expected maximum (static + dynamic) bending moment is close to the static bending moment. For stiffer and shorter pipelines with smaller departure angles the natural frequencies of the first mode shapes will increase and occur within the range of common sea states. Therefore more dynamic effects are expected for shallow water cases which result in a relatively large shift of the position of the maximum bending moment in the pipeline.

5.0 DOMINANT VESSEL MOTIONS REGARDING PIPELINE INTEGRITY

In this chapter the dominant vessel motion(s) regarding the total bending moments in the sagbend are derived for the three different base cases defined in previous chapter. Distinction is made between vessel motions at COG and coupling between vessel motions. Simulations are performed using predefined harmonic vessel motions and by using displacement RAOs. With the results of these simulations, the dominant vessel motion regarding pipeline integrity is found.

5.1 Vessel motions at COG

As described in the problem context of section 2.1, MRUs on the vessel are able to measure the actual vessel motions up to all six DOFs. These vessel motions can be superposed to any point in the local vessel coordinate system. First the vessel motion at the COG is considered, because on that point the RAOs are defined in the model.

5.1.1 Vessel motions at COG using predefined harmonic motions

To understand which kind of vessel motions have the most influence at the pipeline integrity, the vessel is excited in different DOF's using different harmonic motions. OrcaFlex has the ability to predefine harmonic vessel motions at the COG without additional excitation by wave kinematics or RAOs. An arbitrary harmonic vessel motion $\xi(t)$ can be modelled as a sinusoidal wave with amplitude ξ_{a}, frequency ω and phase α_{ξ}.

$$\xi(t) = \xi_{\mathrm{a}} \sin\left(\omega t + \alpha_{\xi}\right) \tag{5.1}$$

For each DOF, simulations are performed with a small duration. Each simulation contains one harmonic vessel motion using one DOF, a single frequency ω in the range of $0.3 \leq \omega \leq 1.0$ [rad/s] and a single amplitude ξ_{a}. The common range of amplitudes is sea state (and thus vessel motion) dependent. For instance pitch motions are more likely to response than yaw motions for a typical sea state. However, direct neglecting of some unlikely amplitude beforehand may lead to incorrect conclusions afterwards. Therefore the same range of amplitudes for each DOF is used ($0.5 \leq \xi_{\mathrm{a}} \leq 2$). The units for translational motions are in [m] and rotational motions in [deg].

During a single simulation a vessel motion in one DOF is excited. Motions in other DOFs are constrained. The phase α is discarded, because it is only essential between vessel motions. If one considers a heave motion, the predefined vessel motion in OrcaFlex looks like equation (5.2).

$$\begin{bmatrix} \mathrm{x}^{\mathrm{COG}}(t) \\ \mathrm{y}^{\mathrm{COG}}(t) \\ \mathrm{z}^{\mathrm{COG}}(t) \\ \varphi(t) \\ \theta(t) \\ \psi(t) \end{bmatrix} = \begin{bmatrix} 0 \\ 0 \\ \mathrm{z}_{\mathrm{a}}^{\mathrm{COG}} \sin(\omega t) \\ 0 \\ 0 \\ 0 \end{bmatrix} \tag{5.2}$$

With $\mathrm{x}^{\mathrm{COG}}(t)$ = surge, $\mathrm{y}^{\mathrm{COG}}(t)$ = sway, $z^{\mathrm{COG}}(t)$ = heave, $\varphi(t)$ = roll, $\theta(t)$ = pitch and $\psi(t)$ = yaw.

In total 60 simulations per DOF are performed using 15 frequencies and 4 amplitudes. For each simulation, the maximum bending moment in the sagbend is determined. In contour-plots the maximum bending moment of combined amplitudes and frequencies for each DOF is displayed. For BC1, the contour plots are shown in Figure 5-1 (translational vessel motions) and Figure 5-2 (rotational vessel motions). For vessel motions in all DOFs, the maximum bending moment in the sagbend will increase for increasing frequencies and amplitudes. Of the translational vessel motions, surge and in particular sway have limited influence on the bending moment. A reason why horizontal vessel motions parallel to the sea surface (surge and sway) have limited influence is because of the water depth.

The relation between water depth and uncoupled vessel motions concerning sagbend moments during S-mode pipelay has been investigated a long time ago (Brewer & Dixon, 1970). Their conclusion was that at a deep water depths (>100m), the unsupported pipeline becomes heavier and pitch motions are dominant regarding bending stress. Therefore concerning bending stress, pitch can be linearly related to water depth. In intermediate water depths (between 30m and 100m), surge and heave motions are dominant regarding bending stress.

In case of BC1 the long slender pipeline leaves the stinger in a direction almost perpendicular to the sea surface level (section 4.2). During the excitations, heave and pitch motions have significant influence on the sagbend bending behaviour in deep water. These in-plane vessel motions cause large axial tension variations of the pipeline and thus the highest dynamic bending behaviour. In the contour plot for heave one notices linear behaviour for increasing amplitude and for increasing frequency. For small pitch motions the same kind of response is seen. In fact pitch and heave show the same response, but for different quantities. This give rise to the theory to combine or couple pitch and heave motions. Roll and yaw motions also have influence on the pipeline's response behaviour, but only for large excitations.

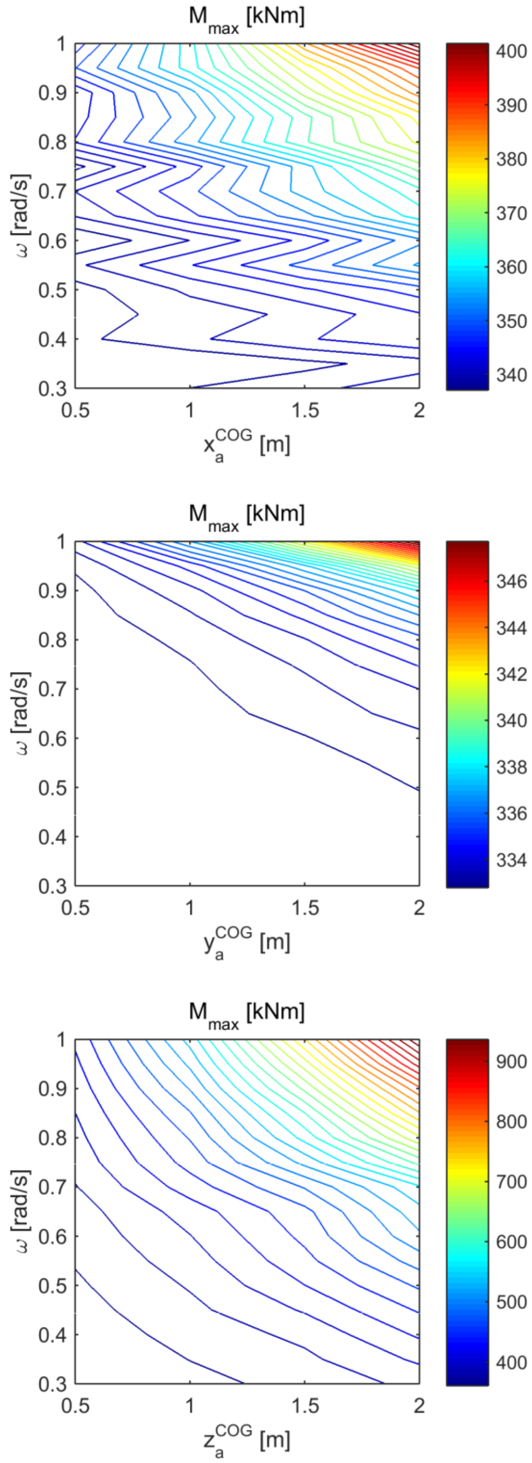

Figure 5-1 Translational vessel motions in COG: Surge, Sway and Heave (BC1)

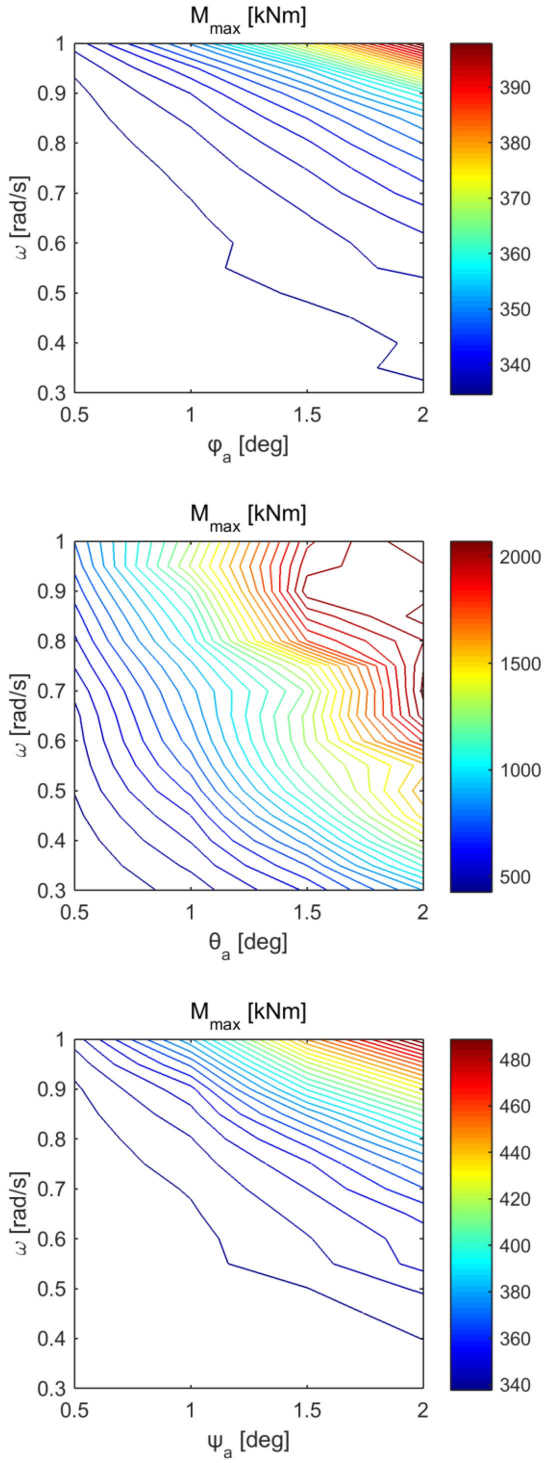

Figure 5-2 Rotational vessel motions: Roll, Pitch and Yaw (BC1)

The contour plots of BC2 are presented in Figure 5-3 and Figure 5-4. One notices a different kind of motion behaviour. In addition to heave, the horizontal vessel motions (surge and sway) also result into large bending moments in the sagbend. Furthermore the shape of the contour plot of surge and heave look similar to the one of surge of BC1 (Figure 5-1). The horizontal vessel motions also induce axial tension fluctuations which cause bending moment fluctuations. The shape could be an aspect of the normal motions and thus an aspect of the hydrodynamic loads. Another interesting aspect is that sway motions only amplify the bending moments for high frequencies and large amplitudes. This is different behaviour than for surge and heave motions where the influence on the bending moments is more evenly amplified (more linear). This is because there is no out-of-plane bending moment during the static situations. For increasing sway excitations, the out-of-plane bending moment is increased. Until the static in-plane bending moment is larger than the dynamic out-of-plane equivalent, it is not noticeable in the contour plot for the total maximum bending moment. Keeping this in mind, still some in-plane bending moments are increased by an out-of-plane motion like sway. These amplified in-plane bending moments could be the result of nonlinear behaviour (Chatjigeorgiou & Mavrakos, 2009). This phenomenon will be treated in more detail in section 6.2.4. Regarding the rotational motions, yaw is in addition to pitch of major influence at the maximum bending moments in the sagbend. Both rotations amplify the axial motions of the pipeline. Roll has in particular influence at the smaller out-of-plane bending moments.

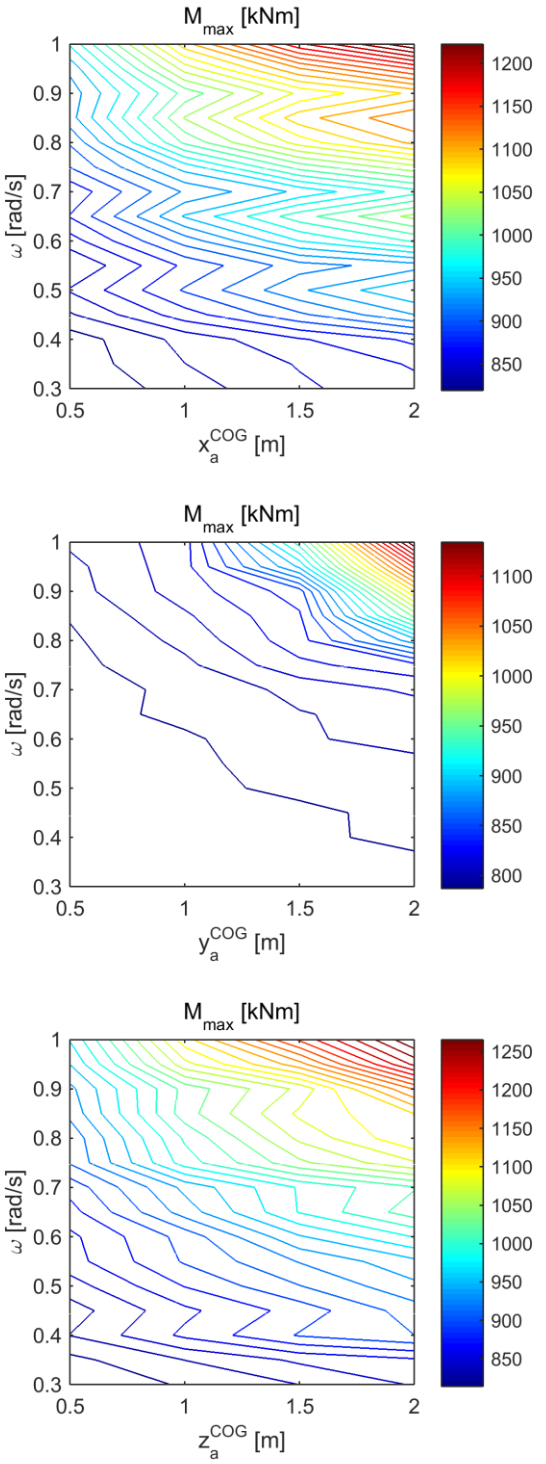

Figure 5-3 Translational vessel motions in COG: Surge, Sway and Heave (BC2)

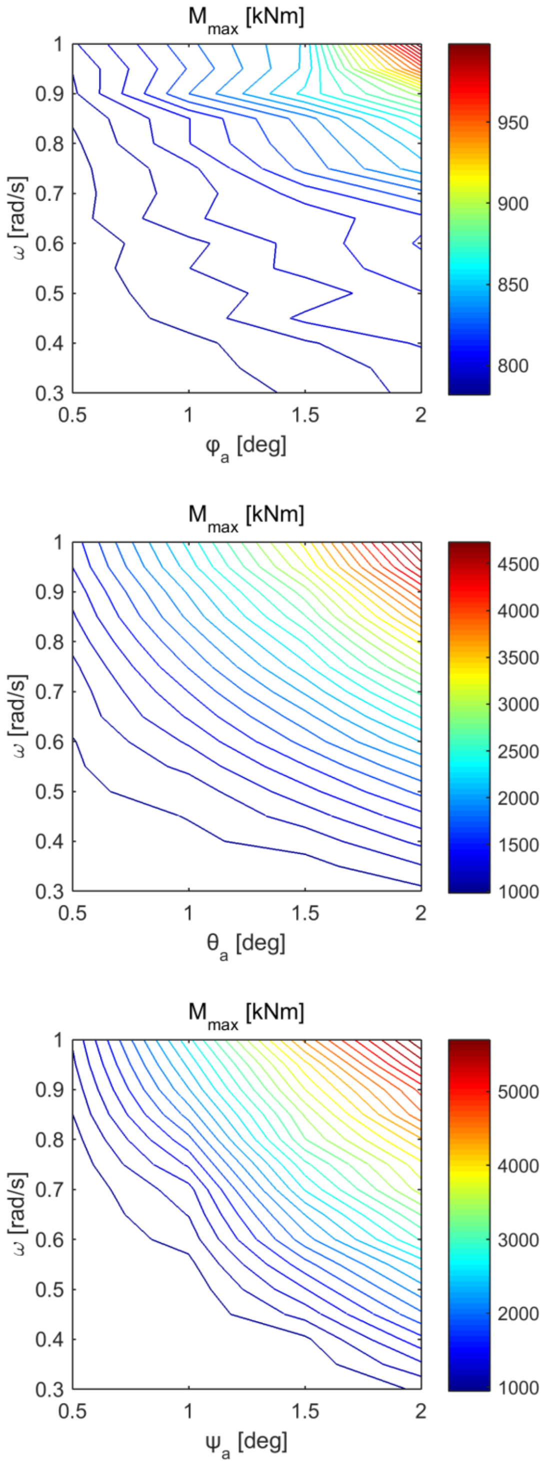

Figure 5-4 Rotational vessel motions: Roll, Pitch and Yaw (BC2)

At shallow water depths like BC3 (which is roughly the situation of BC2 with a water depth of 92m below sea level), the vessel motions amplify the total bending moment significantly. Pitch and yaw still have the largest influence on the pipeline integrity, but relatively speaking the influence of pitch is less compared to BC2. Other motions like heave and surge have more influence now on the shorter unsupported pipeline (Brewer & Dixon, 1970). Also the out-of-plane motions have more influence. Both facts give rise to the thought that vessel motion based criteria for pipelay operations in shallow water is more difficult to achieve, because all six DOFs have significant influence on the bending moment in the sagbend. Note the in-plane resonance at a frequency of about 0.80 rad/s (surge/heave) and out-of-plane resonance at 0.85 rad/s (sway). This phenomenon was also concluded during the modal analysis in 4.3.

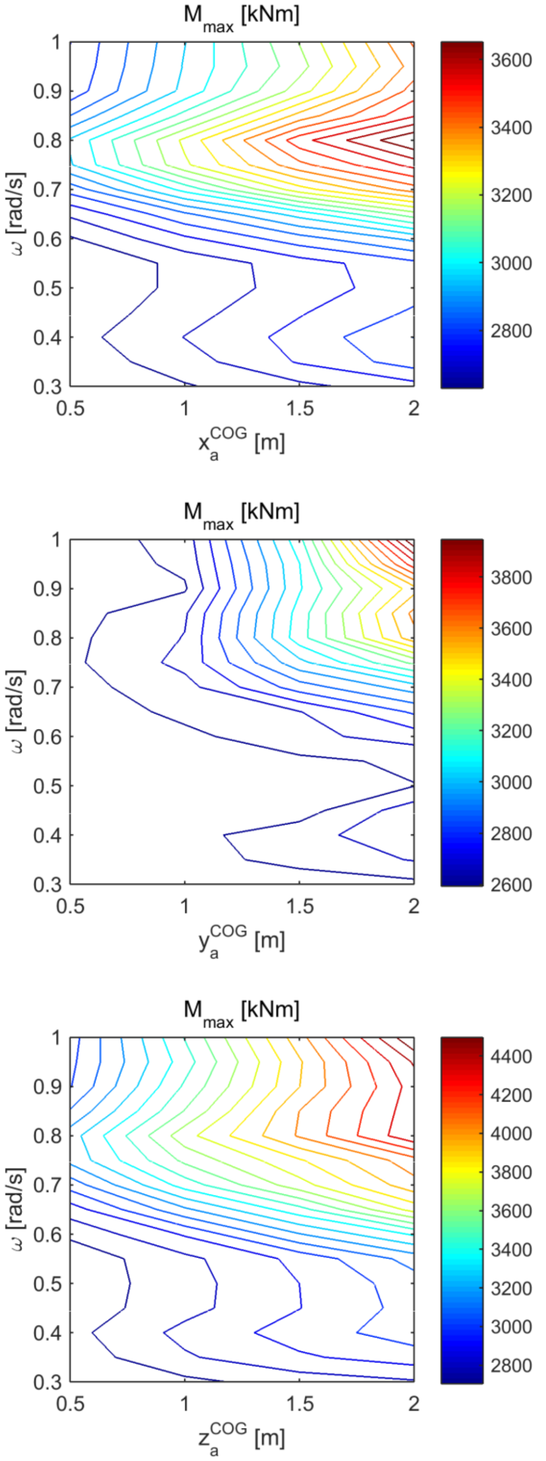

Figure 5-5 Translational vessel motions in COG: Surge, Sway and Heave (BC3)

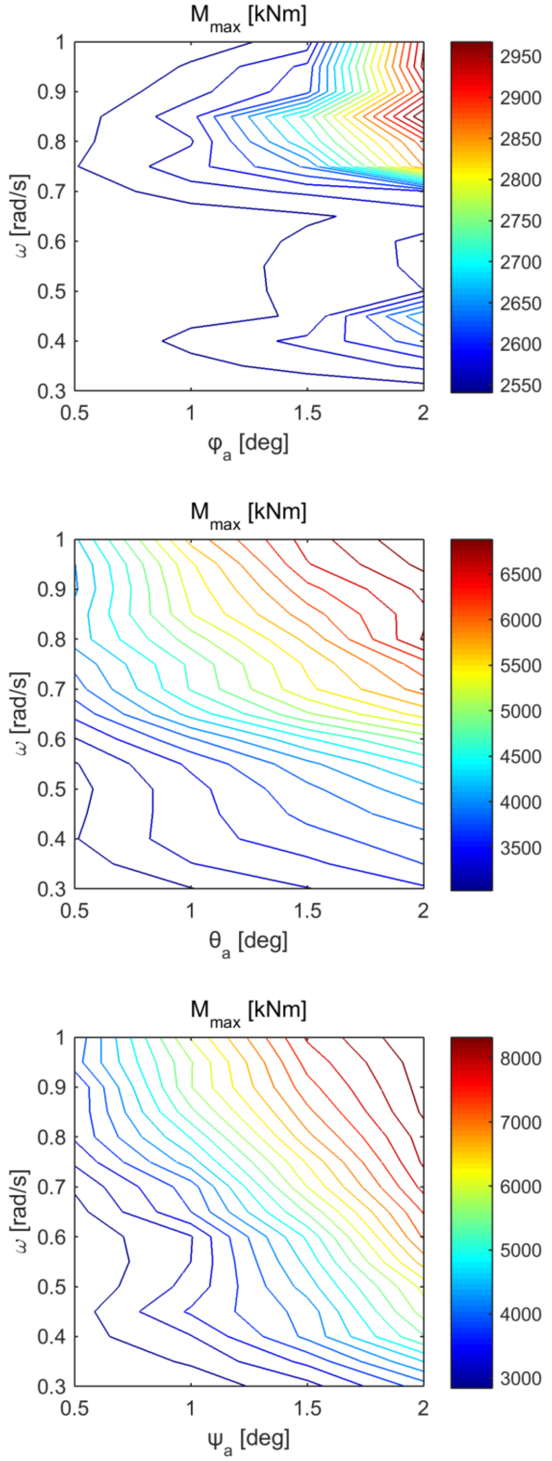

Figure 5-6 Rotational vessel motions: Roll, Pitch and Yaw (BC3)

5.1.2 Vessel motions at COG using displacement RAOs

In the previous section, a single range of amplitudes for all DOFs was used. In reality each combination of frequency and amplitude of the DOFs has a certain probability. In 3.1 is described that using wave spectra, linear theory and displacement RAOs, a sea state can be transferred into vessel motions over time. In this section simulations are performed with a critical sea state using a JONSWAP spectrum with a $\mathrm{H_S}$ of 4m and a $\mathrm{T_Z}$ of 9s. By assuming that the vessel is symmetric along its longitudinal axis (section 3.1), only wave directions between 0° (stern/stinger) and 180° (bow) are considered. The range is divided into steps of 10°, which means a total of 19 simulations are needed. A duration of 900s is used. Because a variance density spectrum is a stochastic representation of the irregular sea surface (section 1.2) the significant amplitude of the response ξ_s is more interesting than the maximum amplitude $\xi_{\max}$ in each DOF. The significant amplitude of the vessel motions in each direction are presented in polar plots for translational and rotational vessel motions in respectively Figure 5-7 and Figure 5-8.

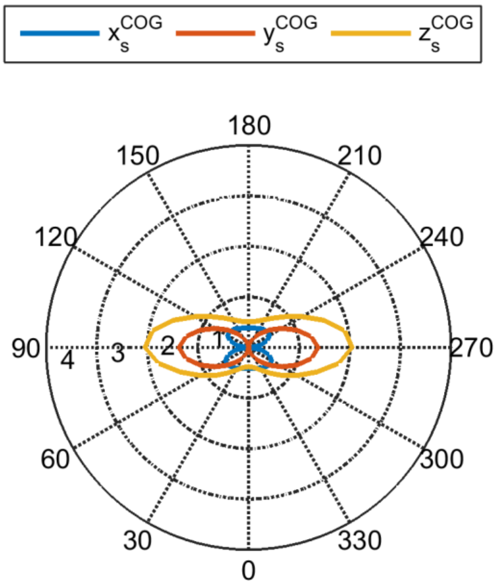

Figure 5-7 significant amplitude of surge, sway and heave. JONSWAP spectrum, $\mathrm{H_S} = 4.0m$, $\mathrm{T_Z} = 9.0s$, $t_{\mathrm{sim}} = 900s$. (BC1/BC2/BC3)

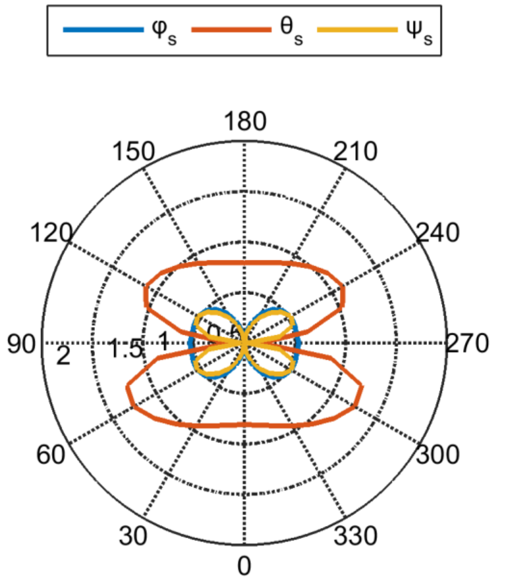

Figure 5-8 significant amplitude of roll, pitch and yaw. JONSWAP spectrum, $\mathrm{H_S} = 4.0m$, $\mathrm{T_Z} = 9.0s$, $t_{\mathrm{sim}} = 900s$. (BC1/BC2/BC3)

As one notices in the figures, large pitch motions are likely to occur in quartering, head and stern waves. More importantly the significant amplitude of pitch is much larger than the significant amplitudes of the other rotational motions. In other words, pitch motions are more likely to occur in heavy sea states than roll and yaw. Instead of the polar plot above one also could investigate the displacement RAOs of the vessel to see that large pitch motions are likely to occur more often than roll and yaw motions. However for beam waves approaching perpendicular to the vessel, pitch motions are very limited. Roll, heave and sway motions are largest in this direction. In comparison with the contour plots of Figure 5-1 and Figure 5-2 the magnitude the heave and roll motions of have more influence on the bending moment than sway motions.

By using linear theory, the vessel motions are Gaussian distributed (section **Error! Reference source not found.**). In section 3.5.3 was described that the dynamic equilibrium shows nonlinear behaviour. Therefore it makes no sense to use significant amplitudes for dynamic bending moment. Instead the maximum total bending moment per direction is shown all three base cases in Figure 5-9 to Figure 5-11. For all three base cases the overall maximum bending moment occurs for beam quartering waves at an approach angle of 70°. The extreme bending moments coincidence with the largest significant rotational vessel motions. However the significant amplitude of pitch in combination with the contour plots of Figure 5-2 and Figure 5-4 validate that the pitch motion is dominant in this direction. By comparing the shape of the pitch motion in Figure 5-8 with the shape of the maximum bending moment in Figure 5-9 and Figure 5-10, one notice similarities for other directions as well. Only the responses for pure beam waves approaching the vessel from 90° are different. Heave and roll instead of pitch motions have the most influence on the total bending moment in this direction. In the situation of BC3 (Figure 5-11), vessel motions in other DOFs like surge and yaw also affect the maximum bending moment which is seen in Figure 5-5 and Figure 5-6. Although pitch is dominant in BC3 for beam quartering waves, the vessel motions in other DOFs should not be underestimated.

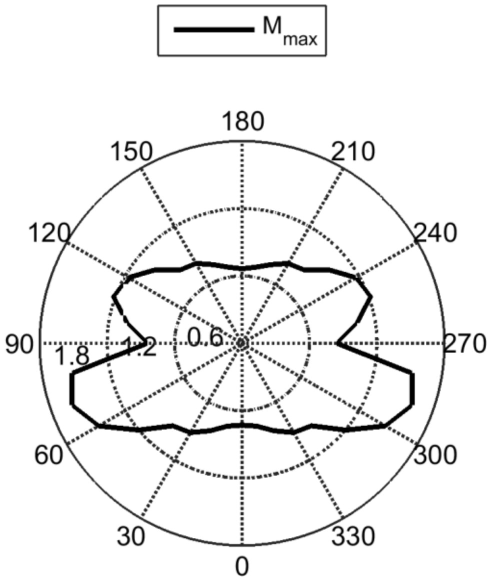

Figure 5-9 The maximum total bending moment per direction [MN]. JONSWAP spectrum, $\mathrm{H_S} = 4.0m$, $\mathrm{T_Z} = 9.0s$, $t_{\mathrm{sim}} = 900s$. (BC1)

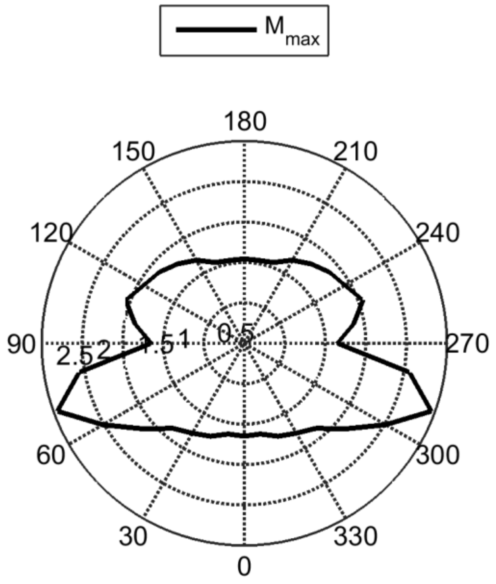

Figure 5-10 The maximum total bending moment per direction [MN]. JONSWAP spectrum, $\mathrm{H_S} = 4.0m$, $\mathrm{T_Z} = 9.0s$, $t_{\mathrm{sim}} = 900s$. (BC2)

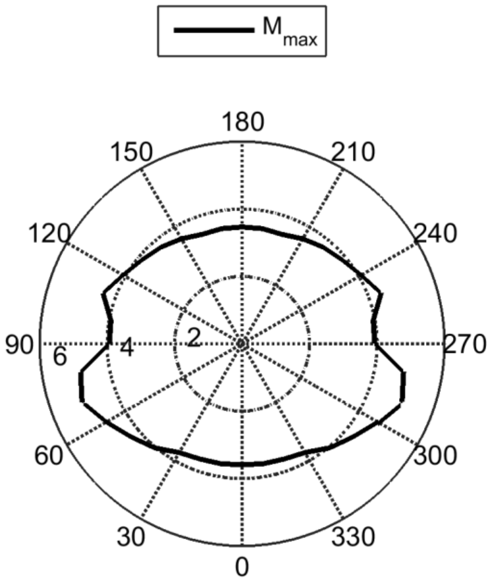

Figure 5-11 The maximum total bending moment per direction [MN]. JONSWAP spectrum, $\mathrm{H_S} = 4.0m$, $\mathrm{T_Z} = 9.0s$, $t_{\mathrm{sim}} = 900s$. (BC3)

5.2 Superposed vessel motions

Despite knowing the dominant vessel motions at COG regarding bending moment, the less dominant vessel motions still have significant influence on the bending moments in the sagbend. Furthermore for beam approaching waves, heave motions are dominant instead of pitch motions. As described in section 5.1.1, coupling of pitch and heave motions could be beneficial. In this section the vessel motions which work in COG are superposed to a point on the vessel which will improve the relationship between dominant vessel motions and bending moment.

5.2.1 Superposition of vessel motions

Vessel motions can be superposed at every location relative to COG. For the pipeline integrity the axial motions of the pipeline are directly responsible. In general, larger axial motions of the pipeline results in larger bending moments. This is the main reason why tensioners are compensating these motions. Ideally one wants a fixed location for which the axial motions of the unsupported pipeline are equal to the vessel motions. Unfortunately, LOP where the pipeline departures from the stinger is not a fixed location, but is shifting over the stinger. Dynamic tension will cause LOP to fluctuate upwards and downwards on the stinger. For large vessel motions, the dynamic effective tension results into loads on the stinger tip which can cause buckling. For extreme bending moments and thus low effective tension, the stinger tip (ST) location is close to the inflection point. Assumed is that the difference in pipeline motions between the stinger tip location, LOP and inflection point is very small. Hence the stinger tip location is used for coupling the vessel motions.

To find the vessel motions on the stinger tip, the principle of superposition is used (Journeé and Massie, 2000). For each DOF, the coupled vessel motions at the stinger tip location relative to the COG can be derived using this principle. However before using it the lay system must satisfy the following two conditions:

- First of all, the vessel and stinger need to be considered as one system with the stinger rigidly connected to the vessel. For large stingers such as the one from Solitaire which is used in this research, the direct hydrodynamic load has small effects on the stinger itself (Marbus, 2007). However these loads can be considered small and are therefore neglected in this thesis.

- Another condition is that the angles of rotation (θ, φ and ψ which are expressed in radians) need to be small ($\sin\varphi \approx \varphi$). Also this condition is assumed to be satisfied, because in beam waves roll motions higher than 0.1 rad can occur and thus some nonlinearity applies.

For convenient use of the principle of superposition, the trigonometric functions are expressed in the complex notation using Euler's formula. An arbitrary harmonic vessel motion which is dependent on time and frequency can be written using the following function:

$$\xi(t) = \hat{\xi}_{\mathrm{a}}\, e^{i(\omega t+\alpha)} \tag{5.3}$$

Where ξ_{a} denotes the complex amplitude of the harmonic vessel motion (in [m] or [rad]):

$$\hat{\xi}_{\mathrm{a}} = \mathrm{Re}(\xi_{\mathrm{a}}) + i\,\mathrm{Im}(\xi_{\mathrm{a}}) \tag{5.4}$$

and α the phase shift [-]:

$$\alpha = \arctan\left(\frac{\mathrm{Im}(\xi_{\mathrm{a}})}{\mathrm{Re}(\xi_{\mathrm{a}})}\right) \tag{5.5}$$

If $\alpha < 0$, a value of π is added to correct the domain of the phase shift α.

Next, equation (5.6) will superpose the motions on any point projected point P on the vessel (Journee and Massie, 2000). In this case P is the stinger tip location (ST).

$$\begin{bmatrix} x_P(t) \\ y_P(t) \\ z_P(t) \\ \theta_P(t) \\ \varphi_P(t) \\ \psi_P(t) \end{bmatrix} = \begin{bmatrix} 1 & 0 & 0 & 0 & z_{dP} & -y_{dP} \\ 0 & 1 & 0 & -z_{dP} & 0 & x_{dP} \\ 0 & 0 & 1 & y_{dP} & -x_{dP} & 0 \\ 0 & 0 & 0 & 1 & 0 & 0 \\ 0 & 0 & 0 & 0 & 1 & 0 \\ 0 & 0 & 0 & 0 & 0 & 1 \end{bmatrix} \cdot \begin{bmatrix} x^{COG}(t) \\ y^{COG}(t) \\ z^{COG}(t) \\ \theta(t) \\ \varphi(t) \\ \psi(t) \end{bmatrix} \tag{5.6}$$

Where x_{dP}, y_{dP} and z_{dP} are the distances in [m] between the local x, y and z coordinates of the stinger tip location and the COG. See Figure 5-12. The tangent of the pitch angle times x_{dP} result in z_{dP}. Thus for pitch motions, this will result into large coupled vertical and in-plane horizontal motions at the stinger tip location. In the static state situation, the roll and yaw angle does not influence the coupled motions of the stinger tip, because $y_{dP} = 0$. The triangles for roll and yaw in Figure 5-12 are fictitious to resemble which motions are induced on the stinger tip. Roll and yaw motions will result into in-plane and out-of-plane horizontal stinger tip motions.

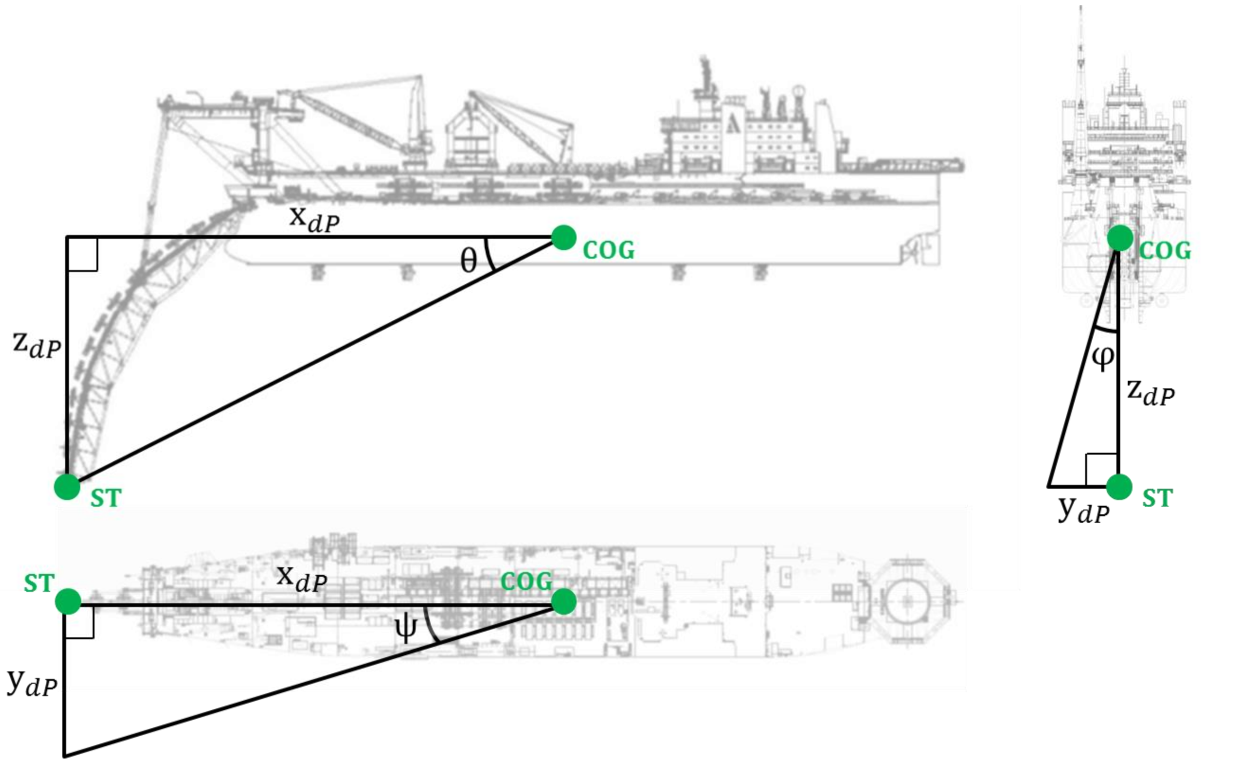

Figure 5-12 Relation between uncoupled vessel motions and coupled vessel motions at the stinger tip. Influence of pitch (top left), roll (right) and yaw (bottom).

In addition of using the principle of superposition on vessel motions, the principle could also be applied for displacement RAOs which are in fact also vessel motions for a unit wave height. For 19 directions between 0° and 180°, the RAOs at COG are superposed to RAOs which relate the waves at COG to vessel motions at the stinger tip location.

5.2.2 Superposed vessel motions using displacement RAOs

Using the new RAOs of the coupled vessel motions at the stinger tip new simulations are performed in the 19 directions. The same sea state as in section 5.1.2 is used. The significant amplitude of the stinger tip motions per direction are shown in Figure 5-13 and Figure 5-14. One notices that the vertical stinger tip motions are significant in all directions for both cases. The shape of the vertical stinger tip motions in the polar plot is similar to the shape of the pitch motions in COG (Figure 5-8). This is because particularly pitch motions result in vertical stinger tip motions which is seen in equation (5.6). The ratio between vertical and in-plane horizontal stinger tip motions is larger for BC2 and BC3 in comparison with BC1. This is due to the different stinger setting of BC2/BC3 which results into a large distance between the stinger tip and COG. In section 5.1.1 is described that for BC2, the horizontal motions have much more influence on the bending moment. In the situation of BC1, the out-of-plane horizontal motions occur less than in the situation of BC2/BC3. Also this results from the different stinger setting which superpose yaw motions into out-of-plane horizontal motions.

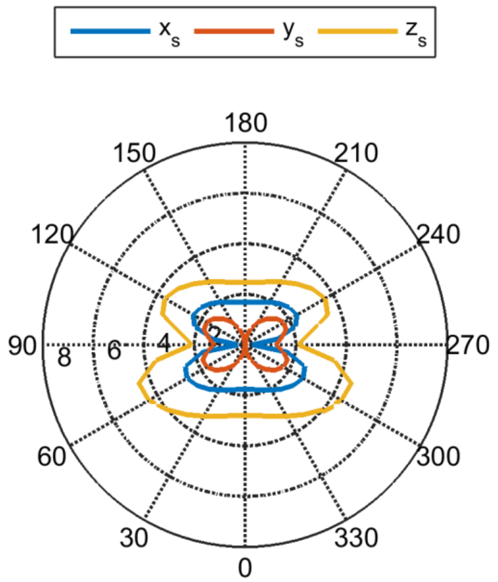

Figure 5-13 significant amplitude of the stinger tip motions in the global X, Y and Z direction. JONSWAP spectrum, $\mathrm{H_s} = 4.0m$, $\mathrm{T_z} = 9.0s$, $t_{\mathrm{sim}} = 900s$. (BC1)

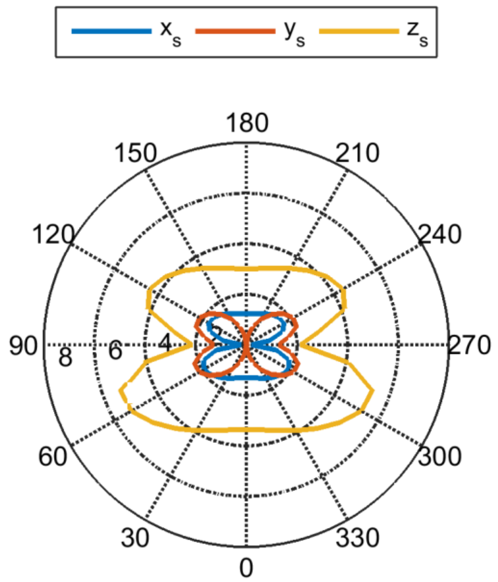

Figure 5-14 significant amplitude of the stinger tip motions in the global X, Y and Z direction. JONSWAP spectrum, $\mathrm{H_s} = 4.0m$, $\mathrm{T_z} = 9.0s$, $t_{\mathrm{sim}} = 900s$ (BC2/BC3)

In Figure 5-13 and Figure 5-14, the maximum vertical stinger tip motions as well as the shape of the maximum bending moment (of Figure 5-9 and Figure 5-10) of the simulations are shown. The shapes of both quantities show some similarities. They both vary their magnitudes in about the same ratio along the different directions.

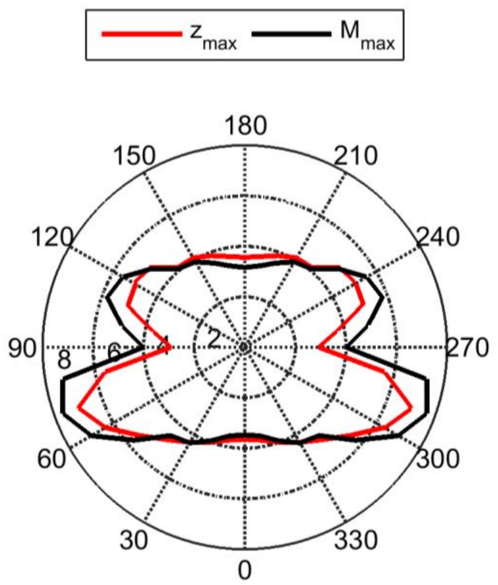

Figure 5-15 maximum vertical stinger tip and maximum total bending moment. JONSWAP spectrum, $\mathrm{H_s} = 4.0m$, $\mathrm{T_z} = 9.0s$ $t_{\mathrm{sim}} = 900s$ (BC1)

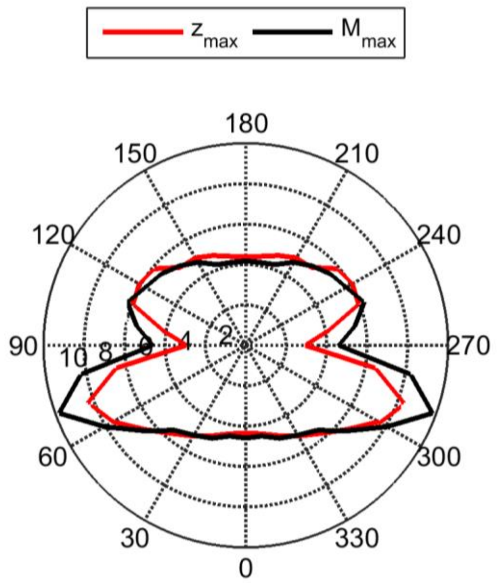

Figure 5-16 maximum vertical stinger tip and maximum total bending moment. JONSWAP spectrum, $\mathrm{H_s} = 4.0m$, $\mathrm{T_z} = 9.0s$ $t_{\mathrm{sim}} = 900s$ (BC2)

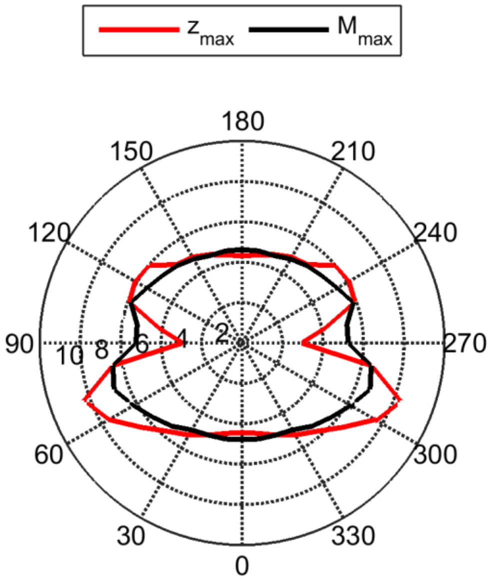

Figure 5-17 maximum vertical stinger tip and maximum total bending moment. JONSWAP spectrum, $\mathrm{H_s} = 4.0m$, $\mathrm{T_z} = 9.0s$, $t_{\mathrm{sim}} = 900$ (BC3)

In the situation of BC3 (Figure 5-17), the shape of the maximum vertical stinger tip motions is different in comparison with the shape of the maximum sagbend bending moment. This is because the horizontal stinger tip motions also affect the bending moment in the pipeline. In beam waves the out-of-plane horizontal stinger tip motions affect the bending moment in the sagbend.

5.3 Chapter conclusion

In deep water, pitch motions are the dominant uncoupled vessel motions with regards to the total bending moment in the sagbend. In beam waves, heave and roll motions instead of pitch motions are dominant according to the analyses. In reality there is always some wave directional spreading of ocean waves involved, which reduce the pitch motions of the worst angle and spread them over the beam direction. Thus pitch motions are dominant for beam waves with wave directional spreading.

The dominant pitch, heave and roll motions can be superposed to the stinger tip location which cause large vertical motions of the stinger tip. These vertical stinger tip motions have the largest influence on the bending moment in the sagbend.

By reducing water depth or stinger radius, other motions like surge and yaw get more influence on the bending moment in the sagbend. These vessel motions increase the effect of the in-plane horizontal stinger tip motions at the bending moment in the sagbend. For a deep water case like BC2 this effect is small, but for shallow water (BC3) the effect should not be underestimated. In shallow water also the out-of-plane sway motions have increased influence for larger amplitudes and frequencies. Therefore in shallow water other DOFs like sway and yaw also influence the total bending moment in the sagbend.

6.0 VESSEL MOTION BASED CRITERIA

In the previous chapter is concluded that the dominant vessel motion which increases the bending moments in the sagbend is the vertical motion of the stinger tip which is superposed from heave, pitch and roll. In this chapter vessel motion based criteria based on vertical stinger tip motions is derived and validated for the base cases described in chapter 4.2.

6.1 Relation between vertical stinger tip motions and effective tension

Vessel motions cause compressive axial motions in the pipeline which result in compressive axial tension and thus higher bending moments. In previous chapter was described that for a deep water static configuration (BC1) mainly vertical motions at the stinger tip are related to bending moments in the sagbend.

To assume that the axial motions in the pipeline are directly related to only the vertical motions of the stinger tip, one must ensure the pipeline leaves the stinger almost perpendicular to the seabed. This way also the axial tension of the pipeline can be related to the vertical stinger tip motions. Because the effective tension and the bending moment are also related, one may obtain vessel motion based pipe lay criteria.

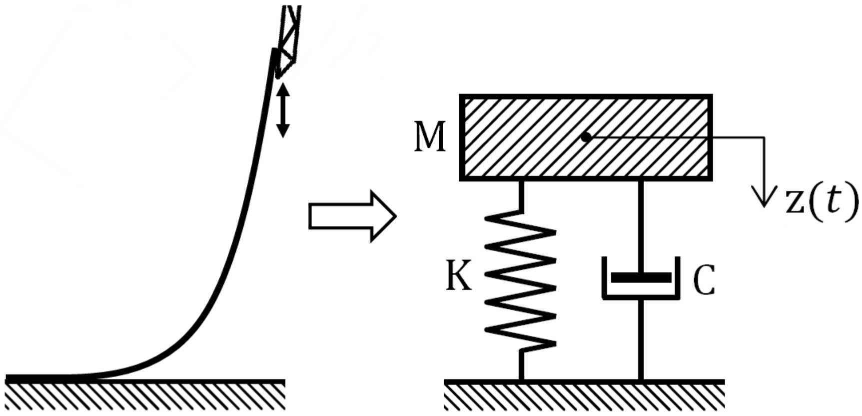

Figure 6-1 spring dashpot representation of dynamic tension at the stinger tip location

The total effective tension $T(t)$ in the pipeline can be described as a mass-spring-dashpot system (Figure 6-1) in a similar way as in section 3.4. The total effective tension

$$T(t) = \mathrm{M}\ddot{\mathrm{z}}(t) + \mathrm{C}\dot{\mathrm{z}}(t) + \mathrm{Kz}(t) + T_{\mathrm{sta}} \tag{6.1}$$

With M the mass coefficient [kg], $\mathrm{C}(t)$ the damping coefficient [kg/s], K the spring coefficient [kg/s^2], $\mathrm{z}(t)$ the vertical stinger tip motions [m] and T_{sta} the static effective tension [kN]. The coefficients of stiffness and mass are assumed equal to respectively equation (3.37) and (3.39). The damping coefficient is assumed equal to the equivalent damping coefficient c_{eq} derived in equation (3.53).

6.1.1 Relation between vertical stinger tip motions and effective bottom tension without probability

In section 4.3 is described that the axial motions of the pipeline at LOP result in normal motions at the seabed. Because the mass coefficient M is only dependent on the vertical motions (section 3.4.), the inertia term can be neglected at TDP in case of BC1 where axial pipe motions on LOP are related to vertical stinger tip motions. Also the stiffness at TDP is no longer dependent of only the vertical displacement, but the total displacement due to influences by weight, length and departure angle. This means that the spring stiffness in relation with vertical stinger tip motions is unknown. Assumed is that the spring stiffness is small. Since fluid drag is related to the normal velocity of the pipeline squared, the damping term governs the dynamic tension at TDP. Therefore the total effective tension at TDP is assumed to be

$$T_{\mathrm{TDP}}(t) \approx \mathrm{C}_{\mathrm{TDP}}\,\dot{\mathrm{z}}(t) + T_{\mathrm{TDP;sta}} \tag{6.2}$$

Because of the relation between fluid drag and quadratic velocity, the relation between vertical stinger tip velocity and effective bottom tension is therefore most probably close to a quadratic relation.

To test this relation, short simulations with the wide variety of theoretic vertical stinger tip motions (different frequency and amplitude) of 5.1.1 are used. For each simulation the minimum effective tension at TDP is compared with the vertical stinger tip velocity. Their relation is plotted in Figure 6-2. The coloured lines represent the different amplitudes of the vertical stinger tip motions (between 0.5 m and 5 m in steps of 0.5 m). The points along the lines represent the different frequencies (between 0.30 and 1.00 rad/s in steps of 0.05 rad/s). An increase in vertical stinger tip velocity results in more compression at TDP. For frequencies of 0.70 rad/s and above, the vertical stinger tip velocity induces larger axial motions in the pipeline which result in more effective bottom tension. For a certain amplitude and frequency combination (for example 3 m and 0.95 rad/s), the relation between the vertical stinger tip velocity and effective bottom tension shows significant nonlinear behaviour. It must be noted that these kinds of stinger tip motions are unlikely to happen.

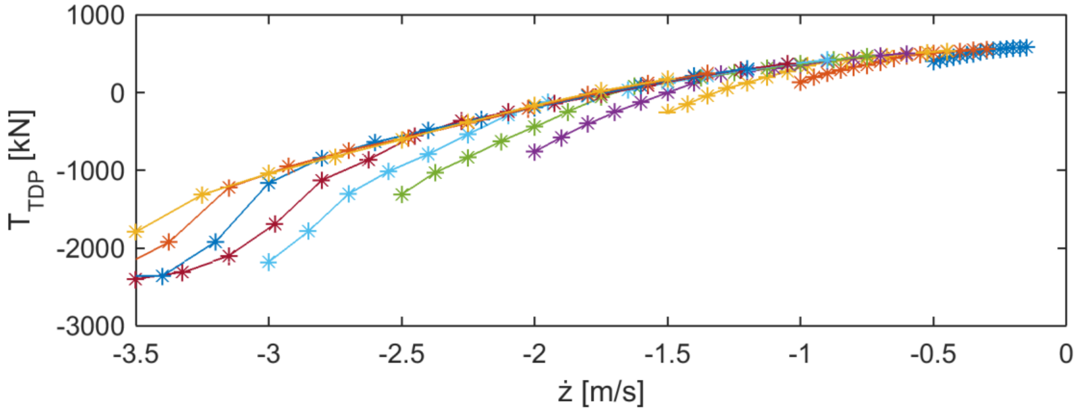

Figure 6-2 Relation between vertical stinger tip velocity and effective bottom tension using 150 short simulations containing vertical stinger tip excitations with different frequencies and amplitudes (BC1)

The contour plot of Figure 6-3 presents the minimal vertical velocity in the pipeline for a vertical stinger tip excitation. Notice that the contour plot shows similar behaviour as the contour plot of the heave motions in Figure 5-1 of previous chapter. The coupling of pitch and heave which headed to vertical stinger tip velocities show thus the same kind of linear behaviour as for heave motions. The contour plot in Figure 6-4 presents the effective bottom tension for a vertical stinger tip excitation. Comparison between the contour plots below shows similar behaviour as the plot in Figure 6-2.

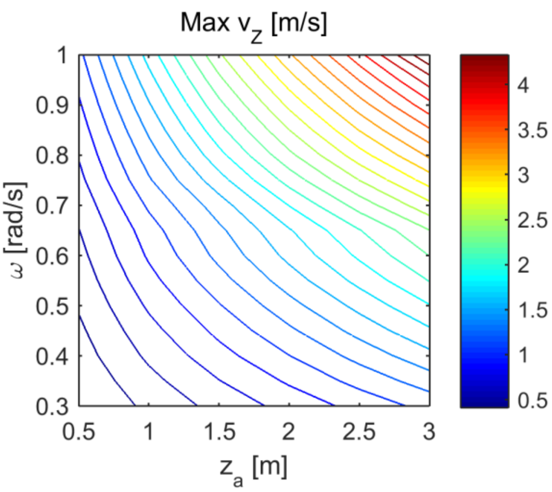

Figure 6-3 Relation between vertical stinger excitation and the vertical velocity in the pipeline

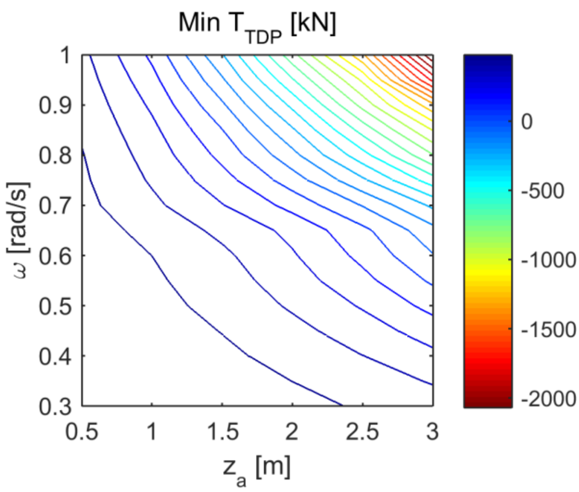

Figure 6-4 Relation between vertical stinger excitation and the effective bottom tension

Instead of theoretic harmonic motions, also motions excited by stochastic irregular seastates are used to show the relation between vertical stinger tip velocity and effective bottom tension. The main advantage is that the relation is more practical, because with the probability into account it better matches the sea conditions. On the other hand the relation of Figure 6-2 can work in combination with all possible sea states. So both relations are of interest.

6.1.2 Relation between vertical stinger tip motions and effective bottom tension with probability

To perform the method using sea states a program is written in MATLAB which is based on a method used in a similar kind of research about dynamic behaviour of steel catenary risers (Passano & Larsen, 2006). The program receives the time histories for two different quantities out of an OrcaFlex simulation. The peaks of the first quantity are linked with the nearest peaks of the second quantity. Together they form paired peaks. In Figure 6-5 can been seen that the vertical stinger tip velocity is correlated with the effective bottom tension. Only the downward peaks are linked, because these peaks affect the bending moments as less tension result into more bending moment (section 3.2.5). In Figure 6-6 one notices that a single peak does not perfectly align on the same time step. This delay is peak dependent which means that not all peaks can be shifted at once. If the peaks occur two much out of sync, they will not be taken into account in order to ensure that not the wrong peaks are compared with each other. This happens in about 1% of the peaks and these peaks are always limited in magnitude. The bandwidth used is about 1.5 s which is smaller than half of the shortest occurring wave period (3.8 s). In conclusion, each peak of one quantity is forming a paired peak with the peak of another quantity except if the peak is outside the bandwidth.

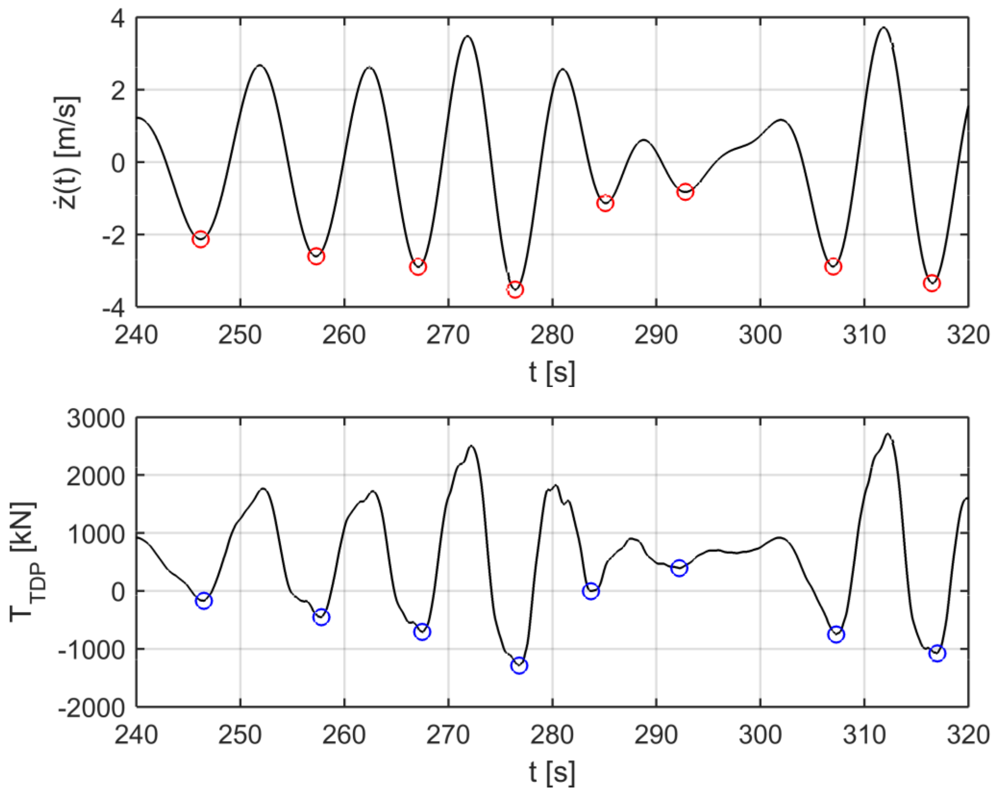

Figure 6-5 Time history of vertical stinger tip velocity (up) and effective bottom tension (down) (BC1)

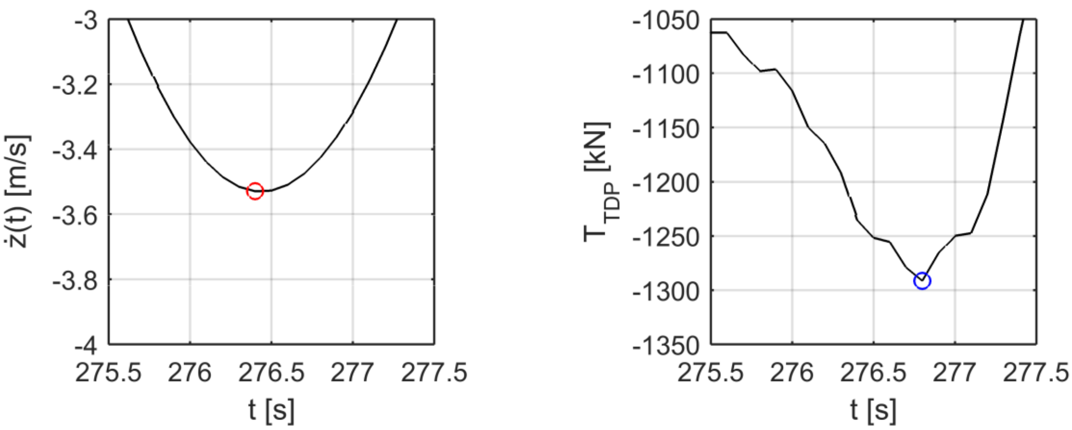

Figure 6-6 Misalignment of a downward peak between different quantities (BC1)

After compiling the paired peaks, scatter diagram are developed. The paired downward peaks between negative stinger tip velocity and effective bottom tension using different simulations are plotted in Figure 6-7 till Figure 6-10. In Figure 6-7 the paired links of a one hour simulation using a large sea state at the worst angle of the vessel is plotted. One notices the same quadratic trend between the quantities as using theoretic motions (Figure 6-2). (Legras, 2008) published similar results for deep water pipelay operations using the J-Lay method. The bottom tension was approximately quadratic with the heave velocity of a J-Lay vessel.

In Figure 6-8, the paired peaks of three different simulations are plotted using different sea states with different $\mathrm{H_S}$ and $\mathrm{T_Z}$ values. The magnitude of both quantities is smaller for a smaller sea state, but the relation between the quantities seems not affected.

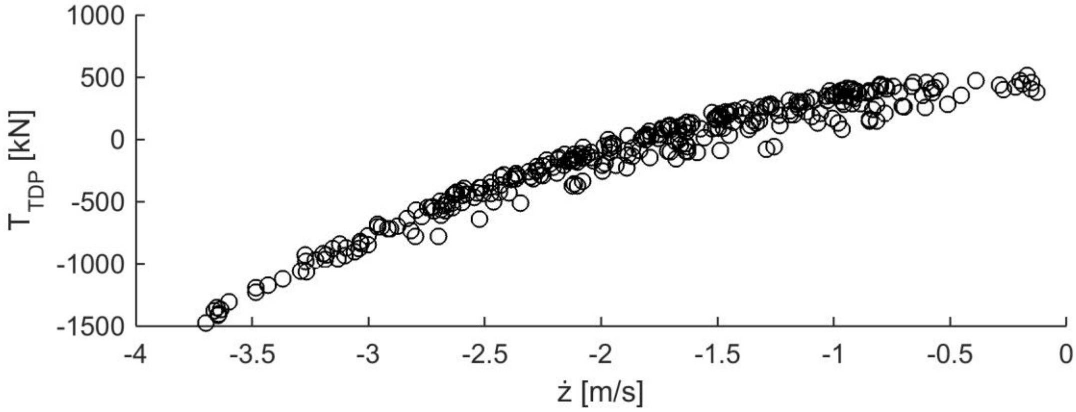

Figure 6-7 Scatterplot of $\dot{z}(t)$ vs T_{TDP} (BC1), JONSWAP spectra with $\mathrm{H_S} = 4.0m$, $\mathrm{T_Z} = 9.0s$, $\vartheta = 70°$, $t_{\mathrm{sim}} = 3600s$

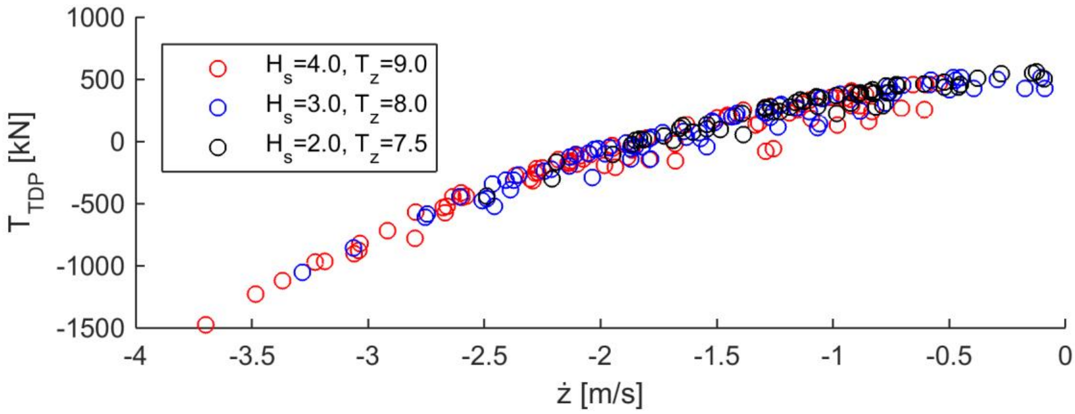

Figure 6-8 Scatterplot of $\dot{z}(t)$ vs T_{TDP} (BC1), Three simulations with different JONSWAP spectra, $\vartheta = 70°$, $t_{\mathrm{sim}} = 900s$

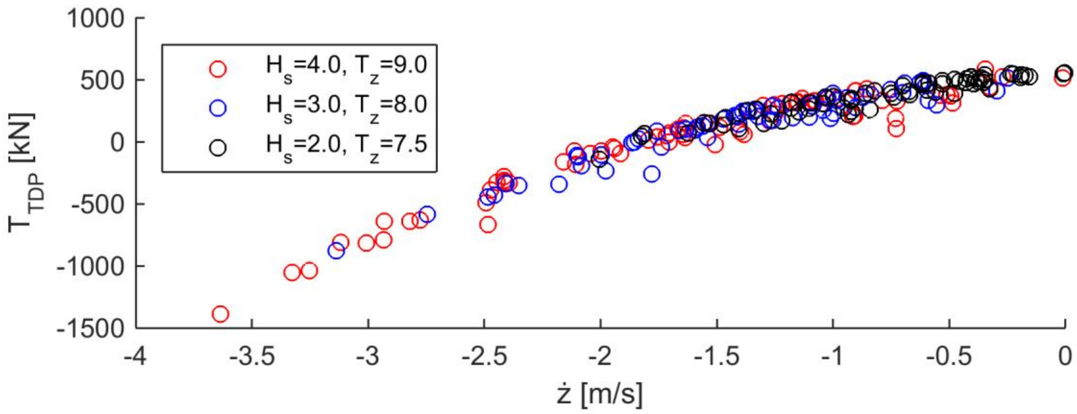

Figure 6-9 Scatterplot of $\dot{z}(t)$ vs T_{TDP} (BC1), Three simulations with different JONSWAP spectra, $\vartheta = 70°$, $t_{\mathrm{sim}} = 900s$ with wave directional spreading (20 components, $n = 8$)

In Figure 6-9 simulations with wave directional spreading are used. The dominant wave approach angle is $\vartheta = 70°$ (beam quartering waves). The wave heights will be spread to beam and quartering waves. Therefore large values of the paired peaks will occur less in comparison with the simulations used in Figure 6-8. Wave directional spreading does not affect the trend significantly. To create a better overview of wave approach dependency of the relation between effective bottom tension and vertical stinger tip velocity, nine short simulations are performed using the same $\mathrm{H_S}$ and $\mathrm{T_Z}$ values of Figure 6-7, but over nine different approach directions (without wave directional spreading). The results of the simulations are grouped in beam quartering waves, beam waves and a group containing all other approach directions. The results are shown in Figure 6-10. In section 5.1.2 was shown that beam quartering waves will cause the highest loads on the vessel which explains the large red trend in the scatterplot. A more interesting result is the variance the trend due to beam quartering and beam waves. In comparison with other wave approach directions, these directions deviate from the trend at particularly the lower magnitudes. In section 5.2.1 was described how the translational motions at the stinger tip were superposed from the six DOFs at COG. The roll, yaw and sway motions result in large out-of-plane horizontal motions at the stinger tip which have small influence at the maximum bending moments according to section 5.1.1. The axial motions of the pipeline at LOP do also have horizontal out-of-plane velocities which affect the effective tension. Fluid drag acts normal to the pipeline, thus the hydrodynamic load also affect the horizontal out-of-plane velocities of the pipeline. Therefore not only horizontal in-plane (XZ) stinger tip motions affect the pipeline axial motions, but also horizontal out-of-plane (YZ) motions do affect axial motions of the pipeline. The damping term of the effective tension at TDP is thus also affected by these horizontal out-of-plane pipeline velocities.

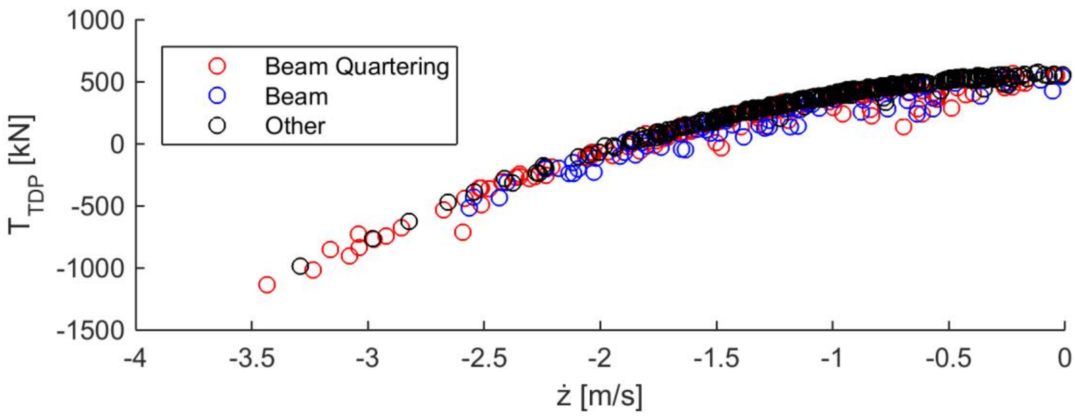

Figure 6-10 Scatterplot of $\dot{z}(t)$ vs T_{TDP} (BC1), nine simulations with different sea states, JONSWAP spectrum, $\mathrm{H_S} = 4.0m$, $\mathrm{T_Z} = 9.0s$, $t_{\mathrm{sim}} = 900s$. Beam Quartering waves ($\vartheta = 67.5°$, $\vartheta = 112.5°$), Beam waves ($\vartheta = 90°$), Other waves approach angles ($\vartheta = 0°$, $\vartheta = 22.5°$, $\vartheta = 45°$, $\vartheta = 135°$, $\vartheta = 157.5°$, $\vartheta = 180°$)

Large roll and sway motions occur for large waves with small frequency peaks in contrast to pitch and heave motions which occur for large waves with high frequency peaks. The minimum effective bottom tension is like the maximum bending moment primarily dependent on high frequency vessel motions. Because large vertical motions occur more frequent and have more influence on the bottom tension than horizontal motions in beam quartering waves (BC1), the maximum allowed effective bottom tension is dependent of the vertical stinger tip velocity. In other words, the out-of-plane motions on the stinger tip affect the relationship, but do not influence the relation between their maxima. However, if during a pipeline installation operation a sea state occurs with a large T_z in pure beam waves, large roll motions will significantly affect the bottom tension. However during offshore operations always some wave directional spreading is involved and therefore the theoretical pure beam waves do not exist in practical sense. Both pitch and heave motions are always involved in beam waves. Therefore (in case of BC1), vertical stinger tip motions still have more influence on the effective bottom tension than horizontal stinger tip motions.

6.1.3 Relation between vertical stinger tip motions and effective top tension

As described in the beginning of section 6.1, the effective top tension can be related to the vertical stinger tip motions using the mass-dashpot-spring representation. The inertia term $\mathrm{M}\ddot{z}(t)$ in equation (6.1) is largest at ST which is the assumed equal to the LOP location. The damping contributes a negligible amount of effective tension comparison with the inertia term and static term at ST. Using this assumption equation (6.1) will be rewritten to equation (6.3) which is a linear function.

$$T(t) = \mathrm{M}\ddot{\mathrm{z}}(t) + \mathrm{Kz}(t) + T_{\mathrm{sta}} \tag{6.3}$$

With the short simulations of harmonic vertical stinger tip motions used earlier in section 5.1.1 the relationship is plotted in the same way as Figure 6-2 which is shown in Figure 6-11. The relation between effective top tension and vertical stinger tip acceleration is well correlated for all different vertical stinger tip excitations. The assumption of a linear function is incorrect. A small slope in the figure is seen which implies that the damping do have some minor influences. For an effective tension value of 8000 kN and upwards, some nonlinear effects are experienced.

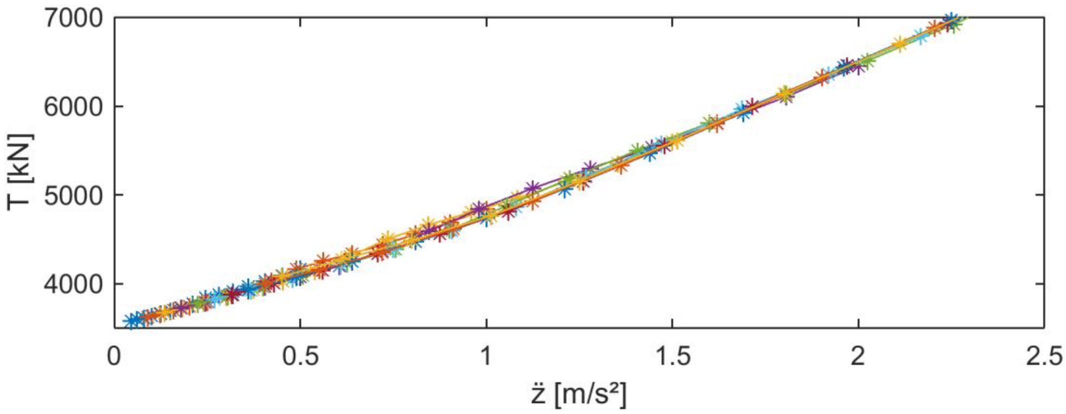

Figure 6-11 Relation between vertical stinger tip acceleration and effective top tension (BC1) using 150 short simulations containing vertical stinger tip excitations with different frequencies and amplitudes

Using the stochastic sea state and pairing peak method of section 6.1.1, the paired peaks are found between effective top tension and vertical stinger tip acceleration. They are plotted for different directions in Figure 6-12. Also for this criterion, beam waves and beam quartering waves affect the relation. The out-of-plane horizontal motions resulting from beam waves influence the effective tension. Because they respond to low frequencies and large vertical stinger tip motions to high frequencies, the criterion limit is not affected in the same way as the vertical stinger tip velocity criterion of section 6.1.1.

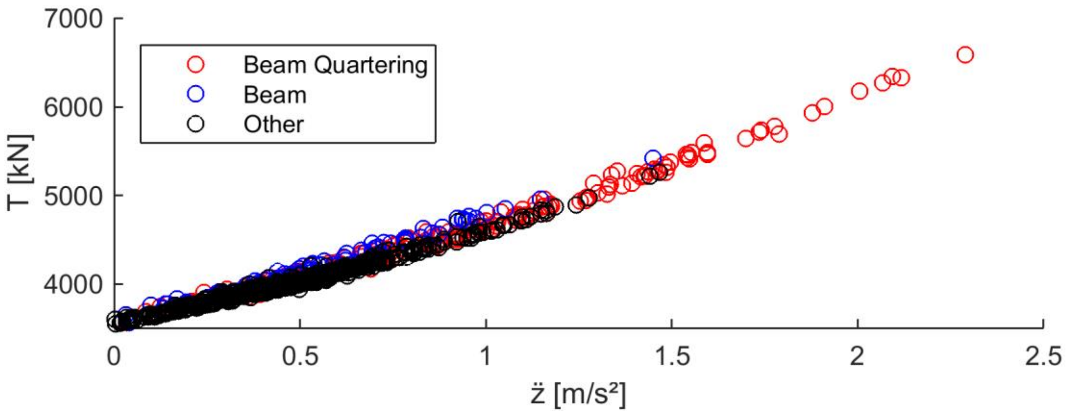

Figure 6-12 Scatterplot of $\ddot{z}(t)$ vs T (BC1), nine simulations with different sea states, JONSWAP spectrum, $\mathrm{H_S} = 4.0$, $\mathrm{T_Z} = 9.0s$, $t_{\mathrm{sim}} = 900s$. Beam Quartering waves ($\vartheta = 67.5°$, $\vartheta = 112.5°$), Beam waves ($\vartheta = 90°$), All other waves approach angles ($\vartheta = 0°$, $\vartheta = 22.5°$, $\vartheta = 45°$, $\vartheta = 135°$, $\vartheta = 157.5°$, $\vartheta = 180°$)

6.2 Relation between effective tension and bending moment

In the introduction and chapter 3.0 and 4.0, the relation between tension and bending moment is described. In deep water projects the maximum bending moments in the sagbend usually occur in the TDA close to the location of the maximum static bending moment of the pipeline. If the pipeline leaves the stinger almost perpendicular to the seabed (like BC1) this is always the case. In this section FEA simulations of the base cases are used to further improve the relationship between effective tension and bending moment.

6.2.1 Constant effective tension in TDA

One can assume that the static effective tension in the TDA is equal to the static effective bottom tension (Figure 6-13).

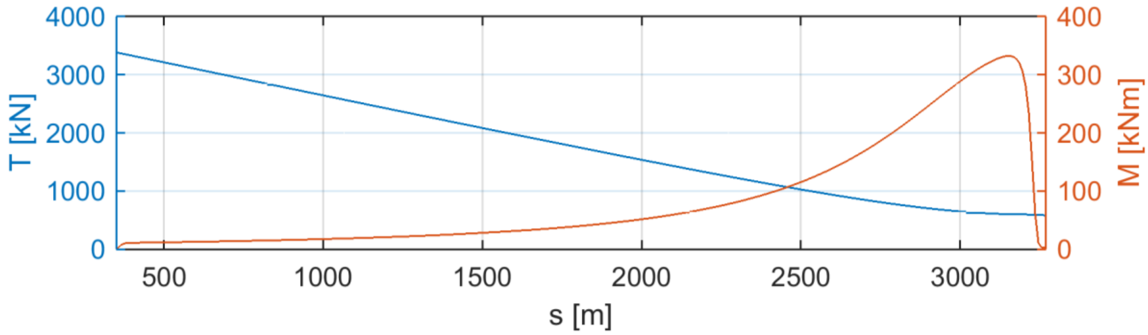

Figure 6-13 Static comparison of effective tension and bending moment in the sagbend (BC1)

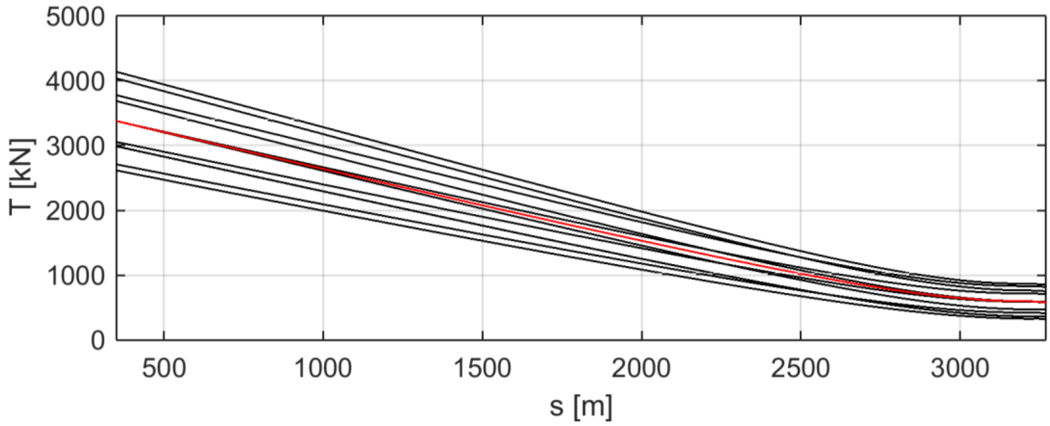

Figure 6-14 Dynamic effective tension due to a harmonic wave (BC1) with $H = 1$, $\omega = \frac{\pi}{4}\,\mathrm{rad}/s$, $\vartheta = 70°$

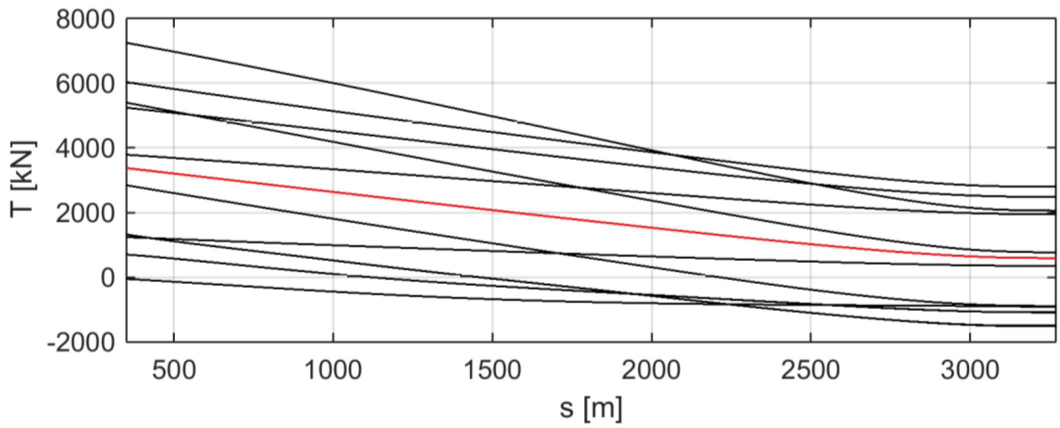

Figure 6-15 Dynamic effective tension due to a harmonic wave (BC1) with $H = 4$, $\omega = \frac{\pi}{4}\,\mathrm{rad}/s$, $\vartheta = 70°$

The dynamic tension excites around the steady state condition In Figure 6-14 is seen that the dynamic effective tension is almost parallel to the static effective tension (red line). For the larger excitation in Figure 6-15, the dynamic effective tension will deviate more less parallel to the static effective tension. However in the TDA, the dynamic effective tension is still parallel to the static effective tension. One can assume that the dynamic tension in the TDA at each time step is distributed uniform over length and equal to the dynamic effective tension at TDP. Therefore the maximum total bending moment occurs at a section with an effective tension equal or close to the effective bottom tension.

6.2.2 Time history comparison

Compressive dynamic axial tension peaks at TDP will likely result into bending moment peaks in the TDA. This can be visualised using the time histories of the bending moment on the element mid-point containing the maximum bending moment and the effective tension at TDP. In Figure 6-16 are two snapshots of time histories during a dynamic analysis of BC1 using an irregular sea state. The bending moment is taken on the element containing the maximum bending moment. The compressive downwards peaks of the effective tension show good correlation with the upwards peaks of the bending moment.

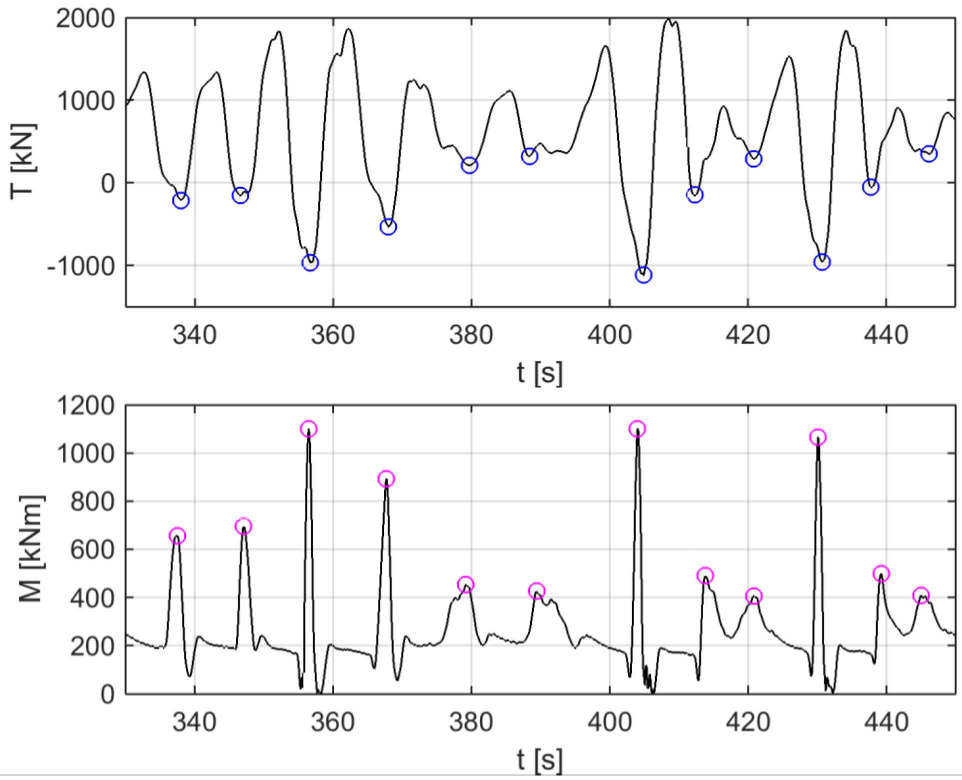

Figure 6-16 Effective tension at TDP (downward peaks) and bending moment a the mid-point of the element containing the maximum bending moment (upward peaks) (BC1)

The pairing peak method used earlier to compare vertical stinger tip motions and axial tension could be used for the bending moment. However unlike the effective tension, the maximum bending moment on the unsupported pipeline during the period of each dynamic tension peak is constantly shifting on different elements. One could use the element mid-point of the largest bending moment to find the relation between the highest bending moment and lowest effective tension during a simulation (Passano & Larsen, 2006). Better is to find the relation between effective tension and the highest bending moment at all the elements in the TDA. The shifting can be explained using the modal analysis of 4.3. For higher frequencies the last peak of the bending moment in the TDA shifts closer to TDP. This is because at larger frequencies, larger axial motions in the pipeline occur which result in larger normal motions in the TDA. Since TDP is modelled as a hinged support on the seabed a rope effect in the last sections of pipeline occurs. The rope effect for a small beam element is described in in section 3.5.1. For the pipeline modelled as a supported beam, the rope effect has a strong presence.

6.2.3 Correlation between effective tension and bending moment in TDA

In section 4.3 was seen that for different frequencies, the maximum bending moment in the sagbend will shift on different positions on the pipeline. The program used earlier in 6.1.1 for comparing quantities on a node or element is now modified to find for each effective bottom tension peak in the time history, the corresponding maximum bending moment peak of all the elements in the TDA. Together they form paired peaks and are plotted into a scatter diagram shown in Figure 6-17. One sees in Figure 6-17 that for decreasing effective tensions, the bending moment increases. The effective tension and bending moment show good correlation for small excitations. For larger dynamic effective tension also the variation of the bending moments increases. The largest bending moment is not always on the same position as the maximum static bending moment. For increasing excitations, the dynamic bending moment peaks are shifting over the pipeline in the TDA and therefore cause extreme bending moments at different positions of the pipeline. The scatterplot of the dynamic bending moment (Figure 6-18) show marginal better results. The variation of dynamic bending moment begins to increase if the pipeline axial loading is in compression (negative effective tension).

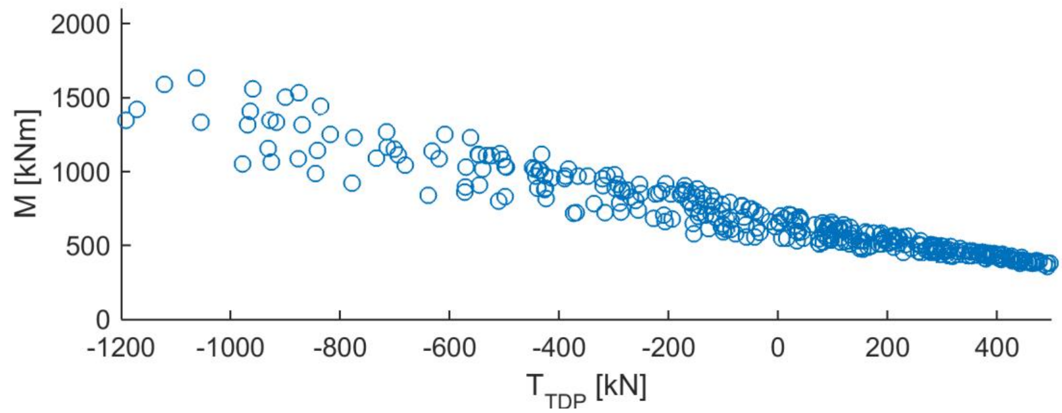

Figure 6-17 Scatterplot T_{TDP} vs M (BC1), JONSWAP spectra with $\mathrm{H_S} = 4.0m$, $\mathrm{T_Z} = 9.0s$, $\vartheta = 70°$, $t_{\mathrm{sim}} = 3600s$

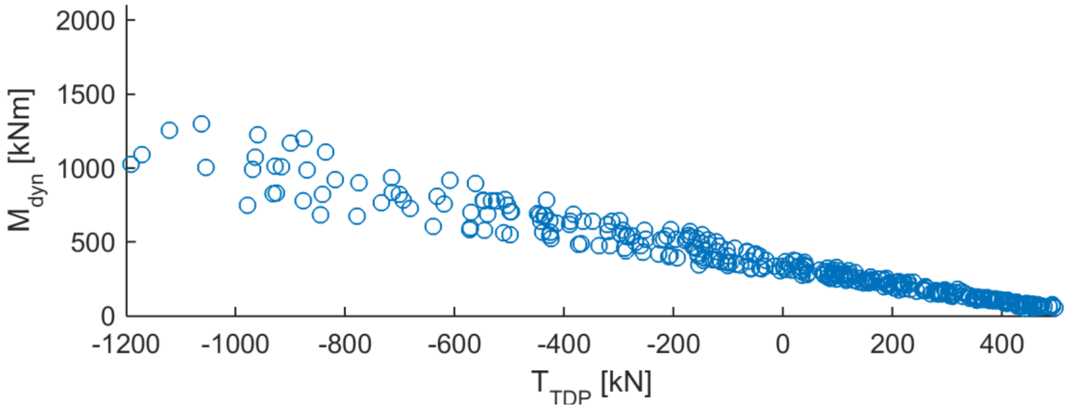

Figure 6-18 Scatterplot T_{TDP} vs M_{dyn} (BC1), JONSWAP spectra with $\mathrm{H_S} = 4.0m$, $\mathrm{T_Z} = 9.0s$, $\vartheta = 70°$, $t_{\mathrm{sim}} = 3600s$

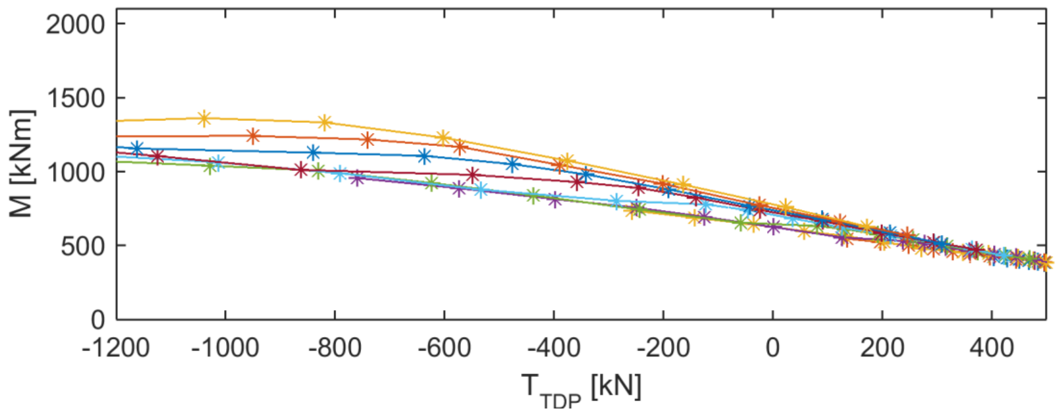

Figure 6-19 Relation between effective bottom tension and bending moment using 150 short simulations containing vertical stinger tip excitations with different frequencies and amplitudes (BC1)

Using the 150 short simulations with diverse harmonic vertical stinger tip motions, the relation between effective bottom tension and maximum bending moment can be visualized (Figure 6-19). It shows that for vertical excitation of the stinger tip, the same sort of deviation for decreasing effective tension occurs. Concluded can be that large excitations cause different magnitudes of bending moment for an equal amount of effective bottom tension. The origin of the nonlinear effect has to do with the shape of the pipeline in the sagbend. It is known as geometric nonlinear behaviour (Passano & Larsen, 2006).

6.2.4 Geometric nonlinear behaviour

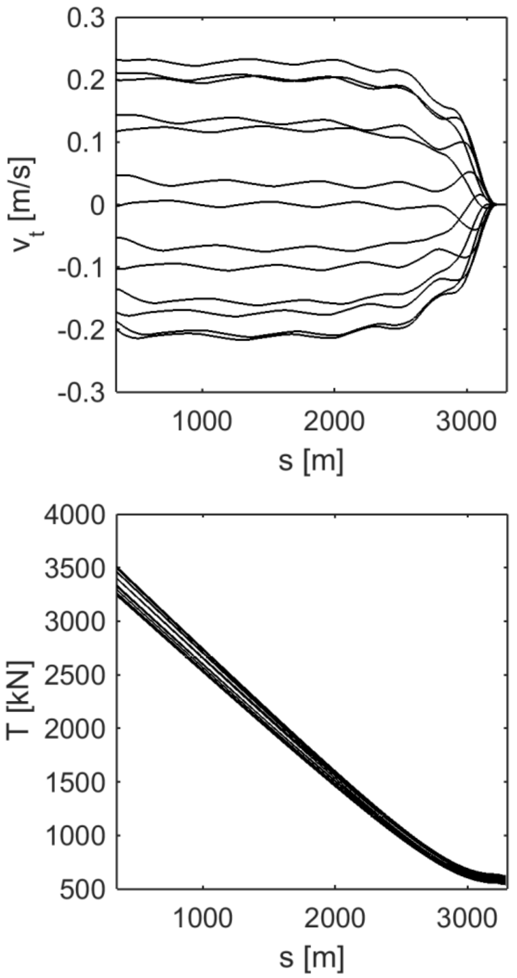

Figure 6-20 axial velocity and effective tension along the pipeline (BC1) by horizontal excitation of the stinger tip ω=0.6 [rad/s] and amplitude=2.0 [m]

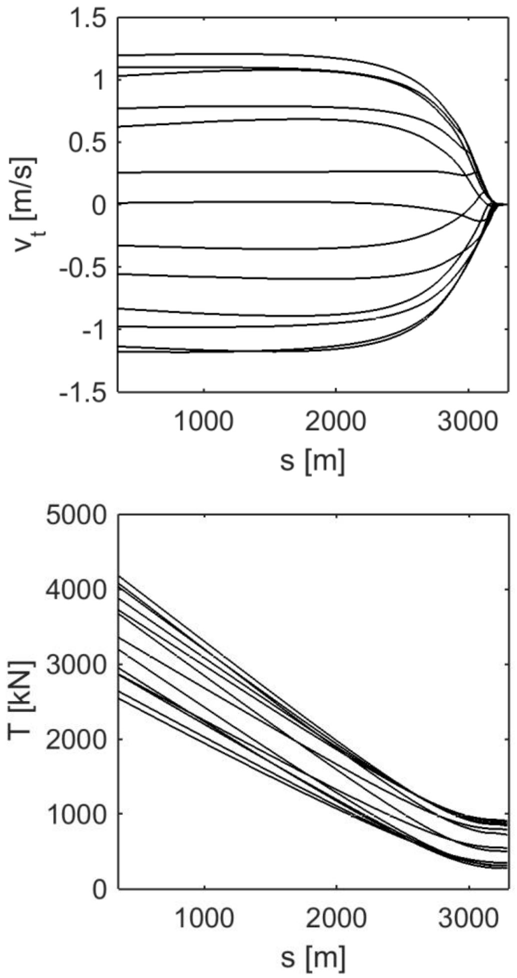

Figure 6-21 axial velocity and effective tension along the pipeline (BC1) by vertical excitation of the stinger tip ω=0.6 [rad/s] and amplitude=2.0 [m]

In 6.1.1 is described how axial motions are directly related to axial effective tension. In section 5.1.1 is described that for deep water cases like BC1 large axial motions in the pipeline occur for vertical stinger tip motions with large amplitudes and high frequencies. Horizontal stinger tip excitation for BC1 cause also (small) axial motions in the pipeline. The progress of horizontal induced axial velocity in the pipeline is similar to the progress of vertical induced axial velocity. For both excitations at the stinger tip, axial pipeline velocity follows a progress similar to the effective tension along the unsupported pipeline (Figure 6-20 and Figure 6-21). The figures are made using horizontal and vertical harmonic excitation of the vessel at the location of the stinger tip for one period after the steady state solution. In the lower half of the sagbend where the effective tension is decreasing, the axial velocity will decrease too till zero at TDP. Note that the horizontal excitation of the stinger tip (Figure 6-20) gives some axial resonance in the pipeline. This axial resonance is small and has thus very limited influence on the dynamic tension which is also small for horizontal excitation. Furthermore for both the horizontal and vertical excitation, the positive axial velocities equal the negative axial velocities which also are the case for the dynamic effective tension around its static value. Both dynamic situations could be effectively linearized using the full nonlinear time domain solution (for example the method used in 6.1.3) or a FD approach using transfer functions (Chatjigeorgiou, 2008).

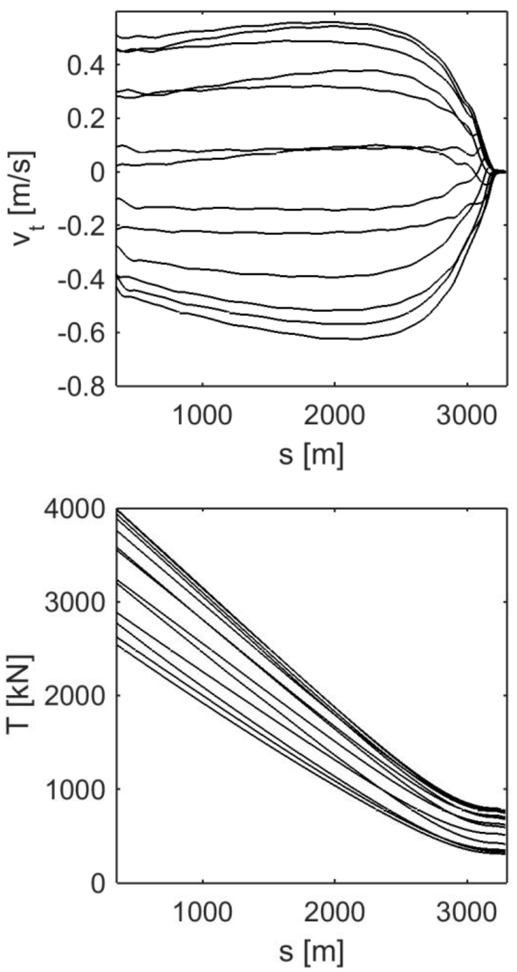

Figure 6-22 axial velocity and effective tension along the pipeline (BC1) by horizontal excitation of the stinger tip ω=1.2 [rad/s] and amplitude=2.0 [m]

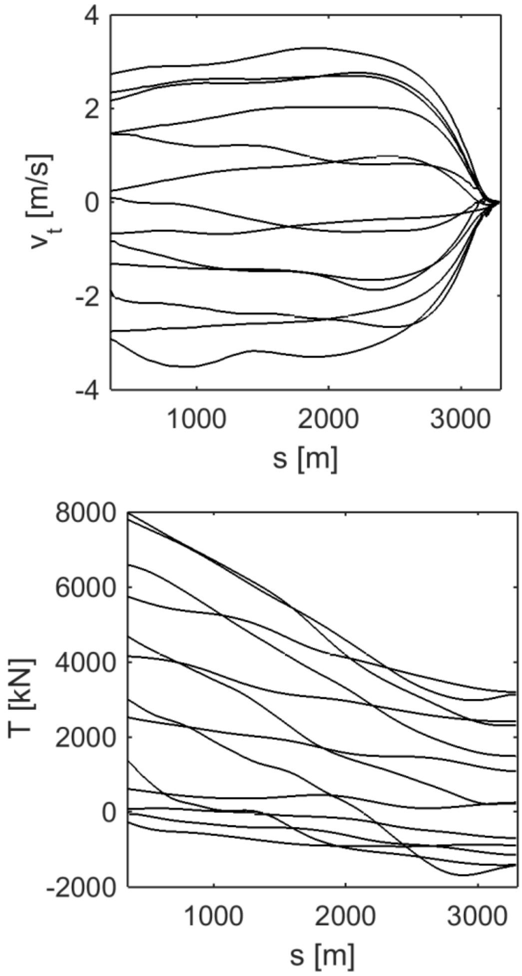

Figure 6-23 axial velocity and effective tension along the pipeline (BC1) by vertical excitation of the stinger tip ω=1.2 [rad/s] and amplitude=2.0 [m]

If for both excitations the frequency is doubled to ω = 1.2 rad/s (Figure 6-22 and Figure 6-23), one notices that the dynamic tension due to vertical excitation is negative and compression will occur. Through the larger excitations, the axial velocity due to vertical excitation shows variations along the length of the pipeline. The same behaviour is noticed for the effective tension of the vertical excitation.

The progress of the pipeline normal motions from lift off point till TDP is presented in Figure 6-24 and Figure 6-25. One notices that the progress of the pipeline's normal velocity is different in comparison with its axial velocity. The horizontal excitation of the stinger tip results in large normal velocities in the pipeline which decrease in magnitude at the TDA. For a vertical stinger tip excitation, the normal velocity of the pipeline has an increased peak in the TDA. Although the normal velocity of the pipeline at lift off point is larger for the horizontal excitation in comparison with vertical excitation, the normal velocity in the TDA is evidently larger for vertical excitations. Note that the dynamic bending moment follows the progress of the normal velocity of the pipeline. The bending moment is related to the normal velocity in the pipeline which was shown in the modal analyses of the basic cases (section 4.3). The maximum total bending moment occurs in the TDA at the segment for the maximum static bending moment for both excitations. If the frequency is doubled (Figure 6-26 and Figure 6-27) then also the normal velocity and total bending moment for large vertical excitation result into nonlinear peaks.

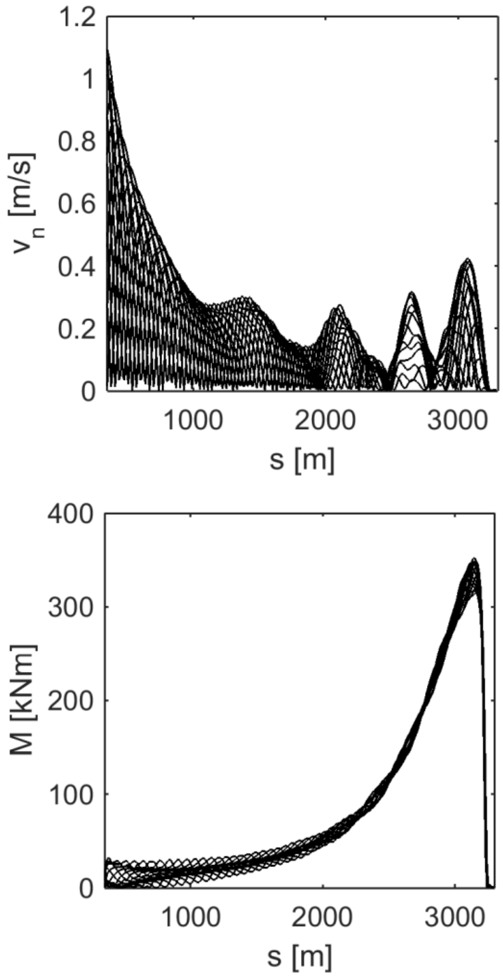

Figure 6-24 normal velocity and total bending moment along the pipeline (BC1) by horizontal excitation of the stinger tip ω=0.6 [rad/s] and amplitude=2.0 [m]

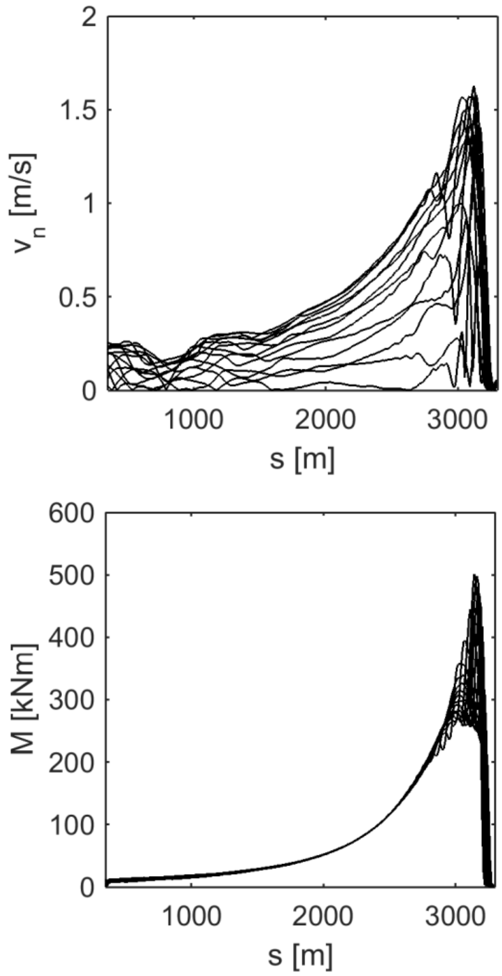

Figure 6-25 normal velocity and total bending moment along the pipeline (BC1) by vertical excitation of the stinger tip ω=0.6 [rad/s] and amplitude=2.0 [m]

Earlier was described that the axial velocity of the pipeline is related with the effective tension and bending moment in the pipeline. The normal velocity is also related with the bending moment. This was noticed earlier during the modal analysis of Figure 4-7. The axial and normal motions of the pipeline are also related to each other. The coupling of axial and normal motions results in the geometric nonlinearities (Chatjigeorgiou & Mavrakos, 2010). From mathematical perspective the geometric nonlinearities originate from the $T\kappa$ term in equation (3.29).

The geometric nonlinearities increase for increasing motions of the stinger tip. For large vertical stinger tip excitations with high frequencies and large amplitudes the dynamic effective tension is larger than its static counterpart and compressive effects occur. The axial motions and normal motions of the pipeline at the top are coupled and result in normal motions at the bottom. The starting geometric nonlinearities begin to affect the relation between effective tension and bending moment. Such behaviour is shown in Figure 6-23 and Figure 6-27. The large peaks of normal velocity and bending moment in the latter figure are the result of nonlinear behaviour. This peak does not follow the trend between effective tension and bending moment found in 6.2.3. Fortunately this particular excitation is exaggerated and is very unlikely to happen offshore. Also at such deep water depths like BC1, the excitation should be enormous and the tensioners should be on the brake to create noticeable geometric nonlinear effects. Unfortunately, for other load cases at shallower water depths, geometric nonlinearities occur for less large and existent and even common excitations.

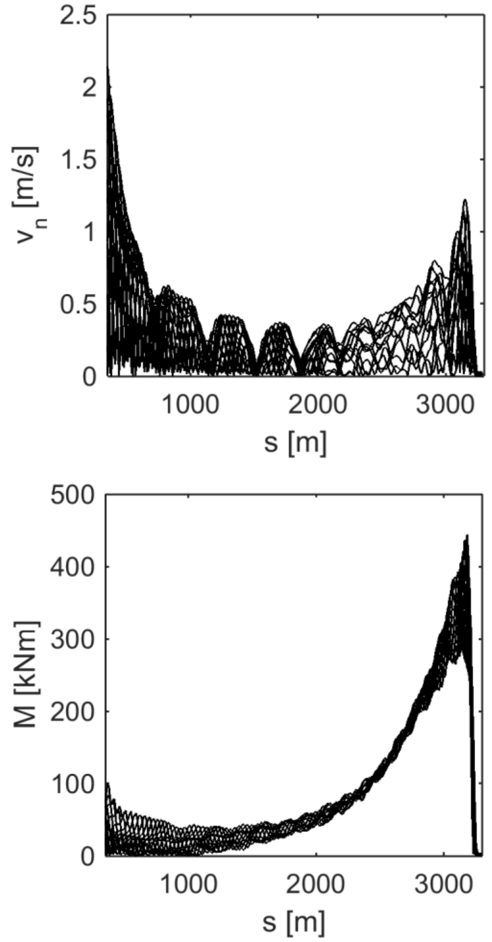

Figure 6-26 normal velocity and total bending moment along the pipeline (BC1) by horizontal excitation of the stinger tip ω=1.2 [rad/s] and amplitude=2.0 [m]

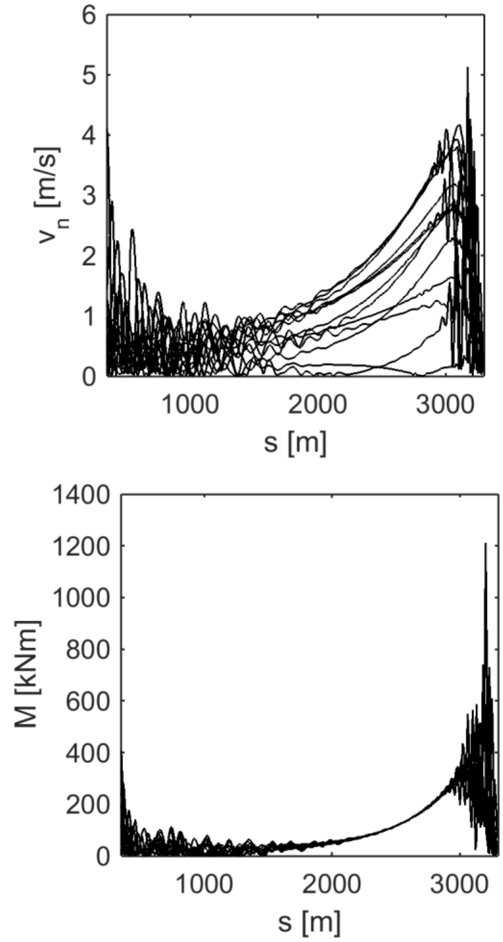

Figure 6-27 normal velocity and total bending moment along the pipeline (BC1) by vertical excitation of the stinger tip ω=1.2 [rad/s] and amplitude=2.0 [m]

6.2.5 Influence of water depth on nonlinear behaviour

The effects of the nonlinearities increase with decreasing water depth. For shallow water projects, the pipeline leaves the stinger more parallel to the seabed. The departure angle is likely to be less than 70°. BC2 has a departure angle of 40° which means that the horizontal component of the unsupported span length is larger than the vertical component. Therefore the horizontal motions at the stinger tip have significant higher axial contribution in comparison with BC1. Also the vertical stinger tip motions have more normal contribution at LOP. The coupling between axial and normal motions in the pipeline result in stronger fluctuations and thus large geometric nonlinear behaviour for even small excitations in the TDA. Fortunately, the static bending moment is so small, that the maximum bending moment occurs in the STA, where the motions of the pipeline are not so much affected by geometric nonlinearities.

For BC3 with tensioners on the brake in 92m water depth, the axial velocity, normal velocity, effective tension and total bending moment is plotted for a horizontal and vertical excitation in Figure 6-28 and Figure 6-29. Horizontal excitation is dominant at this water depth and thus causes the largest axial motions which result in the highest effective tensions and bending moments. The dominant directions of excitation also cause the largest geometric nonlinearities. The dynamic effects are very large at shallow water depths taken into account that a much smaller (and existent) excitation is used in comparison with the excitation used for BC1.

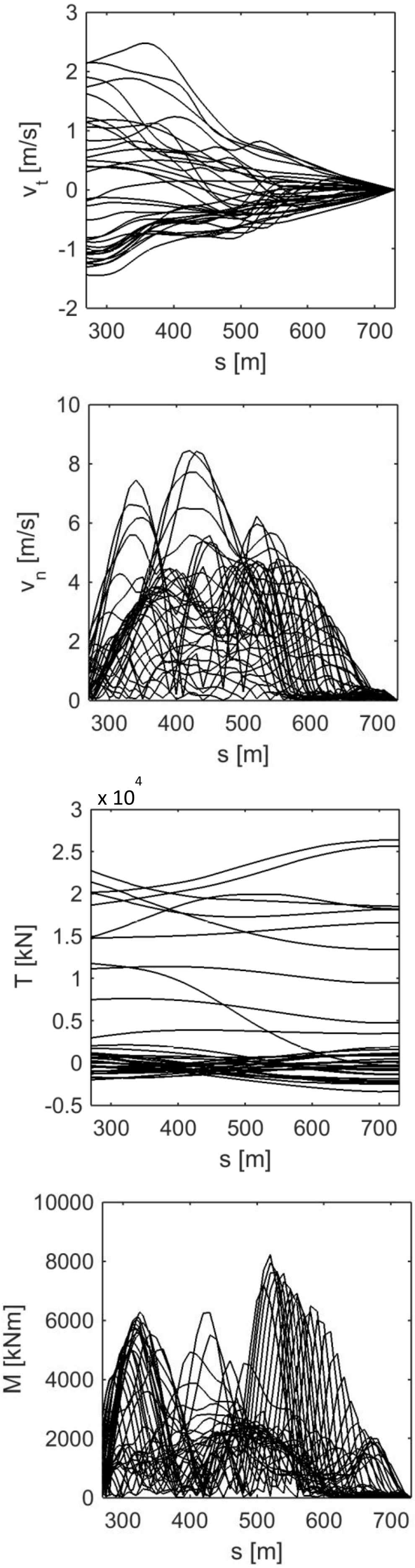

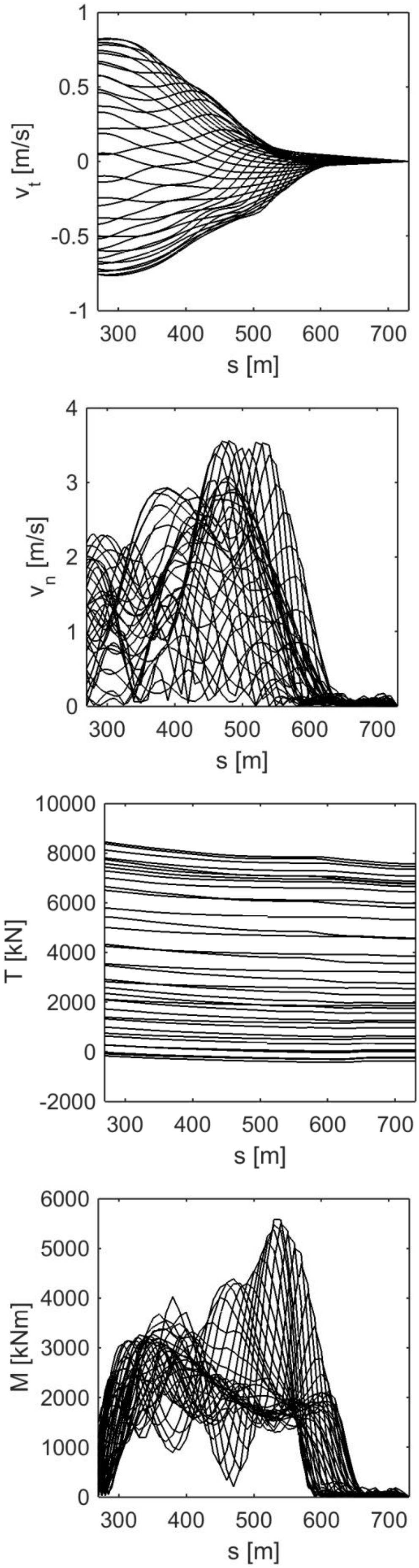

Figure 6-28 axial velocity, normal velocity, effective tension and total bending moment along the pipeline (BC3) by horizontal excitation of the stinger tip ω=0.9 [rad/s] and amplitude=2.0 [m]

Figure 6-29 axial velocity, normal velocity, effective tension and total bending moment along the pipeline (BC3) by vertical excitation of the stinger tip ω=0.9 [rad/s] and amplitude=2.0 [m]

Till now horizontal motions were considered in the dominant plane of bending (XZ-plane). For both horizontal and vertical motions of the stinger tip in the plane of bending (Figure 6-28 and Figure 6-29) no binormal movements of the pipeline occurred. On the other hand if the stinger tip is excited by an out-of-plane horizontal motion (in Y-direction), still axial and normal motions of the pipeline occur. Likewise in-plane dynamic bending moments occur. The in-plane bending moments resulting from out-of-plane motions are also caused by geometric nonlinearities (Chatjigeorgiou & Mavrakos, 2009). Its nonlinear behaviour is shown in Figure 6-30 and Figure 6-31. Note that some out-of-plane moments are larger than its in-plane equivalent. This is because of out-of-plane resonance which can be described with an additional modal analysis analogous to section 4.3.

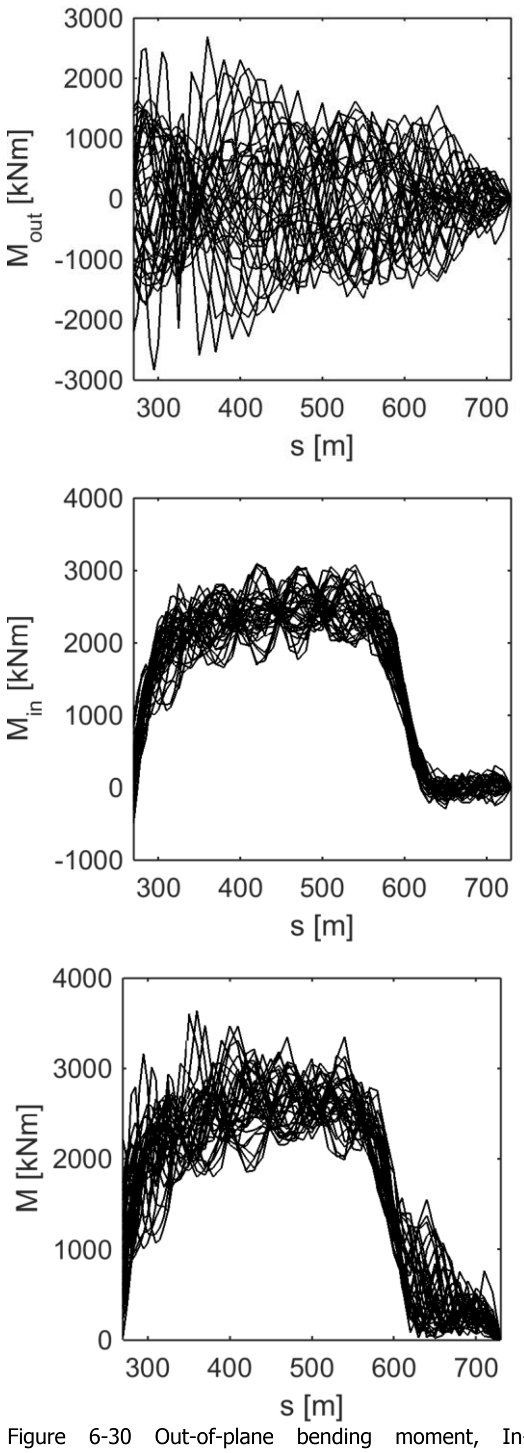

Figure 6-30 Out-of-plane bending moment, In-plane bending moment and total bending moment along the pipeline (BC3) by out-of-plane horizontal excitation of the stinger tip ω=0.9 [rad/s] and amplitude=2.0 [m]

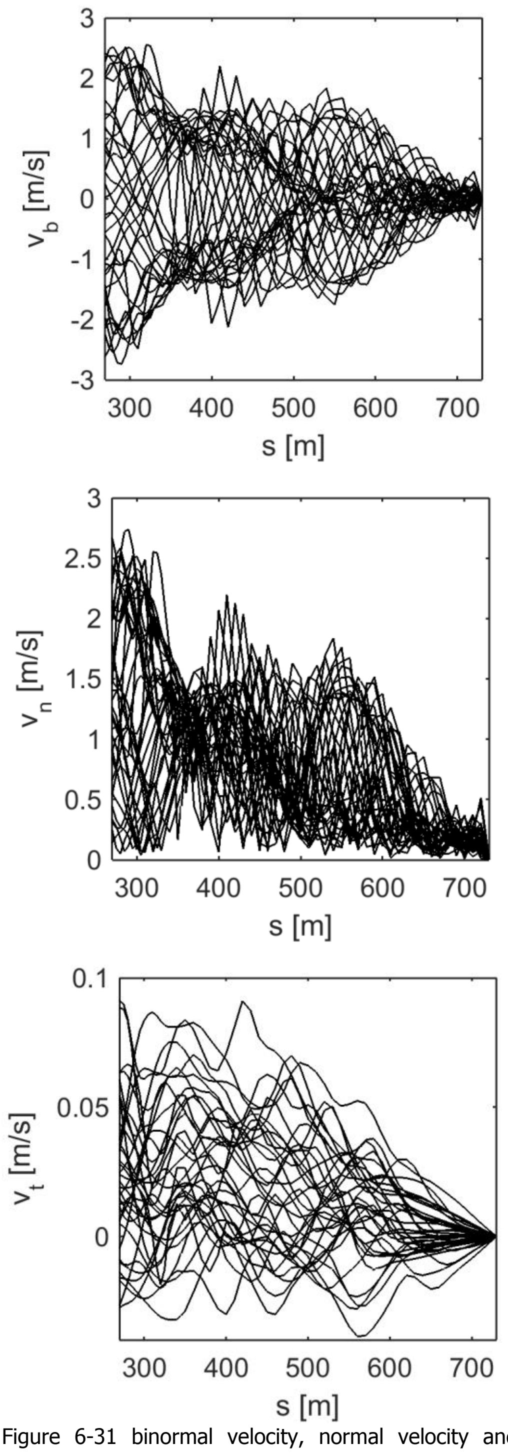

Figure 6-31 binormal velocity, normal velocity and axial velocity along the pipeline (BC3) by out-of-plane horizontal excitation of the stinger tip ω=0.9 [rad/s] and amplitude=2.0 [m]

The mode shapes of the binormal motions along the pipeline give the shape of the out-of-plane bending moments (Figure 6-32). Because there is no out-of-plane bending in the static state situation, the first mode shape is present (Table 6-1). The first two natural frequencies are frequently excited by the vessel motions which can lead to large resonance effects. This resonance is seen in Figure 6-30. From the second mode onwards, the natural frequencies are close to the natural frequencies of the in-plane modes (Table 4-5).

Mode [-]	ω_n [rad/s]
1	0.365
2	0.758
3	1.204
4	1.719
5	2.314

Table 6-1 Eigenfrequencies of the out-of-plane mode shapes (BC3)

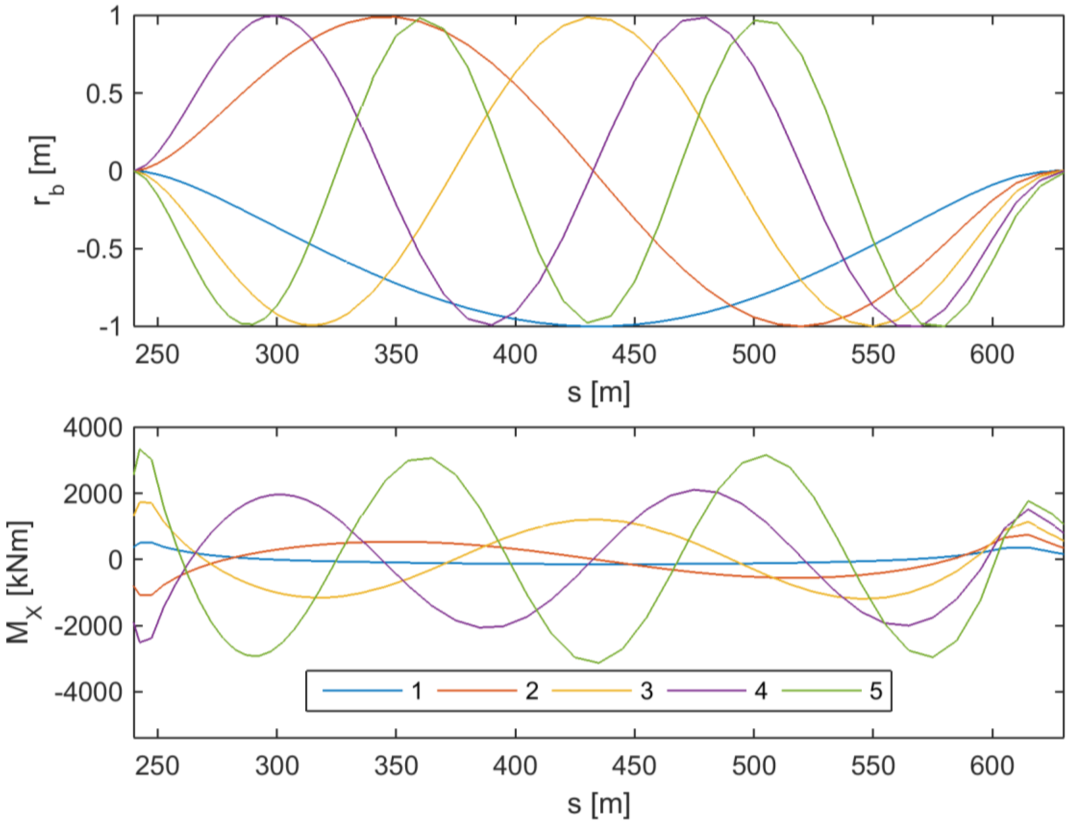

Figure 6-32 First 5 mode shapes for the binormal motions along the pipeline (up) and out-of-plane dynamic bending moment along the pipeline (down) (BC3)

The distance between two peaks of the first two mode shapes is relatively large. Therefore the out-of-plane bending moment is excited on a large variation of the pipeline, which leads to geometric non-linear behaviour. Because also in-plane excitations are amplified by out-of-plane horizontal stinger tip motions, the out-of-plane stinger tip motions have a significant influence on the geometric nonlinear behaviour in shallow water.

6.3 Relation between vertical stinger tip motions and extreme bending moments

In previous sections was described that for deep water projects the dynamic tension or length can be related to the vertical stinger tip motions and the maximum bending moment can related to effective tension. Using both relations a direct relation between vertical stinger tip motions and the maximum bending moment in the pipeline can be obtained.

6.3.1 Correlation between vertical stinger tip velocity and bending moment in the TDA

Using the 150 simulations of 6.1.1 containing vertical stinger tip motions with different amplitudes and frequencies, the correlation between vertical stinger tip velocity and maximum bending moment (in the TDA) is shown in Figure 6-33. For increasing amplitudes (lines) and frequencies (points), the bending moment increases. However for some large excitations, the fluctuating maximum bending moment which is a result of the geometric nonlinear behaviour due to the coupling of vertical and horizontal (both in-plane and out-of-plane) motions of the pipeline.

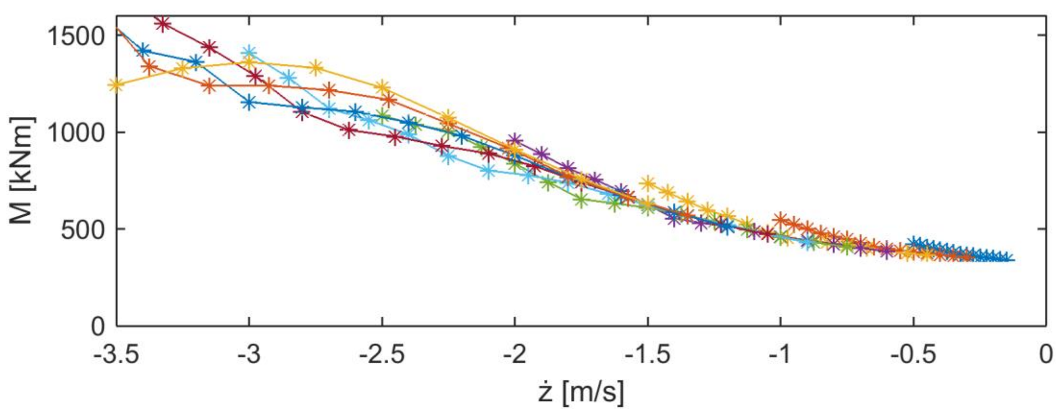

Figure 6-33 Relation between vertical stinger tip velocity and bending moment using 150 short simulations containing vertical stinger tip excitations with different frequencies and amplitudes (BC1)

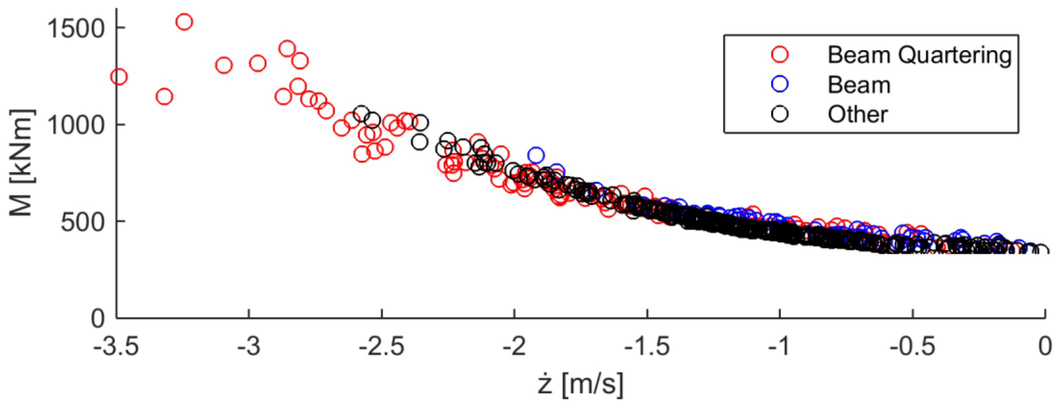

Figure 6-34 Scatterplot of $\dot{z}(t)$ vs M (BC1), nine simulations with different sea states, JONSWAP spectrum, $\mathrm{H_S} = 4.0m$, $\mathrm{T_Z} = 9.0s$, $t_{\mathrm{sim}} = 900s$. Beam Quartering waves ($\vartheta = 67.5°$, $\vartheta = 112.5°$), Beam waves ($\vartheta = 90°$), All other waves approach angles ($\vartheta = 0°$, $\vartheta = 22.5°$, $\vartheta = 45°$, $\vartheta = 135°$, $\vartheta = 157.5°$, $\vartheta = 180°$)

Using the modified paired peak method used in 6.2.3 the scatterplot in Figure 6-34 is made. The out-of-plane motions caused in beam waves and beam quartering waves influence the correlation for low frequencies. For high frequencies and amplitudes, the geometric nonlinear behaviour is seen. This phenomenon occurs by high frequency and large amplitude waves approaching the vessel in all directions. As for beam quartering waves, the bending moments are largest and thus also the geometric nonlinear behaviour is largest.

As is described in 3.3.1, the bending moment dominates the pipeline integrity regarding local buckling. Within pipeline engineering it is common and more accurately to check the equivalent von Mises strain as is described in 3.3.2. For both the short simulations of harmonic stinger tip motions and stochastic simulations using sea states, the equivalent von Mises strain is presented in Figure 6-35 and Figure 6-36. Both plots are quite similar compared to the ones of the previous page. This is because bending moment result in bending strain which dominates the equivalent von Mises strain. Similar conclusions are found in (Gong, et al., 2014) and (Ogink, 2001).

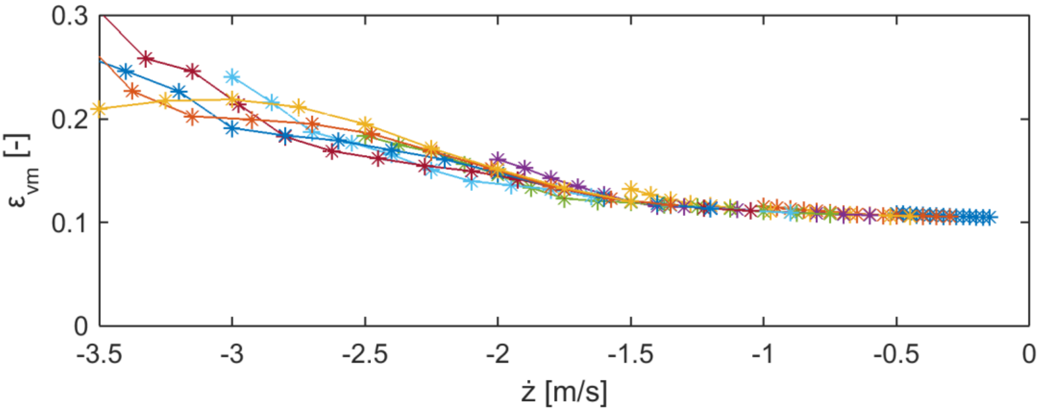

Figure 6-35 Relation between vertical stinger tip velocity and maximum equivalent von Mises strain using 150 short simulations containing vertical stinger tip excitations with different frequencies and amplitudes (BC1)

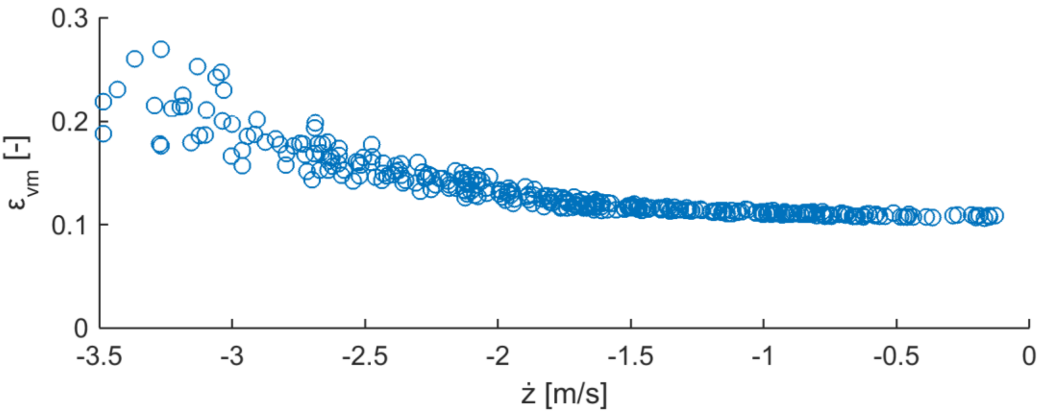

Figure 6-36 Scatterplot of $\dot{z}(t)$ vs $\varepsilon_{\rm vm}$ (BC1), JONSWAP spectrum with $\mathrm{H_S} = 4.0m$, $\mathrm{T_Z} = 9.0s$, $\vartheta = 70°$, $t_{\rm sim} = 3600s$

6.3.2 Correlation between vertical stinger tip acceleration and bending moment in the STA

In 6.1 and 6.1.3 was described that the vertical stinger tip acceleration is related to the effective tension at the stinger tip which is equal to the effective top tension. Using this relation also a relation can be obtained between vertical stinger tip acceleration and the maximum bending moment in the STA. For BC2 a perfect tensioner is used in the simulation. Tensioners on the brake demand tension values exceeding three times the tension capacity of the vessel. Also such tension results in large tensile strains. With the modified paired peak method of 6.2.3 and the simulations of BC2 excited by irregular sea states, the relation is shown in Figure 6-37 and Figure 6-38.

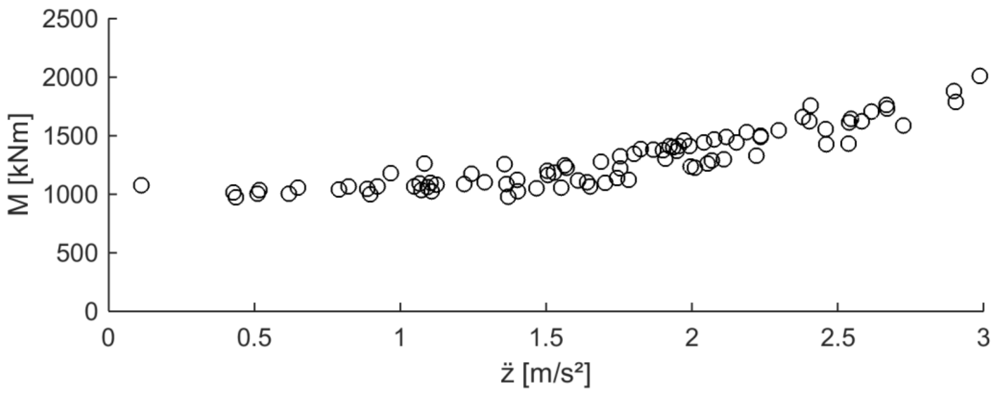

Figure 6-37 Scatterplot of $\ddot{z}(t)$ vs M (BC2), JONSWAP spectrum with $\mathrm{H_S} = 4.0m$, $\mathrm{T_Z} = 9.0s$, $\vartheta = 70°$, $t_{\mathrm{sim}} = 1800s$

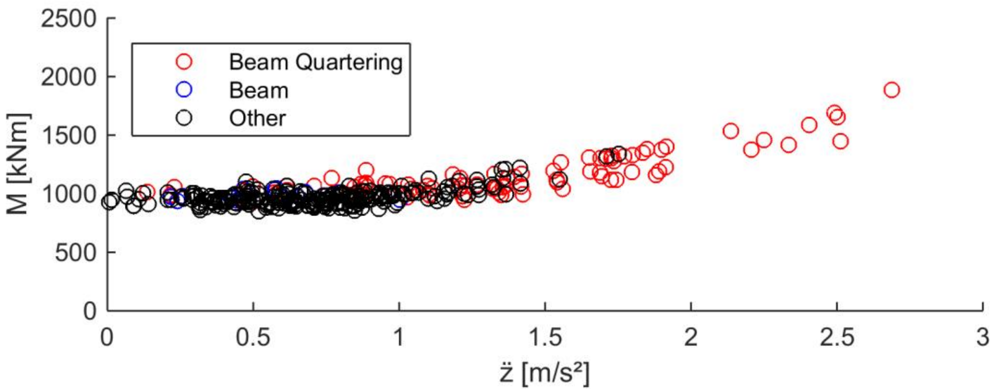

Figure 6-38 Scatterplot of $\ddot{z}(t)$ vs M (BC2), nine simulations with different sea states, JONSWAP spectrum, $\mathrm{H_S} = 4.0m$, $\mathrm{T_Z} = 9.0s$, $t_{\mathrm{sim}} = 900s$. Beam Quartering waves ($\vartheta = 67.5°$, $\vartheta = 112.5°$), Beam waves ($\vartheta = 90°$), All other waves approach angles ($\vartheta = 0°$, $\vartheta = 22.5°$, $\vartheta = 45°$, $\vartheta = 135°$, $\vartheta = 157.5°$, $\vartheta = 180°$)

In both figures, the trend is noticeable. Because gravity acts in vertical direction, the vertical stinger tip accelerations dominate the inertia effects which cause the bending moments. Beam waves and beam quartering waves do not affect the trend which implies that out-of-plane horizontal motions of the pipeline have minor influences at this relation. The in-plane horizontal and vertical motions of the stinger tip will cause alternating axial and normal motions of the pipeline. The coupling of these motions results in geometric nonlinearities which is the origin of the evident variation in the trend.

6.3.3 Correlation between vertical stinger tip motions and bending moment in shallow water depths

If a large stinger radius like the one in BC2 is used and the maximum bending moments particularly occur in the TDA, the proposed vessel motion based criteria of 6.3.1 and 6.3.2 fail. This typically occurs in more shallow water for which the geometric nonlinearities are large (BC3). This behaviour is shown in Figure 6-39 and Figure 6-40. Both figures show almost random scatter. The maximum bending moments occur on many locations of the pipeline. The coupling between axial and normal motions along the pipeline and the coupling between axial and bi-normal motions along the pipeline lead to large geometric nonlinearities. Also the out-of-plane bending moments have some contribution to the total resulting bending moments. Both sources of geometric nonlinearities are described in section 6.2.5.

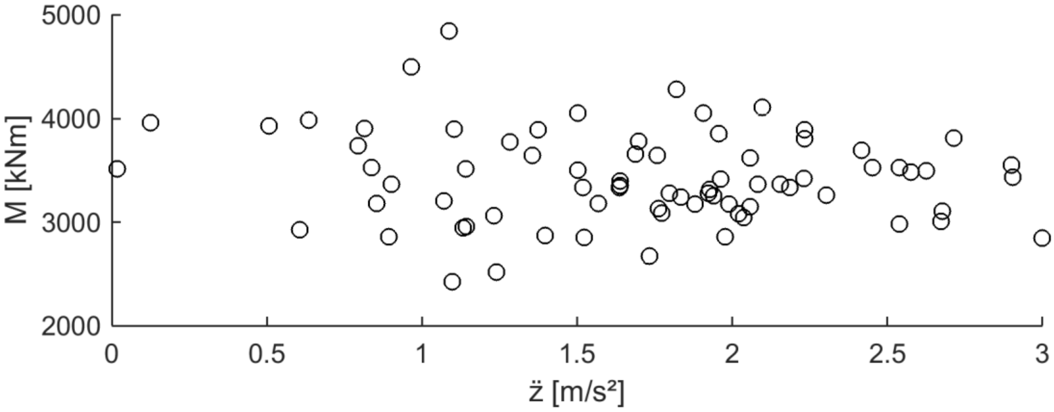

Figure 6-39 Scatterplot of $\ddot{z}(t)$ vs M (BC3), JONSWAP spectrum with $\mathrm{H_S} = 4.0m$, $\mathrm{T_Z} = 9.0s$, $\vartheta = 70°$, $t_{\mathrm{sim}} = 1800s$

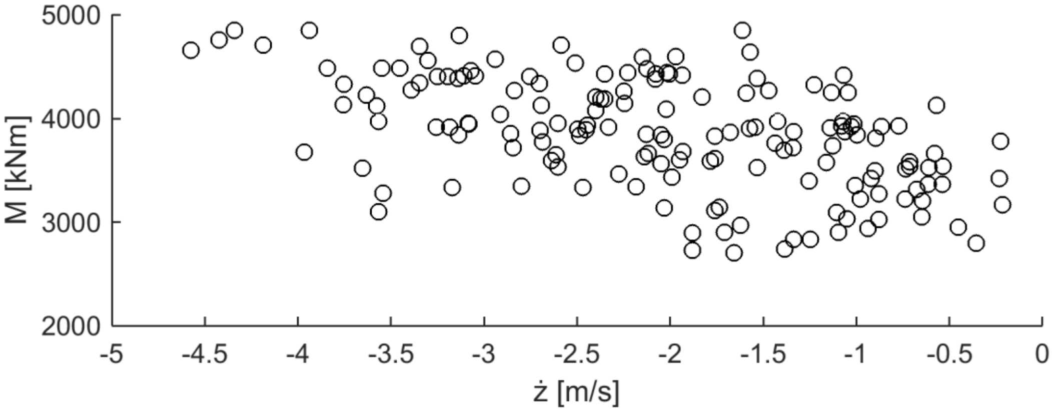

Figure 6-40 Scatterplot of $\dot{z}(t)$ vs M (BC3), JONSWAP spectrum with $\mathrm{H_S} = 4.0m$, $\mathrm{T_Z} = 9.0s$, $\vartheta = 70°$, $t_{\mathrm{sim}} = 1800s$

6.4 Chapter conclusion

For a deep water pipelay operation with a large departure angle (BC1), the vertical stinger tip motions can be related to the axial motions of the pipeline at LOP and the normal motions of the pipeline at TDP. The vertical stinger tip acceleration can be related to the effective top tension and the vertical stinger tip velocity can be related to the effective bottom tension. For installing long slender pipelines in deep water, the maximum bending moments occur in the TDA. Because axial tension and bending moment are related, the maximum bending moment in the pipeline can be related to the vertical stinger tip velocity. The relation is close to quadratic and nonlinear behaviour only occurs for very large excitations of the stinger tip.

For a deep water pipelay operation with a smaller departure angle (BC2), both axial and normal motions of the pipeline are largest in the STA. Therefore the bending moments can be related to the vertical stinger tip accelerations.

Geometric nonlinear behaviour affects the correlation between vertical stinger tip motions and maximum bending moments (or equivalent von Mises strains). It occurs due to the coupling of axial and normal motions along the pipeline. The nonlinear behaviour amplifies for larger amplitudes and larger frequencies. Out-of-plane excitation of the stinger tip can cause additional geometric nonlinearities. This is in particular an issue in shallow water (BC3).

For shallow water pipeline operations the vertical stinger tip motions are not sufficient to predict the axial motions in the pipeline in the STA and the normal motions in the TDA for a shallow water case (BC3). The geometric nonlinear behaviour is significant, because of the horizontal in-plane and out-of-plane motions. Therefore vessel motion based laying criteria in shallow water is dependent on all six DOFs.

7.0 CONCLUSION

The goal of this thesis is to study project specific vessel motion based criteria which can be used to predict the pipeline integrity in the sagbend which is often governing. In this chapter it is indicated to what extent this goal has been achieved and how the results and conclusions can be used for project specific dynamic analyses of pipeline installation models and the development of the on-board SMD software.

7.1 Vessel motion based criteria

For an S-lay vessel laying pipeline in deep water, heave and roll and in particular pitch motions cause the most axial tension and bending moment fluctuations for waves approaching the vessel unidirectional. With the principle of superposition and the assumption that the stinger is rigidly connected to the vessel, these motions result in mainly vertical motions of the stinger tip.

For deep water projects which use a stinger that supports the pipeline until it departures almost perpendicular to the mean sea surface level (BC1), the axial fluctuations of the pipeline at LOP are close to vertical fluctuations of the pipeline. It was seen that for such projects the vertical stinger tip motions can be related to the vertical motions of the pipeline at LOP. Because inertia acts in vertical direction and tension in axial direction, the effective tension at LOP which is equal to the top tension is related to the vertical acceleration of the pipeline at LOP and therefore the vertical acceleration of the stinger tip.

The nonlinear hydrodynamic drag load which is the largest contribution to damping is related to the normal velocities of the pipeline. It was presented that the effective bottom tension is correlated with the axial pipeline velocity at LOP and vertical stinger tip velocity.

For deep water projects with large departure angles (BC1), the maximum bending moment which has the most impact at the pipeline integrity in terms of local buckling occurs in the TDA on a position close to the maximum static bending moment. The effective tension in the TDA is about equal to the effective bottom tension. As a result the vertical stinger tip velocity can also be used to approximate the maximum bending moment in the unsupported part of the pipeline catenary. When pipeline operations use tensioners in deep water lay mode, the relation could be used to define a project specific operational limit based on vessel motions (e.g. maximum vertical stinger tip velocity).

If for deep water projects where the pipeline leaves the stinger under a significant angle relative to the gravitational direction (BC2), there are significant normal motions of the pipeline at LOP. The maximum static bending moment is less explicitly in the TDA. With tensioners compensating dynamic tension, the maximum bending moment occurs in the STA. Therefore vertical stinger tip acceleration can be used to limit the bending moment of the unsupported pipeline.

For the situations of BC1 and BC2, the accuracy and reliability of the relation gets worse for large excitations (large frequencies and/or amplitudes). These excitations result in compressive bottom tension. If the bottom tension of the deep pipeline becomes progressively compressive, geometric nonlinear behaviour will dominate the response behaviour. Therefore the relation between stinger tip motions and pipeline integrity due bending will be affected.

For decreasing water depth and less slender pipelines (BC3), significant resonance occurs. The geometric nonlinearities between tension and bending moment increase and the accuracy of the project specific vessel motion based criteria will be affected negatively. Therefore the method used in this thesis is not yet applicable to limit the pipeline integrity for moderate and shallow water depths.

7.2 Application for Allseas Engineering

The vessel motion based criteria for deep water pipelay projects are derived in two different ways. The first method uses many combinations of regular waves (many simulations) which is the most useful to use for all kinds of sea states. The second method uses sea states in combination with the pairing peak method which is used to test the criteria with a design sea state. For a minimum effective bottom tension, maximum top tension and/or maximum sagbend bending moment, the maximum allowed vertical stinger tip motions can be determined using both methods. Because the effect of approach direction, spreading, variance spectra and significant wave heights / zeros crossing periods have limited influence on the derived vessel motion based criteria, the output can be used to further develop SMD.

8.0 RECOMMENDATIONS

This thesis is a first step into an extensive process to investigate vessel motion based criteria. There are still many steps ahead to use vessel motion based criteria on-board of the pipelay vessels of Allseas. The recommendations for future research are discussed here.

8.1 Recommendations for adding vessel motion based criteria in SMD

The output data of the broad range of short simulations with predefined harmonic vertical stinger tip motions is the most reliable input data for SMD, because this data is purely based on vessel motions. The different combinations between frequency and amplitudes should be interpolated to make the criteria work for all sea states. Besides implementing the vessel motion based criteria, the coding of the SMD software should be adjusted such that the software is able to measure vertical stinger tip motion. Using the principle of superposition and the coordinates of the stinger tip location this can be accomplished. Besides the velocity and acceleration of the stinger tip, also the effective top tension and bottom tension should be monitored. For the tensioners in deep water lay mode (brake between pulls) the monitored data can be compared with the limitations based on vertical stinger tip velocity.

8.2 Recommendations for future research

It was proven that the vessel motion based criteria in deep water showed decent correlation between vertical stinger tip velocities and maximum bending moments for pipeline departure angles close to 90°. If there is a way to measure axial pipeline motions at LOP, one could possibly find better relationship between stinger tip velocities and bending moments. As a result the vessel motion based criteria may also be applicable for smaller departure angles. This should be investigated in further research.

In this thesis the compensating tensioners are modelled without deadband which is a simplification. In the tensioners friction effects are present. Even with advanced tension control, friction and damping contributes to a certain deadband and thus an amount of dynamic tension. The effects of the deadband should be investigated for further research.

In this thesis the pipeline integrity was limited by bending moment. A validation is made with the equivalent von Mises strain. In the classification standard (DNV-OS-F101, 2010), the combined local buckling condition is governing for the pipeline integrity due to local buckling. This condition largely depends on the data of tension, external pressure and bending moment with additional safety factors. In future research, the vessel motion based criteria should implement this local buckling condition.

Parallel to the work of this thesis a funded Joint Industry Project (JIP) on this subject will be performed by Det Norske Veritas. With this thesis, above recommendations and the expected conclusions of this JIP, new targeted goals in finding project specific vessel motion based abandonment criteria could be defined.

LIST OF FIGURES

Figure 1-1 Offshore pipeline installation using the S-lay method. Adapted from (Gong, et al., 2014) 1

Figure 2-1 Vessel motion based criteria vs Sea state based criteria 2

Figure 2-2 Graphical user interface of the SMD application 2

Figure 2-3 Vessel motions in six degrees of freedom at the centre of gravity of the vessel 4

Figure 2-4 local tnb-coordinate system for the pipeline 5

Figure 2-5 2D representation (ZX-plane) of the pipeline catenary in the global XYZ-coordinate system 5

Figure 3-1 1D variance density spectrum of a limiting sea state, JONSWAP, $\mathrm{HS} = 4.0m$, $\mathrm{TZ} = 9.0s$ 7

Figure 3-2 Directional distribution using the cosine-n method 7

Figure 3-3 side view (left) and front view (right) of a modelled support with springs 11

Figure 3-4 Linear elastic foundation 11

Figure 3-5 Internal loads of a small unsupported bend pipeline segment 13

Figure 3-6 moment-curvature relationship 14

Figure 3-7 mass spring dashpot representation of the effective tension at lift-off point 16

Figure 3-8 Euler-Bernoulli beam element with six degrees of freedom 17

Figure 3-9 Rope effect of a 2D simple supported beam with a point load 18

Figure 3-10 Schematic difference between FD and TD 20

Figure 3-11 time integration during one time step (Larsen, 1990) 21

Figure 4-1 Block diagram of the sensitivity study roadmap 23

Figure 4-2 Solitaire pulling a 30" diameter pipeline near the Shetland Islands 24

Figure 4-3 S-Lay catenary shapes of the base cases at different water depths (XZ-plane) 25

Figure 4-4 Tension and bending moment along the unsupported span length (BC1) 26

Figure 4-5 Tension and bending moment along the unsupported span length (BC2) 26

Figure 4-6 Tension and bending moment along the unsupported span length (BC3) 26

Figure 4-7 First 5 mode shapes for the normal motions along the pipeline (up) and in-plane dynamic bending moment along the pipeline in global Y direction (down) (BC1) 28

Figure 4-8 First 5 mode shapes for the normal motions along the pipeline (up) and in-plane dynamic bending moment along the pipeline in global Y direction (down) (BC2) 28

Figure 4-9 First 5 mode shapes for the normal motions along the pipeline (up) and in-plane dynamic bending moment along the pipeline in global Y direction (down) (BC3) 29

Figure 5-1 Translational vessel motions in COG: Surge, Sway and Heave (BC1) 31

Figure 5-2 Rotational vessel motions: Roll, Pitch and Yaw (BC1) 31

Figure 5-3 Translational vessel motions in COG: Surge, Sway and Heave (BC2) 32

Figure 5-4 Rotational vessel motions: Roll, Pitch and Yaw (BC2) 32

Figure 5-5 Translational vessel motions in COG: Surge, Sway and Heave (BC3) 33

Figure 5-6 Rotational vessel motions: Roll, Pitch and Yaw (BC3) 33

Figure 5-7 significant amplitude of surge, sway and heave. JONSWAP spectrum, $\mathrm{HS} = 4.0m$, $\mathrm{TZ} = 9.0s$, $t\mathrm{sim} = 900s$. (BC1/BC2/BC3) 34

Figure 5-8 significant amplitude of roll, pitch and yaw. JONSWAP spectrum, $\mathrm{HS} = 4.0m$, $\mathrm{TZ} = 9.0s$, $t\mathrm{sim} = 900s$. (BC1/BC2/BC3) 34

Figure 5-9 The maximum total bending moment per direction [MN]. JONSWAP spectrum, $\mathrm{HS} = 4.0m$, $\mathrm{TZ} = 9.0s$, $t\mathrm{sim} = 900s$. (BC1) 35

Figure 5-10 The maximum total bending moment per direction [MN]. JONSWAP spectrum, $\mathrm{HS} = 4.0m$, $\mathrm{TZ} = 9.0s$, $t\mathrm{sim} = 900s$. (BC2) 35

Figure 5-11 The maximum total bending moment per direction [MN]. JONSWAP spectrum, $\mathrm{HS} = 4.0m$, $\mathrm{TZ} = 9.0s$, $t\mathrm{sim} = 900s$. (BC3) 35

Figure 5-12 Relation between uncoupled vessel motions and coupled vessel motions at the stinger tip. Influence of pitch (top left), roll (right) and yaw (bottom). 37

Figure 5-13 significant amplitude of the stinger tip motions in the global X, Y and Z direction. JONSWAP spectrum, $\mathrm{Hs} = 4.0m$, $\mathrm{Tz} = 9.0s$, $t\mathrm{sim} = 900s$. (BC1) 38

Figure 5-14 significant amplitude of the stinger tip motions in the global X, Y and Z direction. JONSWAP spectrum, $\mathrm{Hs} = 4.0m$, $\mathrm{Tz} = 9.0s$, $t\mathrm{sim} = 900s$ (BC2/BC3) 38

Figure 5-15 maximum vertical stinger tip and maximum total bending moment. JONSWAP spectrum, $\mathrm{Hs} = 4.0m$, $\mathrm{Tz} = 9.0s$ $t\mathrm{sim} = 900s$ (BC1) 38

Figure 5-16 maximum vertical stinger tip and maximum total bending moment. JONSWAP spectrum, $\mathrm{Hs} = 4.0m$, $\mathrm{Tz} = 9.0s$ $t\mathrm{sim} = 900s$ (BC2) 38

Figure 5-17 maximum vertical stinger tip and maximum total bending moment. JONSWAP spectrum, $\mathrm{Hs} = 4.0m$,$\mathrm{Tz} = 9.0s$, $t\mathrm{sim} = 900$ (BC3) 39

Figure 6-1 spring dashpot representation of dynamic tension at the stinger tip location 40

Figure 6-2 Relation between vertical stinger tip velocity and effective bottom tension using 150 short simulations containing vertical stinger tip excitations with different frequencies and amplitudes (BC1) 41

Figure 6-3 Relation between vertical stinger excitation and the vertical velocity in the pipeline 41

Figure 6-4 Relation between vertical stinger excitation and the effective bottom tension 41

Figure 6-5 Time history of vertical stinger tip velocity (up) and effective bottom tension (down) (BC1) 42

Figure 6-6 Misalignment of a downward peak between different quantities (BC1) 42

Figure 6-7 Scatterplot of $\mathrm{z}(t)$ vs $TTDP$ (BC1), JONSWAP spectra with $\mathrm{HS} = 4.0m$, $\mathrm{TZ} = 9.0s$, $\vartheta = 70°$, $t\mathrm{sim} = 3600s$ 43

Figure 6-8 Scatterplot of $\mathrm{z}(t)$ vs $TTDP$ (BC1), Three simulations with different JONSWAP spectra, $\vartheta = 70°$, $t\mathrm{sim} = 900s$ 43

Figure 6-9 Scatterplot of $\mathrm{z}(t)$ vs $TTDP$ (BC1), Three simulations with different JONSWAP spectra, $\vartheta = 70°$, $t\mathrm{sim} = 900s$ with wave directional spreading (20 components, $n = 8$) 43

Figure 6-10 Scatterplot of $\mathrm{z}(t)$ vs $TTDP$ (BC1), nine simulations with different sea states, JONSWAP spectrum, $\mathrm{HS} = 4.0m$, $\mathrm{TZ} = 9.0s$, $t\mathrm{sim} = 900s$. Beam Quartering waves ($\vartheta = 67.5°$, $\vartheta = 112.5°$), Beam waves ($\vartheta = 90°$), Other waves approach angles ($\vartheta = 0°$, $\vartheta = 22.5°$, $\vartheta = 45°$, $\vartheta = 135°$, $\vartheta = 157.5°$, $\vartheta = 180°$) 44

Figure 6-11 Relation between vertical stinger tip acceleration and effective top tension (BC1) using 150 short simulations containing vertical stinger tip excitations with different frequencies and amplitudes 45

Figure 6-12 Scatterplot of $z(t)$ vs T (BC1), nine simulations with different sea states, JONSWAP spectrum, $\mathrm{HS} = 4.0$, $\mathrm{TZ} = 9.0s$, $t\mathrm{sim} = 900s$. Beam Quartering waves ($\vartheta = 67.5°$, $\vartheta = 112.5°$), Beam waves ($\vartheta = 90°$), All other waves approach angles ($\vartheta = 0°$, $\vartheta = 22.5°$, $\vartheta = 45°$, $\vartheta = 135°$, $\vartheta = 157.5°$, $\vartheta = 180°$) 45

Figure 6-13 Static comparison of effective tension and bending moment in the sagbend (BC1) 46

Figure 6-14 Dynamic effective tension due to a harmonic wave (BC1) with $H = 1$, $\omega = \pi 4\ \mathrm{rad}/s$, $\vartheta = 70°$ 46

Figure 6-15 Dynamic effective tension due to a harmonic wave (BC1) with $H = 4$, $\omega = \pi 4\ \mathrm{rad}/s$, $\vartheta = 70°$ 46

Figure 6-16 Effective tension at TDP (downward peaks) and bending moment a the mid-point of the element containing the maximum bending moment (upward peaks) (BC1) 47

Figure 6-17 Scatterplot $TTDP$ vs M (BC1), JONSWAP spectra with $\mathrm{HS} = 4.0m$, $\mathrm{TZ} = 9.0s$, $\vartheta = 70°$, $t\mathrm{sim} = 3600s$ 48

Figure 6-18 Scatterplot $TTDP$ vs $M\mathrm{dyn}$ (BC1), JONSWAP spectra with $\mathrm{HS} = 4.0m$, $\mathrm{TZ} = 9.0s$, $\vartheta = 70°$, $t\mathrm{sim} = 3600s$ 48

Figure 6-19 Relation between effective bottom tension and bending moment using 150 short simulations containing vertical stinger tip excitations with different frequencies and amplitudes (BC1) 48

Figure 6-20 axial velocity and effective tension along the pipeline (BC1) by horizontal excitation of the stinger tip ω=0.6 [rad/s] and amplitude=2.0 [m] 49

Figure 6-21 axial velocity and effective tension along the pipeline (BC1) by vertical excitation of the stinger tip ω=0.6 [rad/s] and amplitude=2.0 [m] 49

Figure 6-22 axial velocity and effective tension along the pipeline (BC1) by horizontal excitation of the stinger tip ω=1.2 [rad/s] and amplitude=2.0 [m] 50

Figure 6-23 axial velocity and effective tension along the pipeline (BC1) by vertical excitation of the stinger tip ω=1.2 [rad/s] and amplitude=2.0 [m] 50

Figure 6-24 normal velocity and total bending moment along the pipeline (BC1) by horizontal excitation of the stinger tip ω=0.6 [rad/s] and amplitude=2.0 [m] 51

Figure 6-25 normal velocity and total bending moment along the pipeline (BC1) by vertical excitation of the stinger tip ω=0.6 [rad/s] and amplitude=2.0 [m] 51

Figure 6-26 normal velocity and total bending moment along the pipeline (BC1) by horizontal excitation of the stinger tip ω=1.2 [rad/s] and amplitude=2.0 [m] 52

Figure 6-27 normal velocity and total bending moment along the pipeline (BC1) by vertical excitation of the stinger tip ω=1.2 [rad/s] and amplitude=2.0 [m] 52

Figure 6-28 axial velocity, normal velocity, effective tension and total bending moment along the pipeline (BC3) by horizontal excitation of the stinger tip ω=0.9 [rad/s] and amplitude=2.0 [m] 53

Figure 6-29 axial velocity, normal velocity, effective tension and total bending moment along the pipeline (BC3) by vertical excitation of the stinger tip ω=0.9 [rad/s] and amplitude=2.0 [m] 53

Figure 6-30 Out-of-plane bending moment, In-plane bending moment and total bending moment along the pipeline (BC3) by out-of-plane horizontal excitation of the stinger tip ω=0.9 [rad/s] and amplitude=2.0 [m] 54

Figure 6-31 binormal velocity, normal velocity and axial velocity along the pipeline (BC3) by out-of-plane horizontal excitation of the stinger tip ω=0.9 [rad/s] and amplitude=2.0 [m] 54

Figure 6-32 First 5 mode shapes for the binormal motions along the pipeline (up) and out-of-plane dynamic bending moment along the pipeline (down) (BC3) 55

Figure 6-33 Relation between vertical stinger tip velocity and bending moment using 150 short simulations containing vertical stinger tip excitations with different frequencies and amplitudes (BC1) 56

Figure 6-34 Scatterplot of $\mathrm{z}(t)$ vs M (BC1), nine simulations with different sea states, JONSWAP spectrum, $\mathrm{HS} = 4.0m$, $\mathrm{TZ} = 9.0s$, $t\mathrm{sim} = 900s$. Beam Quartering waves ($\vartheta = 67.5°$, $\vartheta = 112.5°$), Beam waves ($\vartheta = 90°$), All other waves approach angles ($\vartheta = 0°$, $\vartheta = 22.5°$, $\vartheta = 45°$, $\vartheta = 135°$, $\vartheta = 157.5°$, $\vartheta = 180°$) 56

Figure 6-35 Relation between vertical stinger tip velocity and maximum equivalent von Mises strain using 150 short simulations containing vertical stinger tip excitations with different frequencies and amplitudes (BC1) 57

Figure 6-36 Scatterplot of $\mathrm{z}(t)$ vs $\varepsilon\mathrm{vm}$ (BC1), JONSWAP spectrum with $\mathrm{HS} = 4.0m$, $\mathrm{TZ} = 9.0s$, $\vartheta = 70°$, $t\mathrm{sim} = 3600s$ 57

Figure 6-37 Scatterplot of $z(t)$ vs M (BC2), JONSWAP spectrum with $\mathrm{HS} = 4.0m$, $\mathrm{TZ} = 9.0s$, $\vartheta = 70°$, $t\mathrm{sim} = 1800s$ 58

Figure 6-38 Scatterplot of $z(t)$ vs M (BC2), nine simulations with different sea states, JONSWAP spectrum, $\mathrm{HS} = 4.0m$, $\mathrm{TZ} = 9.0s$, $t\mathrm{sim} = 900s$. Beam Quartering waves ($\vartheta = 67.5°$, $\vartheta = 112.5°$), Beam waves ($\vartheta = 90°$), All other waves approach angles ($\vartheta = 0°$, $\vartheta = 22.5°$, $\vartheta = 45°$, $\vartheta = 135°$, $\vartheta = 157.5°$, $\vartheta = 180°$) 58

Figure 6-39 Scatterplot of $z(t)$ vs M (BC3), JONSWAP spectrum with $\mathrm{HS} = 4.0m$, $\mathrm{TZ} = 9.0s$, $\vartheta = 70°$, $t\mathrm{sim} = 1800s$ 59

Figure 6-40 Scatterplot of $\mathrm{z}(t)$ vs M (BC3), JONSWAP spectrum with $\mathrm{HS} = 4.0m$, $\mathrm{TZ} = 9.0s$, $\vartheta = 70°$, $t\mathrm{sim} = 1800s$ 59

Figure B-1 von Karman vortex street 71

Figure B-2 Regimes of fluid flow across a smooth pipeline (Blevins, 2001) 71

Figure C-1 significant amplitude of surge, sway and heave. JONSWAP spectrum, $\mathrm{HS} = 4.0m$, $\mathrm{TZ} = 9.0s$, $t\mathrm{sim} = 900s$. Wave spreading, $n = 8$ (BC1/BC2/BC3) 72

Figure C-2 significant amplitude of roll, pitch and yaw. JONSWAP spectrum, $\mathrm{HS} = 4.0m$, $\mathrm{TZ} = 9.0s$, $t\mathrm{sim} = 900s$. Wave spreading, $n = 8$ (BC1/BC2/BC3) 72

Figure C-3 The maximum total bending moment per direction $[\mathrm{MN}]$. JONSWAP spectrum, $\mathrm{HS} = 4.0m$, $\mathrm{TZ} = 9.0s$, $t\mathrm{sim} = 900s$. Wave spreading, $n = 8$ (BC1) 72

Figure C-4 The maximum total bending moment per direction $[\mathrm{MN}]$. JONSWAP spectrum, $\mathrm{HS} = 4.0m$, $\mathrm{TZ} = 9.0s$, $t\mathrm{sim} = 900s$. Wave spreading, $n = 8$ (BC2) 72

LIST OF TABLES

Table 4-1 General model properties used in OrcaFlex 23

Table 4-2 FEM properties used in OrcaFlex 23

Table 4-3 Pipeline properties of the three base cases 24

Table 4-4 Properties of pipelay model and the associated static approximation for all three base cases 25

Table 4-5 Natural frequencies of the in-plane mode shapes for each base case 27

Table 6-1 Eigenfrequencies of the out-of-plane mode shapes (BC3) 55

REFERENCES

Allseas. (2015). Pipeline Engineering Help File.

Bai, Y., & Bai, Q. (2005). *Subsea Pipelines and Risers.* Elsevier Science.

Blevins, R. (2001). *Flow Induced Vibration (2nd edition).* Malabar, USA: Krieger Publishing Company.

Brewer, W., & Dixon, D. (1970). Influence of Lay Barge Motions on a Deepwater Pipeline Laid Under Tension. *Journal of Engineering for Industry*.

Callegari, M., Carini, C., Lenci, S., Torselletti, E., & L., V. (2003). Dynamics models of marine pipelines for installation in deep and ultra-deep waters: Analytical and numerical approaches. *16th AIMETA Congress of Theoretical and Applied Mechanics* (pp. 1-12). Ferrara, Italy: AIMETA.

Chatjigeorgiou, I. (2008). A finite differences formulation for the linear and nonlinear dynamics of 2D catenary risers. *Ocean Engineering 35*, 616-636.

Chatjigeorgiou, I. (2013). Second-order nonlinear dynamics of catenary pipelines: A frequency domain approach. *Computers and Structures 123*, 1-14.

Chatjigeorgiou, I., & Mavrakos, S. (2009). Heave induced out-of-plane motions on catenary risers. *13th Congress of Intl. Maritime Assoc. of Mediterranean (IMAM 2009).* Istanbul: Turkey.

Chatjigeorgiou, I., & Mavrakos, S. (2010). The 3D Nonlinear Dynamics of Catenary Slender Structures for Marine Applications. In E. Evans, *Nonlinear Dynamics* (pp. 173-198). Rijeka, Croatia: InTech.

Chatjigeorgiou, I., Passano, E., & Larsen, C. (2007). Extreme Bending Moments on Long Catenary Risers due to Heave Excitation. *26th International Conference on Offshore Mechanics and Arctic Engineering.* San Diego, USA: ASME.

Chung, J., & Hulbert, G. (1993). A Time Integration Algorithm for Structural Dynamics With Improved Numerical Dissipation: The Generalized-α Method. *Journal of Applied Mathematics 60*, ASME.

Clauss, G., Weede, H., & Riekert, T. (1992). Offshore pipe laying operations - Interaction of vessel motions and pipeline dynamic stresses. *Applied Ocean Research 14*, 175-190.

Cook, R., Malkus, D., & Plesha, M. (1989). *Concepts and Applications of Finite Element Analysis (3rd edition).* John Wiley & Sons.

Dixon, D., & Rutledge, D. (1968). Stiffened Catenary Calculations in Pipeline Laying Problem. *Journal of Engineering for Industry*, 153-160.

DNV. (2010). DNV-OS-F101 Submarine Pipeline Systems. Det Norske Veritas.

DNV. (2010). DNV-RP-C205. *Submarine Pipeline Systems*. Det Norske Veritas.

Gong, S., Xu, P., Bao, S., Zhong, S., He, N., & Yan, H. (2014). Numerical modelling on dynamic behaviour of deepwater S-lay pipeline. *Ocean Engineering 88*, 393-408.

Holthuijsen, L. (2007). *Waves in Oceanic and Coastal Waters.* Delft, Netherlands: Cambridge University Press.

Jensen, G. (2010). *Offshore Pipelaying Dynamics.* Trondheim, Norway: Norwegian University of Science and Technology.

Journée, J., & Massie, W. (2000). *Offshore Hydromechanics.* Delft, Netherlands: Delft University of Technology.

Larsen, C. (1990). *Response Modelling of Marine Risers and Pipelines.* Trondheim, Norway: The Norwegion Institute of Technology.

Legras, J. (2008). Vessel Motions Based Laying Criteria for Rigid and Flexible Pipes in Deepwater. *18th International Offshore and Polar Engineering Conference* (pp. 48-52). Vancouver, Canada: ISOPE.

Li, J., Chen, Y., Gong, S., & Jin, W. (2010). Configuration of Submarine Pipeline for Deepwater S-lay Technique. *20th International Offshore and Polar Engineering Conference* (pp. 188-193). Beijing, China: ISOPE.

Marbus, G. (2007). *Verification of the water forces on stinger of Allseas' Solitaire.* Delft, Netherlands: Delft University of Technology.

McGraw-Hill. (2002). *McGraw-Hill Dictionary of Scientific and Technical Terms (6th edition).* McGraw-Hill Education.

Metrikine, A. (2009). *Dynamics, Slender Structures and an Introduction to Continuum Mechanics.* Delft, Netherlands: Delft University of Technology.

Nonemaker, J. (2012). *An investigation into the modelling and control of pipeline tension.* Delft, Netherlands: Delft University of Technology.

Ogink, R. (2001). *Dynamics Of A Deepwater Suspended Pipeline During J-Lay.* Delft, Netherlands: Delft University of Technology.

Orcina. (2014). OrcaFlex 9.8 manual.

Passano, E., & Larsen, C. (2006). Efficient Analysis of a Catenary Riser. *25th International Conference on Offshore Mechanics and Arctic Engineering.* Hamburg, Germany: ASME.

Randolph, M., & Quiggin, P. (2009). Non-linear hysteretic seabed model for catenary pipeline contact. *28th International Conference on Offshore and Arctic Engineering.* Honolulu, Hawaii, USA: ASME.

Rienstra, S. (1987). Analytical Approximations For Offshore Pipelaying Problems. *1st International Conference on Industrial and Applied Mathematics* (pp. 99-108). Paris-La Villette, France: Society for Industrial & Applied Mathematics.

Schmidt, W. (1977). Submarine Pipeline Analysis With an Elastic Foundation by the Finite Element Method. *Journal of Engineering for Industry*, 480-484.

Shekker, V., Healey, A., & Sezer, F. (1984). A Linearized Approach for the Evaluation of Dynamic Stresses in Offshore Pipelines During Installation. *3rd International Offshore Mechanics and Arctic Engineering Symposium.* New Orleans, USA.

Sparks, C. P. (2007). *Fundamentals of Marine Riser Mechanics: Basic Prinsiples and Simplified Analyses.* PennWell Corp.

Standing, R. (2005). *Review of the role of response forecasting in decision-making for weather-sensitive offshore operations.* Teddington, UK: HSE books.

Sumer, B., & Fredsøe, J. (1997). *Hydrodynamics Around Cylindrical Structures.* World Scientific.

Suzuki, N., & Jingu, N. (1982). Dynamic Behavior of Submarine Pipelines Under Laying Operation. *Journal of Energy Resources Technology 104*, 313-318.

Verwoert, R. (2012). *Rollerbox Modelling.* Delft, Netherlands: Saxion Enschede.

Williams, R., Williams, K., & Walker, A. (2002). Load controlled or displacement controlled? *25th Offshore Pipeline Technology Conference.* Amsterdam, The Netherlands.

APPENDIX A: FREE VIBRATIONS FOR THE BENDING OF A SIMPLY SUPPORTED BEAM

In this section the natural frequencies and mode shapes are derived for the pipeline modelled as a simply supported beam. It is mainly based on (Metrikine, 2009). For the undamped bending motion of a homogenous cylindrical beam with length L and without external load (free vibration), the equation of motion is:

$$\rho_s A \ddot{\mathrm{r}}_{\mathrm{n}}(s,t) + EI\mathrm{r}_{\mathrm{n}}{}^{\mathrm{IV}}(s,t) = 0 \tag{A.1}$$

The initial conditions are:

$$\begin{gathered}\mathrm{r}_{\mathrm{t}}(s,0) = \mathrm{r}_{\mathrm{t_{sta}}}(s) \\ \dot{\mathrm{r}}_{\mathrm{t}}(s,0) = \mathrm{v}_{\mathrm{t_{sta}}}(s)\end{gathered} \tag{A.2}$$

And the boundary conditions:

$$\begin{gathered}\mathrm{r}_{\mathrm{n}}(0,t) = \mathrm{r}_{\mathrm{n}}''(0,t) = 0 \\ \mathrm{r}_{\mathrm{n}}(L,t) = \mathrm{r}_{\mathrm{n}}''(L,t) = 0\end{gathered} \tag{A.3}$$

Using the method of separation of variables, the solution of $\mathrm{r}_{\mathrm{n}}(s,t)$ can be determined into the form of equation (A.4) with unknown functions $\Upsilon(s)$ and $\Psi(t)$.

$$\mathrm{r}_{\mathrm{n}}(s,t) = \Upsilon(s)\Psi(t) \tag{A.4}$$

Substituting (A.4) in equation (A.1) and dividing the result by $\rho_s A$ and $\Upsilon(s)\Psi(t)$ gives equation (A.5).

$$\frac{1}{\Psi(\mathrm{t})}\ddot{\Psi}(t) + \frac{\rho_s A}{EI}\frac{1}{\Upsilon(s)}\Upsilon^{\mathrm{IV}}(s) = 0 \tag{A.5}$$

The first term in equation (A.5) depends on time, while the second term depends on the natural coordinate. To make the equation valid, these terms must be equal to a separation constant. To ensure that the beam is capable of performing harmonic vibrations this separation constant is equal to ω^2.

$$\begin{gathered}\frac{1}{\Psi(\mathrm{t})}\ddot{\Psi}(t) = -\omega^2 \\ \frac{\rho A}{EI}\frac{1}{\Upsilon(s)}\Upsilon^{\mathrm{IV}}(s) = \omega^2\end{gathered} \tag{A.6}$$

For the time dependent part of (A.6) the general solution is a simple harmonic motion with two unknown constants (A and B) and yields:

$$\Psi(t) = \mathrm{A}\sin(\omega t) + \mathrm{B}\cos(\omega t) \tag{A.7}$$

For the spatial dependent part of (A.6) the general solution is equal to equation (A.8) where C_1, C_2, C_3, C_4 are constants and β is equal to equation (A.9)

$$\Upsilon(s) = C_1 \sin\beta s + C_2 \cos\beta s + C_3 \sinh\beta s + C_4 \cosh\beta s \tag{A.8}$$

$$\beta^4 = \frac{\rho_s A}{EI}\omega^2 \tag{A.9}$$

The boundary conditions of (A.3) can be rewritten in terms of $\Upsilon(s)$, because this should be correct at any time interval.

$$\begin{gathered}\Upsilon(0,t) = \Upsilon''(0,t) = 0 \\ \Upsilon(L,t) = \Upsilon''(L,t) = 0\end{gathered} \tag{A.10}$$

By substituting the general solution of equation (A.8) in the boundary conditions of (A.10), equation (A.11) and (A.12) are found. Note that the constants C_1, C_2, C_3, C_4 cannot vanish at the same time.

$$C_2 = C_3 = C_4 = 0 \tag{A.11}$$

$$\sin(\beta L) = 0 \rightarrow \beta_n L = n\pi \quad \text{for} \quad n = 1,2,3,\dots \tag{A.12}$$

Equation (A.12) defines the natural frequencies of the undamped system which can be rewritten to equation (A.13).

$$\omega_n = \sqrt{\frac{EI}{\rho_s A}}\left(\frac{n\pi}{L}\right)^2 \tag{A.13}$$

Consequently, the normal modes $\Upsilon_n(s)$ for $n = 1,2,3,\ldots$ for the vibration of the beam can be found with equation (A.14).

$$\Upsilon_n(s) = C_n \sin(\beta_n s) \tag{A.14}$$

The general vibrations of $\mathrm{r_n}(s,t)$ in the beam is a combination between the time dependent part of equation (A.7) and the spatial dependent part of equation (A.14) which gives equation (A.15).

$$\mathrm{r_n}(s,t) = \sum_{n=1}^{\infty} [\mathrm{A}_n \sin(\omega_n t) + \mathrm{B}_n \cos(\omega_n t)] \sin(\beta_n s) \tag{A.15}$$

The constants A_n and B_n are still unknown and can be determined from the initial conditions of (A.2). Equation (A.15) will be completely different if other boundary conditions are chosen. For the nonlinear bend pipeline the natural frequencies, normal modes and general vibrations of the beam should be determined numerically (e.g. OrcaFlex)

APPENDIX B: HYDRODYNAMIC FLUID FLOW REGIMES

The flow of a fluid around a cylinder circumference is very depending on the Reynolds number. For very low Reynolds numbers ($\mathrm{Re} < 5$) there is no flow separation in the wake behind the cylinder and inertia forces will dominate the pressure. For $5 < \mathrm{Re} < 40$, flow separation starts and increase. In the wake symmetric vortices occur in pairs. For higher Reynolds numbers ($40 < \mathrm{Re} < 150$), the vortices become unstable and alternate shedding in the wake occurs following a Von Karman vortex street (Figure B-1). For higher Reynolds numbers ($150 < \mathrm{Re} < 300$), there is a transition of laminar flow to turbulent flow.

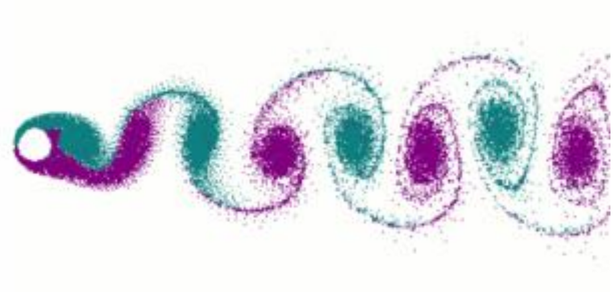

Figure B-1 von Karman vortex street

For subcritical flow ($300 < \mathrm{Re} < 3 \cdot 10^5$), the wake is fully turbulent and reaches the laminar boundary layer on one side of the wake. In the critical flow regime ($3 \cdot 10^5 < \mathrm{Re} < 3.5 \cdot 10^5$), the laminar boundary layer separates on the front side of the cylinder and later reattaches on the cylinders surface. The wake behind the cylinder is still turbulent. For higher Reynolds numbers ($3.5 \cdot 10^5 < \mathrm{Re} < 3.5 \cdot 10^6$) a laminar to turbulent transition occurs on the other side of the cylinder. The wave will be narrower and disorganized. This regime is called the supercritical flow regime. In the post critical flow regime ($\mathrm{Re} > 3.5 \cdot 10^6$), the boundary layer becomes entirely turbulent and regular vortex shedding is re-established (Blevins, 2001), (Sumer & Fredsøe, 1997), (Journée & Massie, 2000).

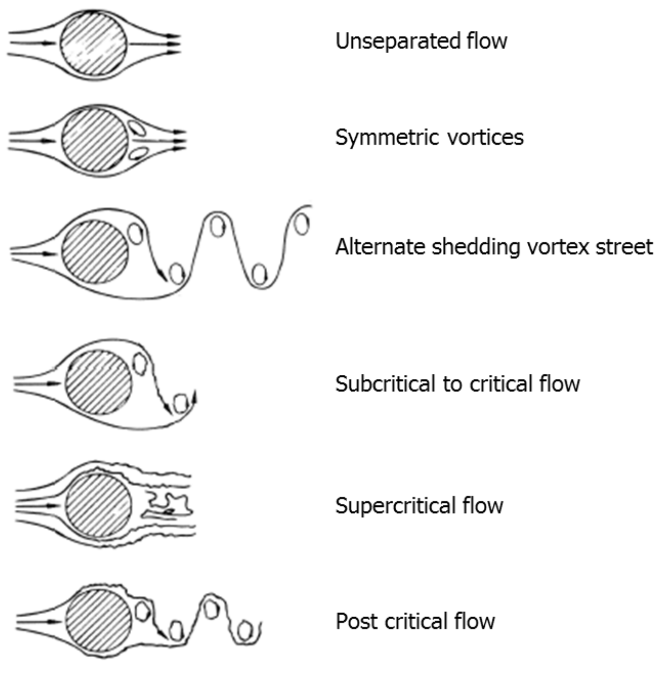

Figure B-2 Regimes of fluid flow across a smooth pipeline (Blevins, 2001)

Reynolds numbers for pipelines at sea will range from 10^4 to 10^6 which are in the subcritical, critical and supercritical regions (Ogink, 2001).

APPENDIX C: INFLUENCE OF DIRECTIONAL WAVE SPREADING

In section 5.1.2, each simulation uses a sea state with the waves propagating into one direction. In reality, waves in a short crested irregular sea state are propagating into multiple directions. To find the directional dependency of the vessel motions with regards to the sagbend bending moment using moderate wave directional spreading, the simulations of section 5.1.2 are performed again by using an extended two-dimensional JONSWAP spectrum with 20 directional components and the power $n = 8$ (section 1.2). The significant amplitudes of the vessel motions are shown in Figure C-1 and Figure C-2.

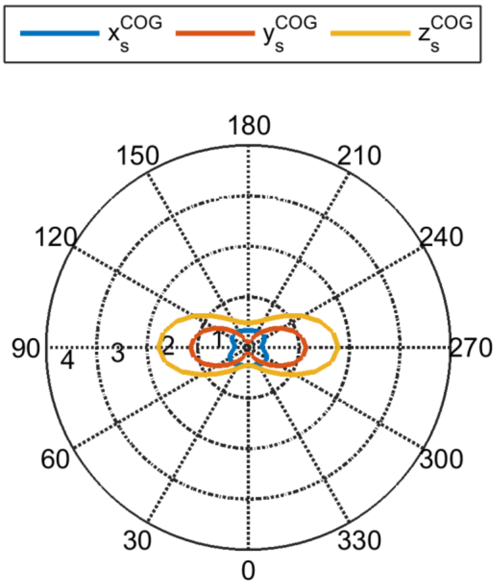

Figure C-1 significant amplitude of surge, sway and heave. JONSWAP spectrum, $\mathrm{H_S} = 4.0m$, $\mathrm{T_Z} = 9.0s$, $t_{\mathrm{sim}} = 900s$. Wave spreading, $n = 8$ (BC1/BC2/BC3)

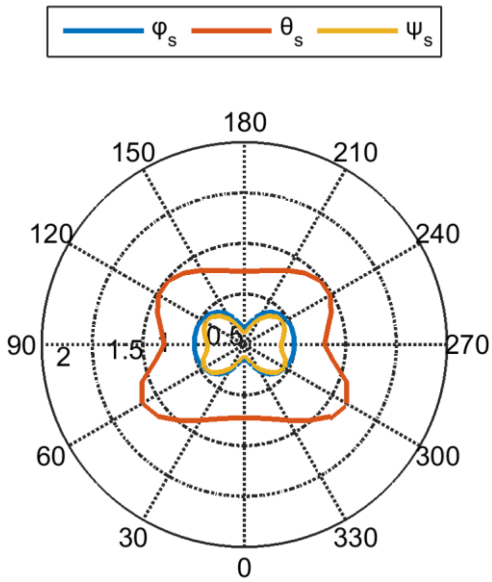

Figure C-2 significant amplitude of roll, pitch and yaw. JONSWAP spectrum, $\mathrm{H_S} = 4.0m$, $\mathrm{T_Z} = 9.0s$, $t_{\mathrm{sim}} = 900s$. Wave spreading, $n = 8$ (BC1/BC2/BC3)

Wave directional spreading results into a more even distribution of vessel motions. The most noticeable effect is for beam waves (90°), where pitch and yaw motions are present. Therefore beam with wave directional spreading will also amplify the bending moments of the unsupported pipeline in the sagbend (Figure C-3 and Figure C-4). Beam quartering waves cause the highest bending moments, although they are less compared to no wave spreading. The shape of the bending moment polar plots still looks similar to the shape of the significant pitch motions. The bending moment in the pipeline due to beam waves is in addition to heave motions now also depending on pitch motions.

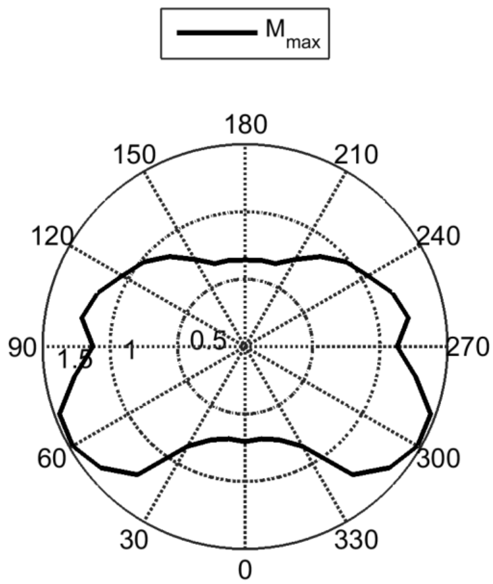

Figure C-3 The maximum total bending moment per direction $[\mathrm{MN}]$. JONSWAP spectrum, $\mathrm{H_S} = 4.0m$, $\mathrm{T_Z} = 9.0s$, $t_{\mathrm{sim}} = 900s$. Wave spreading, $n = 8$ (BC1)

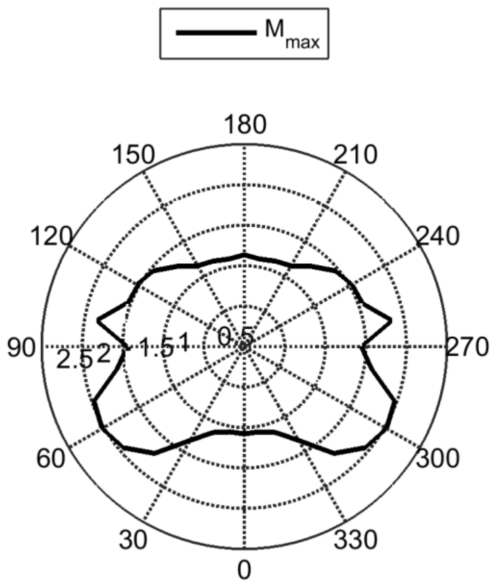

Figure C-4 The maximum total bending moment per direction $[\mathrm{MN}]$. JONSWAP spectrum, $\mathrm{H_S} = 4.0m$, $\mathrm{T_Z} = 9.0s$, $t_{\mathrm{sim}} = 900s$. Wave spreading, $n = 8$ (BC2)